MODELING AND DETECTING ORBIT OBSERVATION ERRORS USING STATISTICAL METHODS

A Thesis

Submitted to the Faculty

of

Purdue University

by

Christopher Y. Jang

In Partial Fulfillment of the

Requirements for the Degree

of

Master of Science

August 2020

Purdue University

West Lafayette, Indiana

THE PURDUE UNIVERSITY GRADUATE SCHOOL
STATEMENT OF THESIS APPROVAL

Dr. Carolin Frueh, Chair

School of Aeronautics and Astronautics

Dr. Kathleen Howell

School of Aeronautics and Astronautics

Dr. David Spencer

School of Aeronautics and Astronautics

Approved by:

Dr. Gregory Blaisdell

Associate Head of Graduate Program of Aeronautics and Astronautics

dedicated to a lifetime of learning

ACKNOWLEDGMENTS

I must first thank my advisor, Dr. Carolin Frueh, for her neverending support as I completed my research. Without her guidance, none of this would be possible. I'd also like to thank committee members, Dr. Kathleen Howell and Dr. David Spencer, for their time and support. I am honored to have learned from them.

I am grateful to the United States Air Force and the Air Force Space Command Scholars Program for providing me the opportunity to pursue my advanced academic degree at Purdue University. I will forever remember my time at Purdue fondly.

Thank you to my colleagues, fellow graduate students, and friends I've made while at Purdue. Special thanks go out to my mother and father for nurturing my curiosity for learning. Thank you to my brother and sister for supporting me unconditionally. To Nicole, my biggest fan and biggest supporter, thank you for all your encouragement.

TABLE OF CONTENTS

Page

Page

LIST OF TABLES

Table Page

LIST OF FIGURES

Figure Page

Figure Page

Figure Page

Figure Page

ABSTRACT

Jang, Christopher Y. M.S., Purdue University, August 2020. Modeling and Detecting Orbit Observation Errors Using Statistical Methods. Major Professor: Dr. Carolin Frueh.

In the globally collaborative effort of maintaining an accurate space catalog, it is of utmost importance for ground tracking stations to provide observations which can be used to update and improve the catalog. However, each tracking station is responsible for viewing thousands of objects in a limited window of time. Limitations in sensor capabilities, human error, and other circumstances inevitably result in erroneous, or unusable, data, but when receiving information from a tracking station, it may be difficult for the end-user to determine a data set's usability. Variables in equipment, environment, and processing create uncertainties when computing the positions and orbits of the satellites. Firstly, this research provides a reference frame for what degrees of errors or biases in equipment translate to different levels of orbital errors after a least squares orbit determination. Secondly, using just an incoming data set's angle error distribution compared to the newly determined orbit, statistical distribution testing is used to determine the validity and usability of the newly received data set. In the context of orbit position uncertainty, users are then able to communicate and relay the uncertainties in the data they share while assessing incoming data for potential sources of error.

1. INTRODUCTION

The first human-made satellite was launched into orbit in October of 1957, and since, society has relied on satellites in Near-Earth space for various tasks, including weather observations, telecommunications, global positioning and navigation, space-to-ground observations, as well as space-based space observations. Near-Earth space, in general, is divided into three major regions: Low-Earth Orbit (LEO) includes the space under 2,000 km altitude above the Earth's surface; Medium-Earth Orbit (MEO) includes the space between 2,000 and 35,586 km altitude; Geosynchronous Earth Orbit (GEO) includes the space between 35,586 and 35,986 km altitude.

There are also various specialty orbits, such as the Highly Elliptical Orbit (HEO), which takes advantage of the long dwell times satellites experience when they reach their highest altitudes. An example of this include the Molniya Orbit, named after early Russian communications satellites. The GEO Transfer Orbit (GTO), is a subclass of HEO used to transport vehicles or payloads from LEO to GEO. In GEO, a circular orbit with zero inclination relative to the Earth's equator is called Geostationary. Its orbital period matches the rotation of the Earth, which causes satellites to appear fixed in the sky. It is one of the most desirable orbits for communication satellites. The Sun-Synchronous Orbit (SSO) is a subclass of LEO and uses a high inclination (nearly polar) so that a satellite and its solar panels can remain in constant sunlight, which is good for weather and imaging satellites [1].

The advantages for a government or private organization to have satellites in Near-Earth Space are clear. As a result, the space environment has become increasingly congested in recent years. There is ongoing research by organizations researching the validity and application of space-based space situational awareness (SSA) via cubesat constellations [2], which presents a new platform for detecting and tracking objects in Near-Earth space. This promises improvements in coverage of objects

otherwise undetectable from the surface of the Earth, and removes sources of error from atmosphere and weather.

In addition to more human-made objects being launched into orbit, major satellite collisions, break-ups, and explosions in the last two decades have contributed greatly to the increase in number of near-Earth space objects. China's anti-satellite (ASAT) missile demonstration in 2007 destroyed Chinese weather satellite, Fengyun 1C, which created an estimated 150,000 pieces of debris, of which approximately 3,000 were large enough to track [3]. In 2009, American satellite Iridium 33 and Russian satellite Cosmos 2251 collided, and approximately 2,000 pieces of debris have been tracked since [4]. These pieces of debris pose serious threats to the usability of the Near-Earth Space environment, and proper tracking can help prevent future collisions, whether it is satellite to satellite or satellite with debris.

United States Strategic Command (USSTRATCOM) maintains a publicly available catalog of satellites in orbit larger than 10 cm and larger than 1 m in GEO. Even within these criteria, not all objects are well tracked due to various uncertainties such as attitude, reflective properties, area-to-mass ratios, etc. Currently, USSTRATCOM tracks nearly 20,000 objects, and approximately 80% of these objects are contained in just the LEO region. There is a collaborative effort across many organizations to maintain an accurate catalog, but this is often difficult because of limited resources and equipment [5]. Most notably, the largest obstacle for SSA collaboration is political: political motives outweigh and limit organizations' willingness to share information. In the early stages of space operations, government organizations tracked objects and kept that information to themselves in the interest of national security.

In aerospace industry operations (private and government), the most common methods for dealing with recreating error or sources of error involve using large arrays of tabulated information, which are comprised of historical, empirical data, or using computationally expensive or labor intensive error models. Tabulated data relies on historical information and requires potentially large amounts of on-board storage. On the other hand, complex error models must be updated frequently to match the

constantly changing Earth environment, which can lead to inefficiencies especially when urgent orbit updates are needed [6]. Because orbits must be updated in a timely fashion, only 1.5% of observational measurement data get the approval from Air Force Space Command (AFSPC) to use higher order models. These cases often require the use of human orbital analysts, who check observational data for timing errors, uncoordinated maneuvers, or other sources of error [7].

Because of the high volume of information related to tracked objects in Near-Earth space, many error models and propagation models use simplified designs for the sake of computational efficiency. This provides an interesting challenge when computing precise orbits [8]: highly precise and accurate tracking of objects comes at the price of computational efficiency. Instead of using complex propagators, simple models are used with updated observations to provide improvements to orbits. The updates to the orbits can compensate for the models' simplicities; however, this places a great importance on a tracking station's ability to take and record usable observations [9].

In addition to the AFSPC catalog, there are other operational agencies across the world, private and government, dedicated to tracking and reporting space objects and debris. Analytic Graphics, Inc. (AGI) is using its expertise in orbit modeling and debris tracking software in Commercial Space Operations Center. AGI works very closely with AFSPC and provides software support for its space operations [10]. There exists a Russian space catalog as well, the Vimpel Catalogue, and likewise, ESA, NASA, and other government-affiliated agencies have taken measures to improve SSA [11]. Commercial companies with assets in space each have their motives for maintaining or providing SSA, and now, a number of companies are interested in the removal of space debris. For example, Astroscale, a Japanese company, is planning a debris removal demonstration within the next 12 months [12]. However, organizations have their own methods and procedure for recording observations, and although they may share information, they do not specifically share what assumptions are made in the process or how computations were made. This creates the need to investigate

and research the different error sources and how to detect them in a data stream of known objects by observing patterns and trends.

It is clear that there are many stakeholders in the space domain, each with their different methods of observing and tracking space objects. This information is not often shared on a public domains, and when data is shared, only fully computed orbits are provided, as orbital elements or the position and velocity state. The technical methods used to compute these values are left unstated. In these cases, raw data is rarely shared if ever, and the end-user, with very little information, needs to decide if a calculated orbit is accurate and to what level of confidence. To complicate matters further, observation stations use different methods and equipment for making satellite observations, each of which have their strengths and weaknesses and various levels of precision and sources of error. The most common satellite observation equipment is the optical telescope. Other common methods include radar and laser ranging; however, optical sensor types will be the focus of this thesis.

An optical telescope observes the reflection of a light source (the sun) off the surface of a tracked object. The light travels from the satellite to the ground station and loses energy at each stage, and thus, optical equipment ideally must be able to detect very faint signals of light as well as very bright signals in order detect a wide range of objects. The light received by the optics excites the elements in a charge coupled device (CCD), which in essence converts and records the light as a digital signal on a computer. The quality of the extracted pixel position depends on the tracking ability of the station, the optics of the telescope, and the processing ability of the computer [13]. The object's location in space is determined using star catalogs, which provide the information needed to convert pixel coordinates to astronomical coordinates [14]. Modifying the existing filtering and processing methods aims to increase the validity of the observations and computed orbits, especially when tracking multiple unknown objects. Lubey, et al [15] have applied Thrust-Fourier-Coefficients to the classical Orbit Determination method and demonstrated real-world improvements in detecting object maneuvers. Delande, et al [16] presents the distinguishable

and independent stochastic populations filter, a multi-object tracking algorithm that exploits the Bayesian Filtering framework in the context of wide-area SSA.

One observation of the satellite returns only two angles, and three complete observations must be made for Initial Orbit Determination (IOD), which returns a first guess for an object's six-element orbit. Additional observations of the object can be added at a later time to improve the IOD solution by using a filtering method [17]. These techniques and methods will be explained in further detail in Chapter 2. These methods combined with accurate observations can provide very usable tracking information, but the computed orbits can only be as accurate and reliable as the observations themselves. Statistical methods can be used to determine the reliability of observation datasets.

Unfortunately, optical telescopes have many shortcomings: received signals may be faint and are subject to many factors once it enters the Earth's atmosphere. Ultimately, the quality of optical observations depends on the strength of illumination source (typically the sun), reflective properties of the satellite (material, shape, orientation), sensitivity of the sensor, and various losses of energy along the path of the light signal (attenuation, free path loss, etc.) [18]. Different operational procedures and equipment from station to station and variables in weather and atmosphere may also cause problems, such as scintillation (twinkling effect) or refraction (bending light). Because they contribute to known sources of error, these factors, both of the equipment and of the environment, must be considered when using observations from another site.

Statistical methods may be used to assess measurement quality and to filter noisy data in astrodynamics and space applications. Since there is such a large amount of data and information in tracking thousands of objects, research for improved SSA focuses heavily on studying applied statistical methods, particularly in the field of outlier detection. Outlier detection is heavily dependent on what quantities are known or unknown in a data set. This helps when deciding what quantities will be modeled as random variables. Statistical methods and neural networking are computationally

efficient methods that require users to know information such as error covariances a priori [19].

Often, in astronautics, a rough estimate or assumption is used for these methods. Testing and comparing variances within a data set can provide more information about the data set's usability. Variance tests, such as Levene's test, the Anderson-Darling test, and the Welch test [20] can test for the normality and linearity of a data set. This incidentally detects outliers as well. With a new data set of observations, performing initial orbit determination provides the necessary information to begin statistical methods, such as the Shapiro-Wilk test, which conducts robust distribution testing [21].

Since much of orbit determination and orbit improvement computations depend on assumptions on random variables, this thesis focuses on studying the effects of error distributions after adding nonlinear errors. Performing distribution tests can be particularly useful, especially since common filtering methods are not effective at detecting outliers. Using a robust statistical distribution test can confirm the goodness-of-fit of using Gaussian assumptions prior to moving forward with the potentially bad data. Significant deviations from a Gaussian distribution must then be considered an unreliable data set. The framework of this research is to provide methods to detect sources of errors within a provided data set. This requires repeatable methods for modeling error when given the conditions of a specific night. This thesis will focus on modeling errors and performing statistical distributions tests.

1.1 Research Goals

The first goal of this research is to model various errors associated with optical sensors using random variables. These errors include satellite timing error, ground station timing error, light refraction, and lens distortion. These all contribute to the uncertainty of an orbiting object's position. This research provides a reference of how different types of error at varying degrees translate to an object's position uncertainty.

Operators and users can share and receive data and use it more appropriately if they are more aware of observation uncertainties.

The second goal of the research is to provide a method for determining an incoming dataset's validity or usability without using additional information. Testing error distributions with statistical methods such as the Shapiro-Wilk test can reveal the presence of errors in a dataset or if the data should be used to update or improve existing orbits. This paper will focus on angles-only optical observations made from the ground.

1.2 Chapter Outline

Chapter 2: This chapter discusses and reviews the foundation and technical background necessary for understanding and simulating an object in orbit around the Earth. Here coordinate systems and reference frames for optical measurements and the two-body orbit problem are presented. Further, Gauss's initial orbit determination method is introduced as well as the Gauss least squares filtering method for batch orbit improvement.

Chapter 3: This chapter briefly introduces probability theory and how random variables can be used to express uncertainties in dynamical systems. Commonly used distribution shapes are described, and distribution tests are introduced, such as the Anderson-Darling test and the Shapiro-Wilk test.

Chapter 4: This chapter summarizes what methods and assumptions are made in modeling the various potential errors associated with optical observations, which revolve around timing, the processing and filtering of data, and equipment limitations. This consists of but is not limited to random and biased timing errors, opening and closing of the shutter, aberration, radial distortion, refraction error, centroid bias, etc. Once modeled, measurements can be shown with and without errors to begin

identifying trends and patterns.

Chapter 5: After modeling the errors, formal statistical methods from chatper 3 are applied to illustrate the effect of each error on a data set. Primarily, distribution testing will test for normality of the residuals in determine the validity or usability of a data set. Positive test results on the distribution testing may indicate a data set as unusable and that it should not be used for orbit update or improvement. However, the optical measurements with errors will be used in orbit determination and least squares filtering in order to demonstrate the errors' effects on orbit computation. This will highlight the strengths and limitations of the methods currently being used and ultimately stress the importance of understanding the errors associated with optical observations.

Chapter 6: Conclusions and recommendations are made.

2. REVIEW OF ASTRODYNAMICS

The detection of sources of observational errors in a data set requires a fundamental understanding of orbital motion, coordinate systems, and orbit determination methods. For this paper, assumptions and simplifications will be made about gravity and other perturbations as to highlight the effects of the optical error models, which will be presented in Chapter 4. This chapter discusses and reviews basic astrodynamics concepts that will be used in following chapters.

2.1 The Two-Body Problem

Objects in space are subject to the primary force of Earth's gravity, which keeps the objects in orbit. Of course, there are other forces, such as third-body effects (sun and moon), solar radiation pressure, atmospheric drag, Earth's oblateness, etc. Firstly, it is assumed in the two-body motion force model that the Earth is spherically symmetric and is perceived as a point mass. The space objects are also considered as point masses in the gravitational force model, but their masses are negligibly small compared to the mass of the Earth. This allows Newton's gravity inverse square law to be written as

$$\ddot{\bar{r}} = -\frac{GM_{\oplus}}{r^2}\frac{\bar{r}}{r}. \tag{2.1}$$

This represents the resultant acceleration of a space object due to gravity in Near-Earth Space as a vector, $\ddot{\bar{r}}$. $\bar{r}$ is the vector from the geocenter to the space object, and thus $\bar{r}/r$ is the unit vector pointing from the geocenter to the satellite. G and $M_{\oplus}$ are the universal gravitational constant and the mass of the Earth, respectively. It is common to use a gravitational parameter, $\mu_{\oplus} = GM_{\oplus}$. The gravity equation can then be written as

$$\ddot{\bar{r}} = -\frac{\mu_{\oplus}}{r^2}\frac{\bar{r}}{r}. \tag{2.2}$$

The value used for the Earth gravitational parameter, $\mu_\oplus$, is 398600.440 km^3/s^2. The above equations dictate the motion of an object in Earth's gravity in the two-body orbit problem [17]. The basic two-body gravity model can be expanded further with third-body perturbations. This is represented as a summation of the gravitational forces of the jth body acting on the primary body, Earth. For this, the point mass assumption and negligible object mass assumption still apply. Any number of third bodies can be used, but for Earth applications, it is most common to include the effects of the Sun and Moon.

$$\ddot{\bar{r}} = -\frac{\mu_\oplus}{r^2}\frac{\bar{r}}{r} - \sum_{j=1}^{n}\mu_j\left(\frac{\bar{r}-\bar{r}_j}{|\bar{r}-\bar{r}_j|^3} + \frac{\bar{r}_j}{r_j^3}\right) \tag{2.3}$$

From here, other perturbations, such as drag and solar radiation pressure (SRP) can be added to the force model, shown below. Drag is most applicable to satellites in LEO and is dependent on the drag coefficient, c_D, density of the air, ρ, the Area-to-Mass ratio (AMR), $\frac{A}{m}$, and it acts in the direction opposite of relative velocity v_r. SRP is more applicable for satellites in MEO or GEO, where smaller force have greater overall effect on an object's motion. It is dependent on the Sun-Earth distance, (AU for Astronomical Unit), the average SRP at 1 AU ($P_\odot \approx 4.56 \cdot 10^{-6} Nm^{-2}$), the AMR, $\frac{A}{m}$, the SRP coefficient, C_R, and the Sun-Earth vector,$\bar{r_\odot}$ More information on these equations can be found in Montenbruck's Satellite Orbits.

$$\bar{a}_{drag} = -\frac{1}{2}c_D\frac{A}{m}\rho\, v_r^2\frac{\bar{v_r}}{v_r} \tag{2.4}$$

$$\bar{a}_{SRP} = -P_\odot C_R\frac{A}{m}\frac{\bar{r_\odot}}{r_\odot^3}AU^2 \tag{2.5}$$

Unknown attitude or lack of information on object orientation, frontal area, mass, etc. can cause drag and SRP to be difficult to model and predict. Often the objects are modeled as spheres, but false assumptions in the force model lead to greater deviations from the truth when propagating

2.2 Coordinate Systems

In addition to the motion of the object(s) determined by the force model, a inertial reference frame is needed to correctly position the object in space and time. Then a coordinate system must be determined to describe the object's position within the decided reference frame. For coordinate systems, this research works primarily in the geocentric equatorial system, the topocentric equatorial system, and the local horizon equatorial system. The coordinate system used determines which angles are recorded during optical observations.

2.2.1 Earth Centered Inertial

For inertial reference, the Earth Centered Inertial (ECI) frame is used, which assumes the center of the Earth to be fixed inertially in space, In reality, it is slowly moving over time in relation to the sun and distant stars. However, if the focus of an object's dynamics is in Near-Earth Space, the ECI is often most appropriate. Propagation of Near-Earth objects is typically done in an ECI frame. Standardizing epoch and reference systems has proven useful, especially in sharing information. Currently, the use of the International Celestial Reference Plane (ICRF or J2000.0) is agreed upon. Here, the ECI reference plane is the Earth's equatorial plane, with the origin of the frame in the center of the Earth. The $\hat{x}$-axis points toward the mean vernal equinox, Υ, the $\hat{z}$-axis is normal to the reference plane and points through the Earth's axis of rotation, and the $\hat{y}$-axis completes the right-handed system as seen in Figure 2.1 [1].

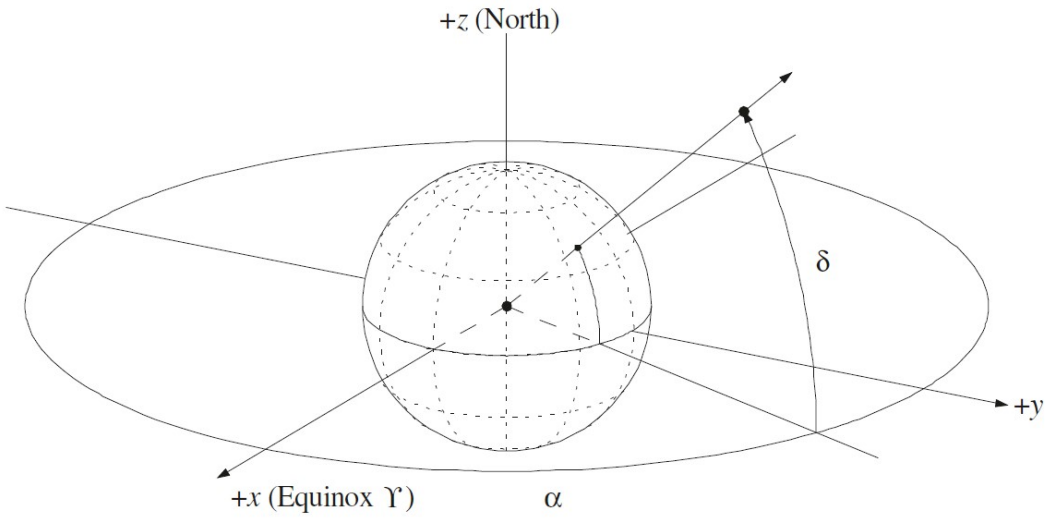

Fig. 2.1. The Equatorial Coordinate System with right ascension and declination labeled [1]

2.2.2 Geocentric Equatorial System

In the ECI frame, the position of a satellite can be described using the geocentric angles right ascension, α, and declination, δ, and the geocentric distance, r. α is the in-plane angle on the equatorial plane from $\hat{x}$ to the satellite (measured from 0° to 360°). δ is the angle above or below the equatorial plane (measured from -90° to 90°). This relationship between Cartesian components and the geocentric angles is described below in matrix form [18].

$$\bar{r} = \begin{bmatrix} x \\ y \\ z \end{bmatrix} = \begin{bmatrix} \cos\delta\cos\alpha \\ \cos\delta\sin\alpha \\ \sin\alpha \end{bmatrix} \tag{2.6}$$

2.2.3 Earth-Centered Earth-Fixed

Ground-based observers use a rotating reference frame, Earth-Centered and Earth-Fixed (ECEF) to describe their positions, where the primary direction is through Greenwich Meridian, the secondary direction is through 90°, and the normal direction is through the Earth's rotation axis. Rotating a position vector from the ECEF frame to ECI is achieved by rotating about the Earth's Rotation axis, $\boldsymbol{R_3}$. The angle used is Greenwich Mean Sidereal Time (GMST, or Θ), which is the angle of rotation past the $\hat{x}$-axis.

$$\bar{R}_{ECI} = \boldsymbol{R_3}(\Theta)\bar{R}_{ECEF} \tag{2.7}$$

In the ECEF frame, there are Topocentric Equatorial System and Topocentric Local Horizon System, which are both commonly used to describe a satellite's position in the sky from a ground-based sensor.

2.2.4 Topocentric Equatorial System

The Topocentric Equatorial System is a right-handed system with its origin at the topocenter, the position of the observer on the surface of the Earth at a specific time. The fundamental reference plane is parallel to the Earth's equator at a fixed equinox, and its reference direction is the vernal equinox at a fixed equinox. This illustration can be see in Figure 2.2. The angles used are topocentric right ascension, α', and topocentric declination, δ'. Use of the Topocentric Equatorial System also requires sidereal time, θ, which is the right of ascension of the zenith at the specified time t. The difference between sidereal time and geocentric right ascension provides the local hour angle, τ. In addition to the angles, the range, ρ, from topocenter to satellite, must be included to describe the position of the satellite.

$$\tau = \theta - \alpha' \tag{2.8}$$

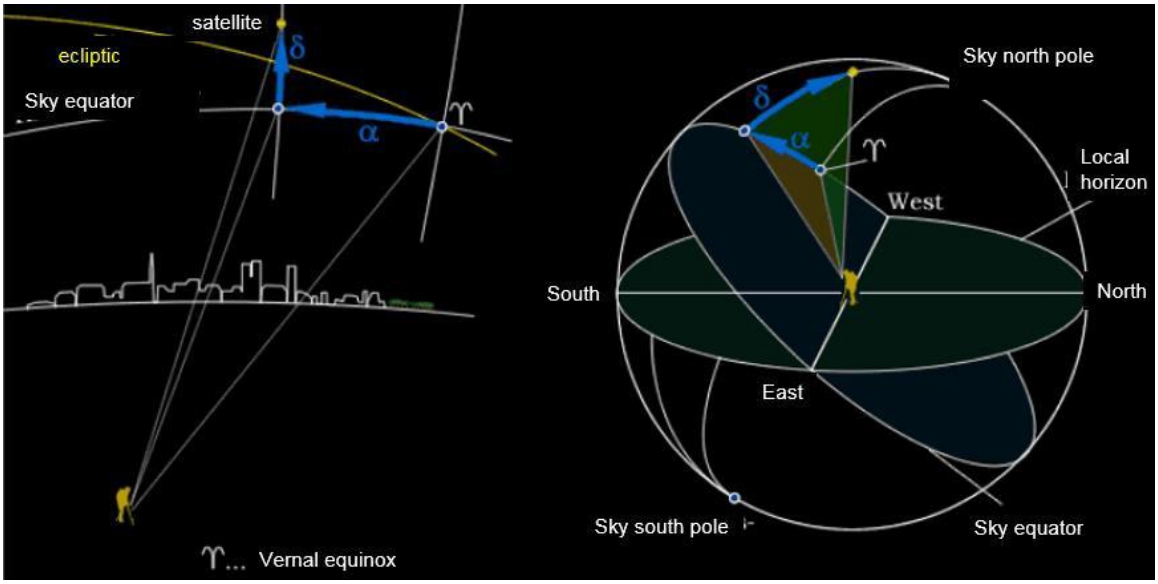

Fig. 2.2. The Topocentric Equatorial System with topocentric right ascension and topocentric declination labeled [18].

The observer's location must also be known and is defined using the geographic latitude (ϕ') of the observer and the average radius of the Earth $R' = 6,378km$. These values are used to make corrections which account for the non-spherical shape of the Earth.

$$\phi = \phi' - 0.1924^\circ \sin 2\phi' \tag{2.9}$$

$$R \approx R' - 21.38km \sin^2 \phi' \tag{2.10}$$

Then, the position of the topocenter can be converted to ECI using the corrected latitude and sidereal time:

$$\boldsymbol{R_{topo}} = \begin{bmatrix} R\cos\phi\cos\theta \\ R\cos\phi\sin\theta \\ R\sin\phi \end{bmatrix}, \tag{2.11}$$

and the topocentric vector is written as:

$$\bar{\rho} = \begin{bmatrix} \rho\cos\delta'\cos\alpha' \\ \rho\cos\delta'\sin\alpha' \\ \rho\sin\delta' \end{bmatrix}. \tag{2.12}$$

Using vector addition, $\bar{r} = \rho + R_{topo}$, the full transformation for topocentric vectors to geocentric ECI can be expressed as:

$$\begin{bmatrix} \cos\delta\cos\alpha \\ \cos\delta\sin\alpha \\ \sin\alpha \end{bmatrix} = \begin{bmatrix} \rho\cos\delta'\cos\alpha' \\ \rho\cos\delta'\sin\alpha' \\ \rho\sin\delta' \end{bmatrix} + \begin{bmatrix} R\cos\phi\cos\theta \\ R\cos\phi\sin\theta \\ R\sin\phi \end{bmatrix} \tag{2.13}$$

2.2.5 Topocentric Local Horizon System

The Topocentric Local Horizon System allows observers to make observations without requiring any computations since the origin and reference plane are local. It is a left-handed system, and the reference direction is South with the origin at the topocenter. The angles used are azimuth, Az, and elevation, h. Azimuth (measured from 0° to 360°) is the in-plane angle between the South reference direction and the satellite. Elevation (measured from 0° to 90°) is the angle above the local horizon. This is illustrated in Fig. 2.3.

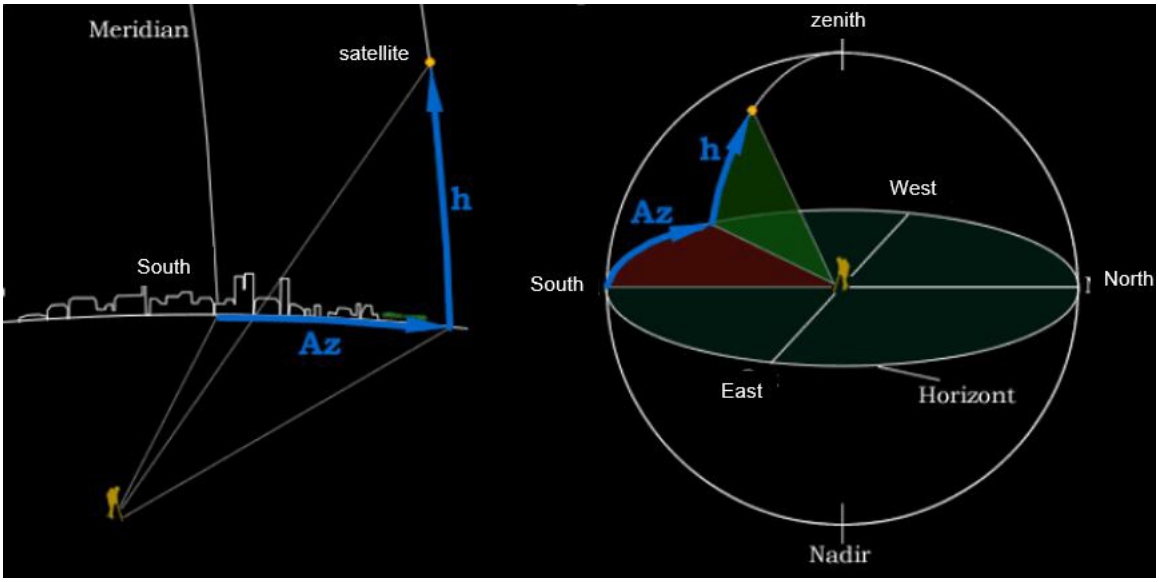

Fig. 2.3. The Topocentric Local Horizon System with Azimuth and Elevation labeled [18].

The azimuth and elevation can be computed using many of the values from above. The expression below uses corrected latitude, hour angle, topocentric right ascension,and topocentric declination.

$$\begin{bmatrix} \cos h \cos Az \\ \cos h \sin Az \\ \sin h \end{bmatrix} = \begin{bmatrix} \sin\phi \cos\delta' \cos\tau - \cos\phi \sin\delta' \\ \cos\delta' \sin\tau \\ \sin\phi \sin\delta' + \cos\phi \cos\delta' \cos\tau \end{bmatrix} \tag{2.14}$$

It is important to note here, that the Topocentric Local Horizon frame does not require using distances, only angles.

2.2.6 Radial, Along-Track, Cross-Track Reference Frame

At times, it may be useful to study the relative motion of satellites. If the true orbit of an object is known, its position can be used as the origin of a dynamic reference system. The direction opposite to the center of the Earth is the Radial

direction, $\hat{R}$. The along-track direction, $\hat{S}$, points in the direction of motion and is orthogonal to $\hat{R}$. The cross-track direction, $\hat{W}$, completes the right-handed system.

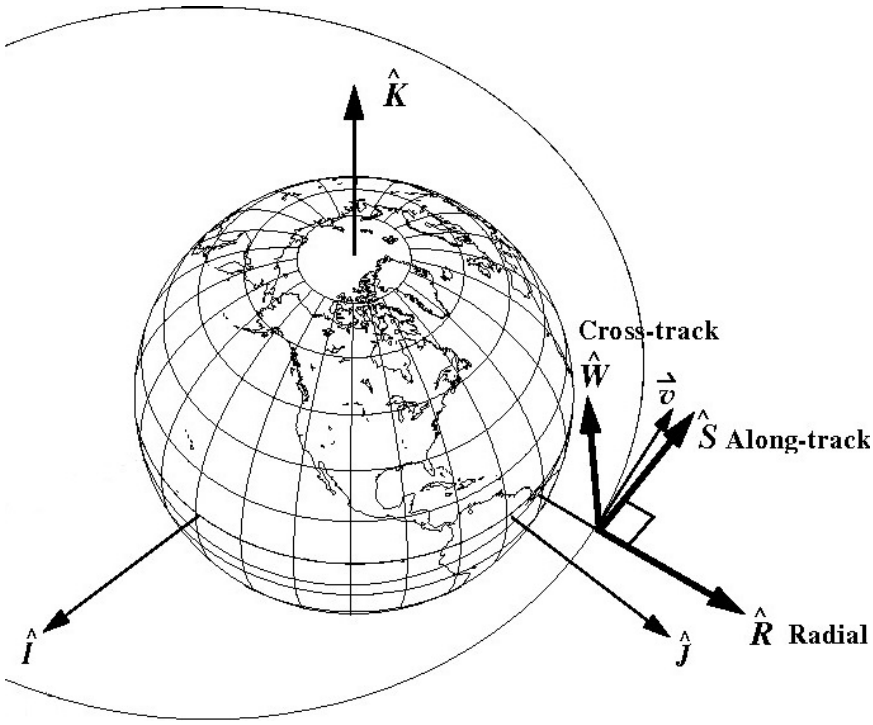

Fig. 2.4. The RSW Reference Frame [17].

From here, users can visualize the error in the context relative to the motion of the original object. The RSW reference frame is most commonly used to display orbit errors as well as proximity operations [17].

2.3 Classical Orbital Elements

Johannes Kepler, a 17th century astronomer, used six orbital parameters to describe the orientation, size, and shape of an orbit. These parameters are now known as Keplerian orbital elements or Classical Orbital Elements (COEs). Using the orbital element space can be helpful in understanding how the perturbations affect the orbit's overall size, shape, or orientation. Often, it can be easier for users to visualize and interpret any changes and differences in orbital elements, but generally speaking,

a full orbit must be known to compute the orbital elements. However, the aforementioned coordinate frames and reference systems allow observers to record information without knowing the full orbit. Orbit determination methods, which are discussed in the following section, use the observation space and returns a six-element state, position and velocity. The six components can then be used to compute the six COEs at a given time.

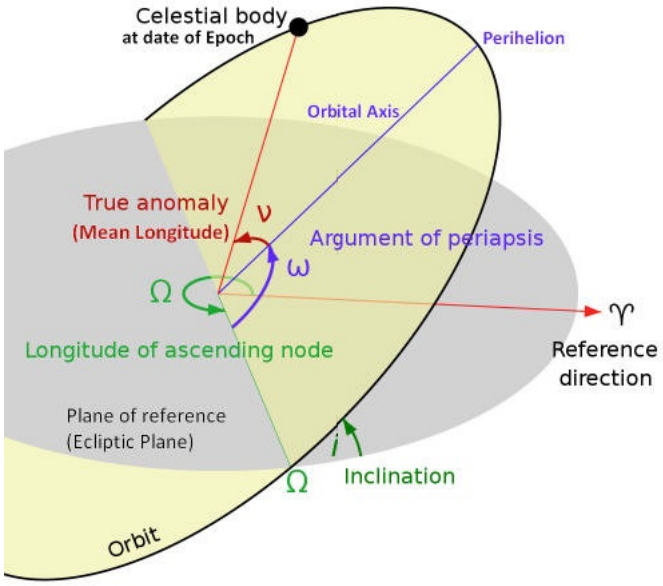

Fig. 2.5. The Classical Orbital Elements first used by Johannes Kepler [18].

a - The semi-major axis describes the size of the orbit. Specifically, it is half the sum of the periapsis and apoapsis distances: $a = (r_p + r_a)/2$.

e - The eccentricity describes the shape of the orbit. 0 indicates a circular orbit. Between 0 and 1, the orbit is elliptical. For Earth-orbiting objects, $0 \leqslant e < 1$.

i - The inclination is the angle between the orbital plane and the fundamental plane. It is measured between -90° and 90°. It defines the tilt of the orbit relative to the reference plane.

Ω - The Right Ascension of the Ascending node is the angle between the $\hat{x}$ and the point on the orbit at which the satellite crosses the equator from south to north. It defines the orientation of the orbital plane relative to the reference frame.

ω - The argument of periapsis is the angle in the orbital plane between the ascending node and periapsis. It defines the orientation of the orbit ellipse in the orbital plane.

ν - True anomaly describes the position of the orbiting object at a given time. It is the angle between periapsis and the position of the satellite in the orbital plane [1].

2.4 Orbit Determination

Once observations for an object are taken, the full orbit must be calculated. This requires knowing the observer's position as well as the time of the observations [18]. Since the orbit has six degrees of freedom, there must be six quantities taken from the observations. Generally, three observations are required to compute an orbit. This can provide good orbit estimates when observations are error-free, but using more observations to improve the initial solution ensures that the estimate is closer to the true orbit. Further observations are added via filtering methods, such as the Least Squares Method or the Extended Kalman Filter [17].

2.4.1 Initial Orbit Determination: Gauss's Method

Initial Orbit Determination (IOD) is the method of determining the full state of a object in orbit, using only observations. This work uses Gauss's IOD method, which uses three angles-only observations to determine the six-element state vector for the object and does not require any distance measurements. This method assumes the object's motion is planar and projects the solution onto the second observation [18]. To begin, there must be three observations in the topocentric frame, each with the

time of observation:

$$\begin{bmatrix} t_1, \alpha_1, \delta_1 \\ t_2, \alpha_2, \delta_2 \\ t_3, \alpha_3, \delta_3 \end{bmatrix}$$

The observations are used to create the pointing direction, $\hat{L}_i$, at each time:

$$\hat{L}_i = \begin{bmatrix} \cos\alpha_i \cos\delta_i \\ \cos\alpha_i \sin\delta_i \\ \sin\delta_i \end{bmatrix} \tag{2.15}$$

Combined with the observers position at each in the ECI frame, there is enough information to determine the orbit. The observer position is recorded in matrix form:

$$\boldsymbol{R_i} = \boldsymbol{R_{observer,ECI}} \tag{2.16}$$

The position of the observed object can be expressed as:

$$r_i = R_i + \rho_i \cdot \hat{L}_i, \tag{2.17}$$

and the only unknowns are the slant ranges for each observation, ρ_i.

Below are the equations and procedure needed to complete Gauss's Method. The method uses the available quantities and geometric restrictions (planar conic section) to solve for the missing ranges algebraically. More information on the derivations of the formulas can be found in Vallado's text, *Fundamentals of Astrodynamics and Applications*.

- Time Intervals Between Observations

$$\begin{bmatrix} \tau_1 = t_1 - t_2 \\ \tau_3 = t_3 - t_2 \\ \tau_{13} = \tau_3 - \tau_1 \end{bmatrix} \tag{2.18}$$

- Triple Products:

$$\begin{bmatrix} D_0 = \hat{L}_1 \cdot (\hat{L}_2 \times \hat{L}_3) \\ D_{11} = R_1 \cdot (\hat{L}_2 \times \hat{L}_3);\ D_{21} = R_2 \cdot (\hat{L}_2 \times \hat{L}_3);\ D_{31} = R_3 \cdot (\hat{L}_2 \times \hat{L}_3) \\ D_{12} = R_1 \cdot (\hat{L}_1 \times \hat{L}_3);\ D_{22} = R_2 \cdot (\hat{L}_1 \times \hat{L}_3);\ D_{32} = R_3 \cdot (\hat{L}_1 \times \hat{L}_3) \\ D_{13} = R_1 \cdot (\hat{L}_1 \times \hat{L}_2);\ D_{23} = R_2 \cdot (\hat{L}_1 \times \hat{L}_2);\ D_{33} = R_3 \cdot (\hat{L}_1 \times \hat{L}_3) \end{bmatrix} \tag{2.19}$$

- A and B coefficients:

$$A = \frac{1}{D_0}\left[-\frac{\tau_3}{\tau_{13}}D_{12} + D_{22} + \frac{\tau_1}{\tau_{13}}D_{32}\right] \tag{2.20}$$

$$B = \frac{1}{6D_0}\left[-(\tau_{13}^2 - \tau_3^2)\frac{\tau_3}{\tau_{13}}D_{12} + (\tau_{13}^2 - \tau_1^2))\frac{\tau_1}{\tau_{13}}D_{32}\right] \tag{2.21}$$

- a, b, c coefficients:

$$a = -A^2 - 2A(\hat{L}_2 \cdot R_2) - ||R_2||^2 \tag{2.22}$$

$$b = -2\mu B(A + (\hat{L}_2 \cdot R_2)) \tag{2.23}$$

$$c = -\mu^2 B^2 \tag{2.24}$$

- Solve for the real root, $||r_2||$:

$$0 = ||r_2||^8 + a||r_2||^6 + b||r_2||^3 + c \tag{2.25}$$

- use $||r_2||$ to determine the slant ranges:

$$\rho_1 = \frac{1}{D_0}\left[\frac{6(D_{31}\frac{\tau_1}{\tau_3} + D_{21}\frac{\tau_{13}}{\tau_3})||r_2||^3 + \mu D_{31}(\tau_{13}^2 - \tau_1^2)\frac{\tau_1}{\tau_3}}{6||r_2||^3 + \mu(\tau_{13}^2 - \tau_3^2)} - D_{11}\right] \tag{2.26}$$

$$\rho_2 = A + \mu B||r_2||^{-3} \tag{2.27}$$

$$\rho_1 = \frac{1}{D_0}\left[\frac{6(D_{13}\frac{\tau_3}{\tau_1} + D_{23}\frac{\tau_{13}}{\tau_1})||r_2||^3 + \mu D_{13}(\tau_{13}^2 - \tau_3^2)\frac{\tau_3}{\tau_1}}{6||r_2||^3 + \mu(\tau_{13}^2 - \tau_1^2)} - D_{33}\right] \tag{2.28}$$

- Using Lagrange Coefficients, the position and velocity at the second observation can be determined:

$$f_1 = 1 - \frac{1}{2}\frac{\mu}{||r_2||^3}\tau_1^2 \tag{2.29}$$

$$f_3 = 1 - \frac{1}{2}\frac{\mu}{||r_2||^3}\tau_3^2 \tag{2.30}$$

$$g_1 = \tau_1 - \frac{1}{6}\frac{\mu}{||r_2||^3}\tau_1^3 \tag{2.31}$$

$$g_3 = \tau_3 - \frac{1}{6}\frac{\mu}{||r_2||^3}\tau_3^3 \tag{2.32}$$

$$\bar{r_i} = R_i + \rho_i \hat{L}_i \tag{2.33}$$

$$\bar{v_2} = \frac{1}{f_1\, g_3 - f_3\, g_1}\left[f_1 r_3 - f_3 r_1\right] \tag{2.34}$$

Once the position and velocity are determined, the equations of motion can be used to propagate the object forwards or backwards to a desired time [18].

2.4.2 Orbit Improvement: Least Squares Method

For real-world applications, the IOD provides only a rough estimate for an object's orbit and should be treated as an incomplete solution. For higher precision, a filtering method using more observations is necessary. In cases where observations are used singly, or as they are recorded, a sequential filter, like the Extended Kalman Filter, is most approriate. More information on the Kalman Filter can be found in Vallado's *Fundamentals of Astrodynamics and Applications*. However, for data sharing, it would be most common to receive a full set of observations from a ground station, so in this study, the orbit improvement of choice is the classical batch filter, or the Least Squares Estimator [18].

Linear Least Squares

The Least Squares method begins with defining the state, $\boldsymbol{x}$. For an object in the orbit problem, the state is a six-element vector of the position and velocity components:

$$\boldsymbol{x^T} = \Big[r_x, r_y, r_z, v_x, v_y, v_z\Big] \tag{2.35}$$

Once the state vector is defined, the model, $\boldsymbol{g_i}$ is expressed as a linear combination of the state and a measurement matrix, $\boldsymbol{H_i}$.

$$\boldsymbol{g_i} = \boldsymbol{H_i x} \tag{2.36}$$

For system with known dynamics, a state transition matrix, $\Phi_{(t_k,t_0)}$, is used to propagate the initial state to time, t_k, of measurement observation. The first time derivative of the state transition matrix, $\dot{\Phi}_{(t,t_i)}$ must also be known. If the system dynamics are known to follow

$$\dot{\boldsymbol{x}}(t) = \boldsymbol{F}(t)\boldsymbol{x}(t), \qquad \boldsymbol{x}(t_0) = \boldsymbol{x_0}, \tag{2.37}$$

then,

$$\dot{\boldsymbol{\Phi}}_{\boldsymbol{(t,t_i)}} = \boldsymbol{F(t)\Phi_{(t,t_i)}} \tag{2.38}$$

The measurement matrix, $\boldsymbol{H}$ model would then be expressed as:

$$\boldsymbol{H_k} = \boldsymbol{\tilde{H}_k \Phi_{(t_k,t_0)}}, \tag{2.39}$$

where $\boldsymbol{\tilde{H}_k}$ is a measurement mapping matrix. The driving factor of the method is the minimization the variance in the residuals between the real observations and the estimates generated by the model. The residuals are recorded as:

$$\boldsymbol{\epsilon_i} = \boldsymbol{z_i} - \boldsymbol{H_i x}, \tag{2.40}$$

where $\boldsymbol{z_i}$ is the matrix of true observations. The method minimizes a performance index, J, which is the sum of squares. This can also be called the weight, hence the name, Weighted Least Squares. In matrix form, it is expressed as:

$$J = -2\left[\boldsymbol{z} - \boldsymbol{Hx}\right]^T\left[\boldsymbol{z} - \boldsymbol{Hx}\right] \tag{2.41}$$

To find the minimum of J, the first derivative is taken with respect to x:

$$\frac{\partial J}{\partial \boldsymbol{x}} = -2\left[\boldsymbol{z} - \boldsymbol{H}\boldsymbol{x}\right]^T \boldsymbol{H}, \tag{2.42}$$

which is set to equal 0.

$$\left[\boldsymbol{z} - \boldsymbol{H}\boldsymbol{x}\right]^T \boldsymbol{H} = \boldsymbol{0}^T \quad \rightarrow \quad \boldsymbol{z}^{\boldsymbol{T}}\boldsymbol{H} - \boldsymbol{x}^{\boldsymbol{T}}\boldsymbol{H}^{\boldsymbol{T}}\boldsymbol{H} = \boldsymbol{0}^{\boldsymbol{T}} \tag{2.43}$$

Rearranging the terms provides:

$$\boldsymbol{H}^{\boldsymbol{T}}\boldsymbol{H}\boldsymbol{x} = \boldsymbol{H}^{\boldsymbol{T}}\boldsymbol{z} \tag{2.44}$$

Solving for the state yields the final equation for $\hat{\boldsymbol{x}}$:

$$\hat{\boldsymbol{x}} = \left[\boldsymbol{H}^{\boldsymbol{T}}\boldsymbol{H}\right]^{-1}\boldsymbol{H}^{\boldsymbol{T}}\boldsymbol{z} \tag{2.45}$$

To ensure the Least Squares method provides an estimate that is unbiased with minimum variance, measurement error must be introduced. Each observation is assumed to have some measurement error, $\boldsymbol{\nu_i}$, of which the mean is 0 and the expected value of the covariance, $\boldsymbol{R_{ij}}$ is known.

$$\boldsymbol{z_i} = \tilde{\boldsymbol{H}}_{\boldsymbol{i}}\boldsymbol{x_i} + \boldsymbol{\nu_i} \tag{2.46}$$

$$E\{\boldsymbol{\nu_i}\} = 0 \tag{2.47}$$

$$E\{\boldsymbol{\nu_i}\boldsymbol{\nu_j^T}\} = \boldsymbol{R_{ij}} \tag{2.48}$$

In summary, the estimated state is assumed to be a linear combination of the measurement data and the known error and covariance. This also assumes that the estimated state is random even though the true state of the system is not random [18]. The covariance matrix, $\boldsymbol{P_k}$, is also updated.

$$\hat{\boldsymbol{x_k}} = \left[\boldsymbol{H}^{\boldsymbol{T}}\boldsymbol{R}^{-\boldsymbol{1}}\boldsymbol{H}\right]^{-\boldsymbol{1}}\boldsymbol{H}^{\boldsymbol{T}}\boldsymbol{R}^{-\boldsymbol{1}}\boldsymbol{z} \tag{2.49}$$

$$\boldsymbol{P_k} = \left[\boldsymbol{H}^{\boldsymbol{T}}\boldsymbol{R}^{-\boldsymbol{1}}\boldsymbol{H}\right]^{-\boldsymbol{1}} \tag{2.50}$$

The full derivation for Eq.2.47 and Eq. 2.48 can be found in Chapter 7, section 2 of Frueh's AAE 590 script.

Nonlinear Least Squares

Unfortunately, the above method does not work when the dynamics of a system, like that of the orbit problem, are nonlinear. Here, the dynamics must be linearized for use in the Least Squares method. The mapping matrices and the state transition matrix use Taylor Series expansion with negligible higher order terms. The matrices needed for the two-body orbit problem can be found in Appendix D of Vallado's *Fundamentals of Astrodynamics and Applications*.

Because of the linearizations, the measurements and estimated state are assumed to have deviations from the truth. The deviations can be expressed with δ, where

$$\delta\, \boldsymbol{x}(\boldsymbol{t}) = \boldsymbol{x}(\boldsymbol{t}) - \boldsymbol{x}^*(\boldsymbol{t}), \tag{2.51}$$

and x^* is a reference state. Likewise, the deviations in the measurements can be expressed as

$$\delta \boldsymbol{z_i} = \boldsymbol{z_i} - \boldsymbol{z_i^*}, \tag{2.52}$$

and differentiating once with respect to time gives

$$\delta \dot{\boldsymbol{x}}(\boldsymbol{t}) = \boldsymbol{x}(\boldsymbol{t}) - \boldsymbol{x}^*(\boldsymbol{t}) \tag{2.53}$$

and

$$\delta \boldsymbol{z_i} = \boldsymbol{h}(\boldsymbol{x_i}) - \boldsymbol{h}(\boldsymbol{x}^*) + \boldsymbol{\nu_i}. \tag{2.54}$$

Linearizing with a first-order Taylor series expansion and removing like terms gives

$$\delta \dot{\boldsymbol{x}}(\boldsymbol{t}) = \boldsymbol{F}(\boldsymbol{x}^*(\boldsymbol{t}))\boldsymbol{\delta x}(\boldsymbol{t}) \tag{2.55}$$

and

$$\delta \boldsymbol{z_i} = \tilde{\boldsymbol{H}}(\boldsymbol{x_i^*})\boldsymbol{\delta x_i} + \boldsymbol{\nu_i}. \tag{2.56}$$

.

New terms, λ and Λ, are defined using the available terms:

$$\boldsymbol{\lambda} = \boldsymbol{\bar{P}_k^{-1}}\boldsymbol{\delta \bar{x}_k} + \boldsymbol{H^T R^{-1}}\boldsymbol{\delta z} \tag{2.57}$$

$$\boldsymbol{\Lambda} = \boldsymbol{\bar{P}_k^{-1}} + \boldsymbol{H^T R^{-1}} \tag{2.58}$$

Now the solution can be found with

$$\boldsymbol{\Lambda \delta \hat{x}_k} = \boldsymbol{\lambda}, \tag{2.59}$$

and the state estimate, $\boldsymbol{\hat{x_k}}$ can be expressed as

$$\boldsymbol{\delta \hat{x}_k} = \boldsymbol{\Lambda^{-1} \lambda} \tag{2.60}$$

The covariance is returned as

$$\boldsymbol{P_k} = \boldsymbol{\Lambda^{-1}} \tag{2.61}$$

The state estimate and covariance estimate, which contain both position and velocity, are reset and reused in the next iteration of the least squares estimator. Iterations can be run until a desired convergence is reached. Ultimately, the method remains largely similar, and only a few modifications must be made for nonlinear system dynamics. This is an abridged summary of the nonlinear least squares method. The solution for the nonlinear system is abbreviated as NLUMVE, or Nonlinear Unbiased, Minimum Variance Estimate. The full derivation can be found in Chapter 7, section 3 of Frueh's AAE 590 script.

3. PROBABILITY AND STATISTICAL METHODS

The foundation of error modeling and analysis relies on an understanding of random variables and probability distributions. Random variables capture uncertainties that may be present in observations or in the orbit model. Random variables allows users to represent uncertainties mathematically [22]. This chapter introduces and discusses probability distributions and the random variables, which can be used in statistical methods, which are covered later in Chapter 5.

3.1 Basic Probability and Random Variables

A random variable can be described as a possible set of values for given conditions. From the possible set of values, the outcome of the random variable follows a random probability distribution. For continuous random variables, the probability density function, $p(x)$, expresses the relative likelihoods for which values within the possible set the random variable may take. The expected value of a random variable, x, when continuous, can be expressed explicitly when the probability density function is known. It is the sum of all possible random outcomes represented by an integral and is equal to the mean, μ, or the average value of all outcomes:

$$E\{x\} = \int_{-\infty}^{\infty} xp(x)dx = \mu \tag{3.1}$$

Moments in statistics are useful parameters that describe the shapes of distributions. The nth moment of x is defined using expected values: $E\{x^n\}$, shown in Eq. 3.1. It can be seen then that the first moment ($n = 1$) is equal to the mean. The second moment, which describes the variance of a distribution, can be calculated using the second moment [22].

$$Var\{x\} = E\{x^2\} - E\{x\}^2 \tag{3.2}$$

In a case with two random variables, x and y for example, the joint variance, or covariance, can be expressed as

$$Var\{xy\} = E\{xy\} - E\{x\}E\{y\} \tag{3.3}$$

Some probability distributions require two or moments to describe the full shape of the distribution. Examples are discussed below.

3.1.1 Normal Distribution

The Normal Distribution, or Gaussian Distribution, is a bell-shaped, continuous distribution symmetric about the mean (see figure 3.1) and can be described in full using the first moment, μ and the second moment, σ^2. The probability density function is expressed as

$$f(x) = \frac{1}{\sqrt{2\pi\sigma^2}} \exp\left(\frac{(x-\mu)^2}{2\sigma^2}\right) \tag{3.4}$$

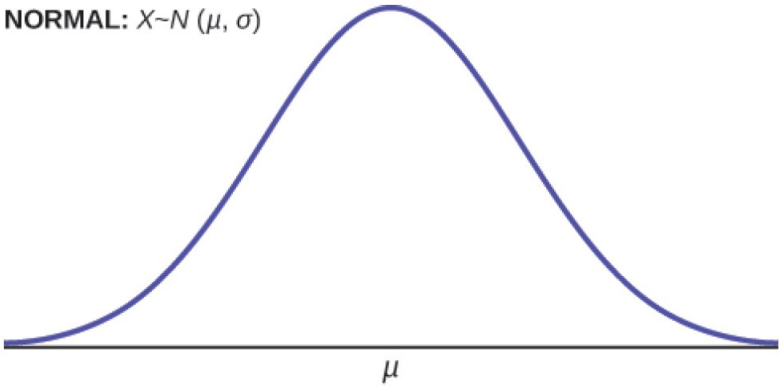

Fig. 3.1. The Normal Distribution Curve [22].

This distribution is widely used in statistics in conjunction with the Central Limit Theorem, which postulates that, for a given sample of size n, the random variables,

sample mean $\bar{X}$ and sample sum ΣX, both follow normal distributions when n is sufficiently large:

$$\bar{X} \sim N(\mu, \frac{\sigma^2}{n}) \tag{3.5}$$

$$\Sigma X \sim N(n\mu, n\sigma^2) \tag{3.6}$$

This holds true even when the population distribution does not follow a normal distribution. This is particularly useful when modeling uncertainties in a dynamical system. The distributions of the uncertainties may be unknown, but in a large enough sample, they can be assumed to be normal [22].

3.1.2 Poisson Distribution

In astrodynamics, photons arriving at the optics of a telescope are known to follow a specific random distribution, the Poisson distribution. The Poisson distribution gives the probability of an event occurring in a fixed interval of time. It is important to note that this is a discrete probability function, meaning it can only take the value of positive counting numbers (see figure 3.2). If the average rate, λ, is known, the probability function of a random variable can be expressed as

$$P(x) = \frac{\lambda^x \exp(-\lambda)}{x!} \tag{3.7}$$

The Poisson distribution is an example of a distribution that can be described using only the first moment since both the mean and variance are equal to λ.

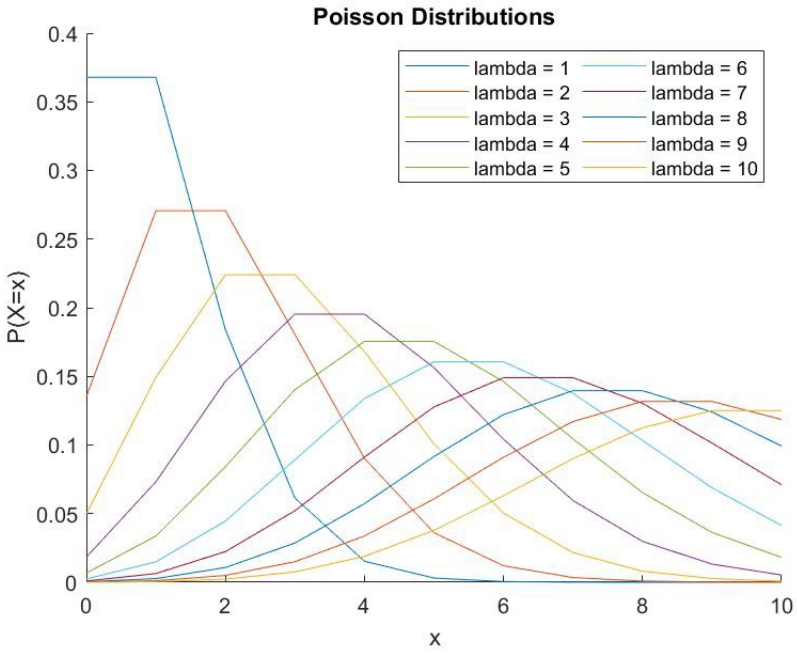

Fig. 3.2. This illustrates the effect of λ on the shape of the distribution.

Users and analysts must determine if applying nonlinear transformations to random variables is appropriate. For example, the normal distribution retains its normality in a linear transformation, but applying a nonlinear transformation may change the overall shape of the distribution. Hence, the transformations themselves may be linearized or approximated for appropriate application. On the similar note, since the Poisson distribution is discrete, transformations may lead to non-Poisson distribution of the random variable. In this case, the Poisson distribution can be approximated using a normal distribution, and then linear transformations would be preserve the distribution [22].

3.2 Distribution Testing

When observations or sets of data are received from a ground station, distribution testing can be performed to validate the measurements' usability. The errors are assumed to follow the distributions of the random variables modeled in chapter 4,

and incoming error distributions can be tested for outliers or irregularities using the knowledge of expected error distribution. This is especially applicable when information sharing and statistical parameters for the data sets are unknown. Information sharing networks may have measurements ranging from amateur to state-of-the-art, and the appropriate assumptions can be made based on the models in chapter 4.

3.2.1 Anderson-Darling Test

The Anderson-Darling test is a formal statistical method that is used to determine if the empirical distribution of a data set follows another known distribution. This is a simple way of checking a distribution for normality and can also work for identifying outliers if the sample size n is small. The test begins with random variable X, which is assumed to follow a normal distribution with known mean, μ, and variance, σ^2. The normal distribution follow $F_X(x;\theta)$, where θ is a known parameter, or set of parameters, that define the distribution. For a 1-dimensional problem, $\theta = (\mu, \sigma^2)$. The sample from X of size n follows the distribution $F_n(x)$. The Anderson-Darling test statistic, A^2, is given by a weighted sum of the squares of the differences in standard deviations:

$$A^2 = \frac{1}{n}(\sum_{i=1}^{n}(F_X(x;(\mu,\sigma^2)) - F_n(x))^2 \tag{3.8}$$

The A^2 test statistic is a random variable that follows an asymptotic distribution. A user-defined significance level, α, determines the threshold p-value that triggers a positive test result. This research focuses on normal distributions, but the Anderson-Darling test has a wide-range of applicability as the distributions are defined by the user, including poisson, exponential, logistic, gamma distribution etc. It is a simple yet effective test for testing for normality and outliers [23].

3.2.2 Shapiro-Wilk Test

Similar to the Anderson-Darling test but more robust, the Shapiro-Wilk distribution test was founded by Samuel Shapiro and Martin Wilk in 1965. It is a goodness-of-fit test that tests for the deviation of an empirical distribution from another known, user-specified distribution. Most commonly, it is used to test for normality in a data set. As before, the test begins with a random variable, X, which is assumed to follow a normal distribution with mean, μ, and variance, σ^2. The test statistic, W, is computed:

$$W = \frac{(\sum_{i=1}^{n} a_i x_{(i)})^2}{\sum_{i=1}^{n}(x_i - \bar{x})^2} \tag{3.9}$$

Here, $x_{(i)}$ is the ith order statistic, and x_i is from the sample. $\bar{x}$ is the sample mean. The coefficients a_i are given by $(a_1, ..., a_n) = \frac{m^T V^{-1}}{C}$, where $C = \parallel V^{-1}m \parallel$. The vector $m = (m_1, ..., m_n)$ is made of the expected values of the order statistics of independently and identically distributed random variables, and V is the covariance matrix of those random variables.

The Shapiro-Wilk test then is a correlation test between the data and expected normal scores using the empirical variances and the expected variances. The test statistic W is a ratio of how closely the distribution follows normal. For example, a perfectly normal distribution has a test statistic of $W = 1$, and deviations from normal drive the value down. The Shapiro-Wilk test is well-known for its robustness and applicability. Like the Anderson-Darling test, the user can specify any distribution with known order statistics [21]. Though the Shapiro-Wilk test is known to be more robust than the Anderson-Darling test, it is more difficult to implement and requires more information in the order statistics. For this paper, the Shapiro-Wilk test is used as it is known to be more robust.

4. SOURCES OF ERROR

Orbit tracking and propagation are not exact: between the physical equipment and environment, processing and filtering, and propagation modeling, there are many sources of error and uncertainties. As assumptions and simplifications are made in these processes, a modeled object's state and its true state will differ. In other words, only the probability density function of the object's state can be determined, and wrong assumptions can result in deviations from the true assumptions. The errors studied in this research include optical errors, timing errors, and other potential errors relevant to the operation of ground-based optical observations. Some of these errors can be modeled as random variables using the fundamentals of astrodynamics and statistical probability reviewed in the previous chapters. The nonlinearity of the orbital dynamics causes the uncertainties to change with time and drives the need to make frequent updates with new observations. This chapter discusses stochastic and systematic errors. Stochastic errors are random and cause fluctuations about the true value, whereas systematic errors result in predictable and consistent biases from the truth often as a result of poorly calibrated equipment. Identifying and understanding both stochastic and systematic errors are critical to accurately representing an object state's uncertainty.

4.1 Optical and Equipment Errors

Each observation consists of three basic parts: the observer position, the time of observation, and the pointing direction from sensor to object. Optical errors are directly associated with the angles in this pointing direction. These angles are subject to deviations, or errors, which can be minimized with careful operational procedures and processing, but they cannot be eliminated. Measurement errors are an inherent

part of the observation process.As a reminder, the pointing direction can be expressed as

$$\hat{L}_i = \begin{bmatrix} \cos\alpha_i \cos\delta_i \\ \cos\alpha_i \sin\delta_i \\ \sin\delta_i \end{bmatrix},$$

where α_i and δ_i are topocentric right ascension and declination, respectively. This pointing direction is measured from the center of a camera's field of view (FOV). For the observation of near-Earth objects, FOV ranges from 0.5x0.5 degree to 8.0x8.0 degree pixel grids, and pixel scales vary between 0.5 arcseconds to several arcseconds per pixel [18]. The resultant angle measurements for an object are computed using the pixel grid and telescope pointing direction. For example, if the center of an object is determined to be in pixel (x, y), then the corresponding pixel scales, δ_x and δ_y, are used to adjust α_i and δ_i:

$$\alpha_{adj} = \alpha_i + x \cdot \delta_x \tag{4.1}$$

$$\delta_{adj} = \delta_i + y \cdot \delta_y \tag{4.2}$$

4.1.1 Pixel Position Uncertainty

Depending on the size and intensity of the light, the received signal can be spread across many pixels, and determining the true centroid of an image can be very difficult due to limited pixel resolution and background noise. An example of an object shown as a faint streak of light is shown in Fig. 4.1.

The quality of the equipment and image processing can improve the signal-to-noise-ratio (SNR), which results in a crisper image; however, determining the exact centroid of a bright signal is still difficult. In this context, pixel position uncertainty using the parameters of a two-dimensional Gaussian model:

$$f = A \ \exp\left[-\frac{1}{2}(c_1(x-x_0)^2 + 2c_3(x-x_0)(y-y_0) + c_2(y-y_0)^2)\right] \tag{4.3}$$

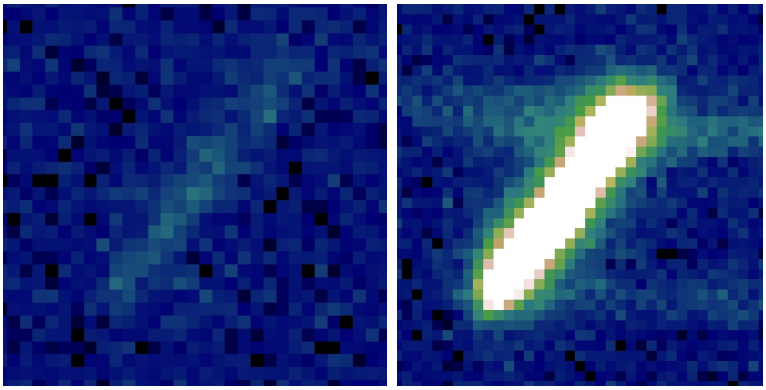

Fig. 4.1. Uncertainties in determining the centroid of a faint signal will cause observation angle errors. On the right is the same object with an improved SNR [18].

Here, A defines the amplitude of the Gaussian fit, c_1 and c_2 define the size of the Gaussian fit in the x, y directions, c_3 orients the fit with respect to the xy-plane, and x_0, y_0 locate the center of the Gaussian in the image. Once these parameters are estimated, the inverse of the Fisher Information Matrix, which quantifies the lower bound of the pixel position uncertainty, can be determined:

$$K_{x_0,y_0} = \frac{\delta_x \delta_y}{(\mathrm{SNR})^2 \sqrt{D\pi^3}} * \\ * \begin{bmatrix} 2c_2(\sqrt{\pi} + 2\sqrt{\frac{D}{c_2}} a d_a + 2\sqrt{\frac{D}{c_1}} \rho^2 b d_b), & -2c_3(\sqrt{\pi} + 2\sqrt{\frac{D}{c_2}} a d_a + 2\sqrt{\frac{D}{c_1}} \rho^2 b d_b) \\ -2c_3(\sqrt{\pi} + 2\sqrt{\frac{D}{c_2}} a d_a + 2\sqrt{\frac{D}{c_1}} \rho^2 b d_b), & 2c_1(\sqrt{\pi} + 2\sqrt{\frac{D}{c_1}} b d_b + 2\sqrt{\frac{D}{c_2}} \rho^2 a d_a) \end{bmatrix} \tag{4.4}$$

Eq. 4.2 does require the parameters of the CCD and signal truncation. δ_x, δ_y are the pixel scales in the respective x and y directions. $\mathrm{SNR} = \frac{A\delta_x\delta_y}{\sigma}$, and σ is the standard deviation of the background subtracted signal. D is the determinant ($D = c_1c_2 - c_3^2$). $\rho = -\frac{-c_3}{\sqrt{c_1 c_2}}$ is a correlation factor between the x, y axes. a and b are image truncation parameters in the x and y directions. $d_a = \exp -\frac{Da^2}{c_2} D$ and $d_b = \exp -\frac{Db^2}{c_1} D$. More information on this equation and its derivation can be found in papers by Sanson and Frueh [24] [25]. Fig. 4.2 demonstrates the strong inverse relationship between pixel uncertainty and SNR.

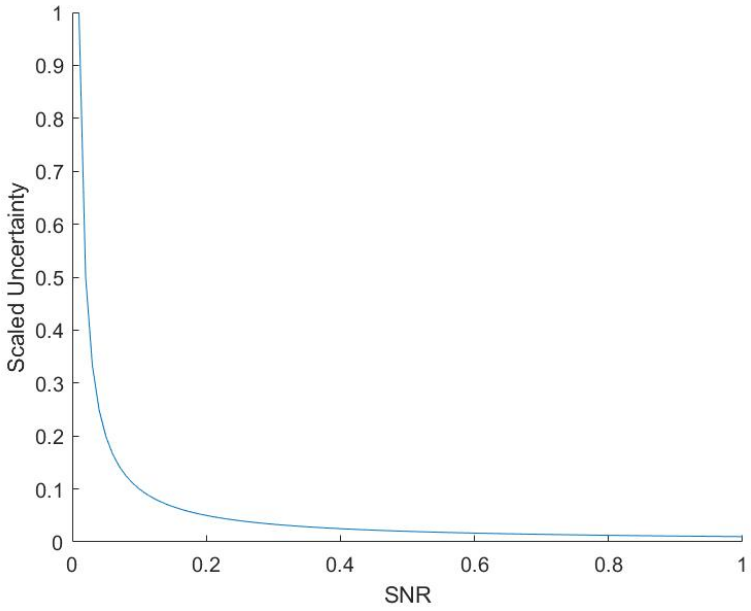

Fig. 4.2. Uncertainty is scaled to demonstrate the impact the effect of SNR.

4.1.2 Lens Distortion

Other equipment-related problems can be found in the physical optics in sensors. Due to the spherical nature of lenses and mirrors, light passing through the optics is bent or distorted in a radial fashion. Different paths of the signal are bent in varying degrees and do not arrive at the same point simultaneously unless physically corrected. Examples of distorted images can be seen in Fig. 4.3.

This radial distortion must be corrected in the processing stage. The distortion can be modeled as a radial function using the x and y coordinates of the pixel grid [26]:

$$r_u(x_u, y_u) = r_d(x_d, y_d)(1 + kr_d(x_d, y_d)^2), \tag{4.5}$$

where the subscripts d and u denote distorted and undistorted values, and k is the distortion parameter. This relationship is then used to find an expression for the distortion correction. Each lens and application will have its own parameters and

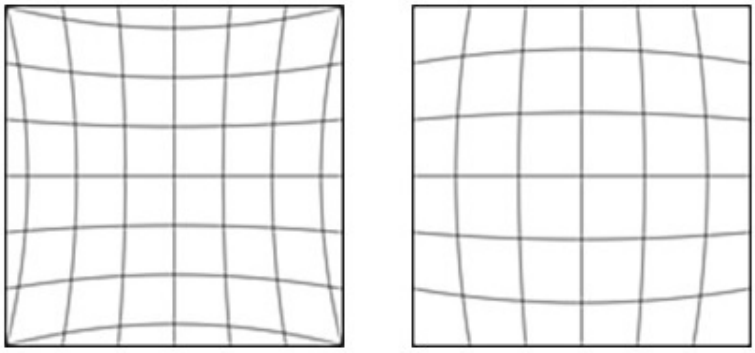

Fig. 4.3. Pincushion distortion is shown on the left, and barrel distortion is shown on the right [26].

distortion models. Here is simplified example of what radial distortion corrections may look like:

$$x \text{ distortion} = x(kx^2 + ky^2 + 1) \tag{4.6}$$

$$y \text{ distortion} = y(kx^2 + ky^2 + 1) \tag{4.7}$$

A positive k is used to correct pincushion distortion, and a negative k is used to correct barrel distortion. Eq. 4.4 and Eq. 4.5 were used to create the plots in Fig. 4.3 using $k = 0.1$ and $k = -0.1$.

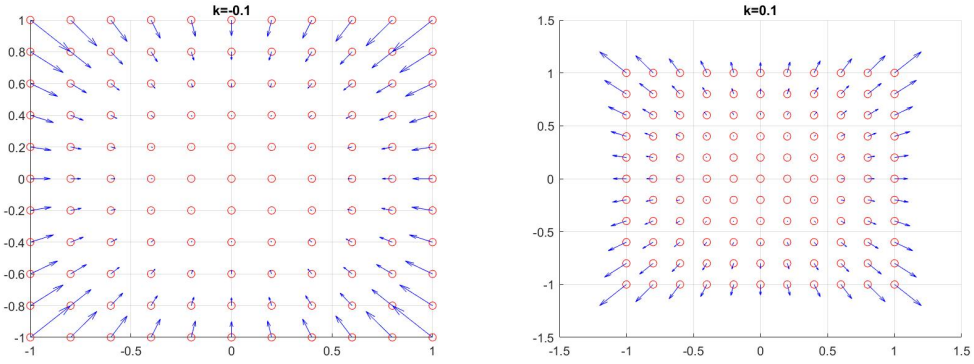

Fig. 4.4. Pincushion correction is shown on the left, and barrel correction is shown on the right [26].

These examples of distortion are exaggerated. High quality sensors will have radial distortion values of approximately 0.1 arcseconds of biased error. If the object of interest is not in the exact center of a telescope's field of view, the pixel position is introduced to more needed correction or calibration, which contributes to changes in uncertainty [18].

As stated before, in the case of information sharing between organizations, these uncertainties are usually not shared, and when they are shared, it is still good practice to assume that these uncertainties exist. Random variables can be inserted into Eq. 4.1 and Eq. 4.2. For example, general measurement error, Δ, for an observation angle can be modeled as mean random variable with zero mean following a normal distribution with a standard deviation of 1 arcsecond:

$$\Delta\alpha,\ \Delta\delta \sim N(0, 1^2)[arcseconds] \tag{4.8}$$

If the sensor has a known bias, β, such as radial distortion, the random variable can be shown as:

$$\Delta\alpha,\ \Delta\delta \sim N(\beta, 1^2)[arcseconds] \tag{4.9}$$

Measurement variance near 1-2 arcseconds can be found at state-of-the-art ground stations [18]. Amateur or lower-end equipment may have standard deviations around 10 arcsecond or higher. In Eq.4.8 and Eq. 4.9, the standard deviations can be adjusted to the appropriate level of uncertainty for individual users, who should consult their operations manuals.

4.1.3 Satellite Timing Error

Another uncertainty from limitations of the equipment is the observation timing error. When a ground station records angle measurements, the time of observation must also be recorded using time servers. This is typically achieved using local networks and GPS-precise timing. Again, the operations manual of the equipment specifies the uncertainty. For example, the Time Machines TM2000A, which is used at the

Purdue Optical Ground Station (POGS), records time with 3-σ bounds of 1 millisecond [27]. Then the satellite timing error, Δt of the observation can be recorded using a random variable with zero mean following a normal distribution with a standard deviation of 1/3 millisecond:

$$\Delta t_{POGS} \sim N(0, (.001/3)^2)[seconds] \tag{4.10}$$

According to the operations manual, the timing error follows a normal distribution, but because the two-body problem is nonlinear, the errors for the object's true position are not expected to follow a normal distribution after computing orbit determination or orbit propagation. The best time servers can have 3-σ bounds for error as low as 10 microseconds, and amateurs can expect greater than 10 milliseconds [13]:

$$\Delta t_{best} \sim N(0, (.000010/3)^2)[seconds] \tag{4.11}$$

$$\Delta t_{amateur} \sim N(0, (.010/3)^2)[seconds] \tag{4.12}$$

4.1.4 Ground Station Timing Error

When observations are recorded, the position of the ground station is also recorded with the local sidereal time. Similar to the satellite observation timing error, there is uncertainty associated with the time at the ground station's local sidereal time. The TM2000A operations manual specifies a 3-σ sidereal timing error of 10 microseconds. Then, the ground station timing error, $\Delta\theta$, can be expressed as a random variable with zero mean following a normal distribution with a standard deviation of 10/3 microsecond:

$$\Delta\theta_{POGS} \sim N(0, (.00001/3)^2)[seconds] \tag{4.13}$$

However, it is common practice to record sidereal time angularly as it is a measure of the Earth's rotation. Then the timing must be converted using the Earth's rotation rate, $\omega = 15^\circ/hr$. As with the satellite timing error, this normally distributed random variable experiences nonlinear transformations as orbit determination and propagation are performed, and the resultant uncertainties in the object's position are not

expected to follow a normal distribution. A low-quality time server with intermittent GPS synchronization, such as a cell phone, can experience standard deviations as high as a tenth of a second [13]:

$$\Delta\theta_{cellphone} \sim N(0, (.10/3)^2)[seconds] \tag{4.14}$$

Depending on the orbit region, both of the above timing errors have varying effects on an object's position uncertainty: the effect is proportional to the velocity of the object. Since objects in LEO are traveling at higher velocities, the position errors are greater than compared to a slower-moving object in GEO. Likewise, for elliptical orbits, depending on where the object is in relation to apogee or perigee.

4.1.5 Timing Bias

Due to some limitations in the equipment, it is possible to have a biased timing error. Users who are very familiar with their equipment may already know that their recordings have timing bias, β. In this case, Eq. 4.2 can be used but with the zero mean replaced with the known bias.

$$\Delta t \sim N(\beta, (.001/3)^2)[seconds] \tag{4.15}$$

Because time servers and processors are not instantaneous, some timing bias is not uncommon, but some time servers simply subtract the known bias from the recorded time [27]. If the equipment has any lag in its operation, the resultant image would be recorded later than expected. For example, the POGS telescope uses an electronic shutter, which records light in the pixel grid one row at a time. This results in a cascading, time-delayed capture of the light signals. The time-delay may take as long as a tenth of a second depending on the exposure settings and where in the pixel grid the signal is recorded. These kinds of biases must be considered when recording measurements, and they should be removed before any computations are made.

4.1.6 Time and Light Aberration

In addition to the limitations of the equipment at the ground station, another source of time bias results from the light signal from the object taking time to travel to the surface of the Earth. In that time, the object continues to move, and this phenomenon is known as light aberration, shown in Figure 4.3. How to compute light aberration can be found in section 6.2.2. of Montenbruck's *Satellite Orbits* [1]. The

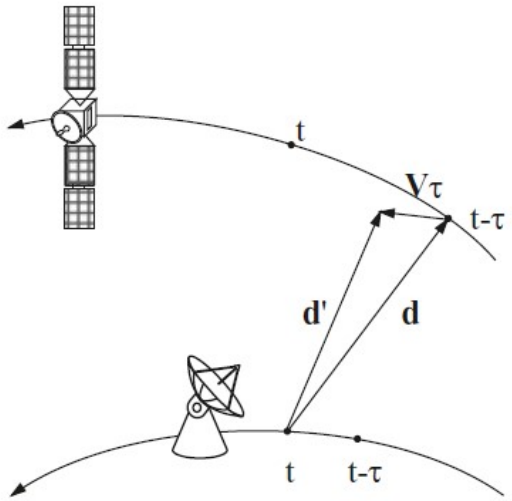

Fig. 4.5. The effect of aberration on a Near-Earth Object [1]

aberration effect on angle measurements is approximately 0.6 arcseconds for LEO objects and 0.3 arcseconds for GEO objects [1].

Stellar Aberration Correction

In order to account for the Earth's movement relative to distant bodies in the star catalogs, well-documented, empirical data is used to calculate aberration correction. This allows users to position the night sky accurately using a stellar background as a reference. However, star catalogs typically use yearly aberration corrections [18], which may not be the most appropriate for tracking a near-Earth object. In *Fundamentals of Astronomy*, Kovalevsky computes an example of stellar aberration to be approximately 20 arcseconds [26]. Using known variances from the star catalog [13], a random variable for the biased stellar aberration, ϕ, can be represented before correction:

$$\Delta\phi_{uncorrected} \sim N(20, 0.001^2) \ [arcseconds] \tag{4.16}$$

As Eq. 4.16 shows, uncorrected aberration has a much larger effect on distant objects than on near objects. When corrected, the random variable assumes zero mean and can be written as

$$\Delta\phi_{corrected} \sim N(0, 0.001^2) \ [arcseconds] \tag{4.17}$$

Though there is correction, there is still an uncertainty associated with every measurement. Unfortunately, in sharing information, this type of procedural information is not included, which further adds to observation uncertainties.

4.2 Refraction

A signal from space experiences refraction as it passes through the dense Earth atmosphere. Refraction is the bending of light that results from the slowing of light as it passes through denser mediums. The resultant passing angle follows Snell's Law (Eq. 4.2) [1], which relates the velocity of the signal v, the passing angle θ, and the refractive index n of the medium. Here, c is the speed of light, $3.0 \cdot 10^8$ m/s, and n

is the refractive index, which can be found with $n = c/v$. Figure 4.3 shows a simple example of how a light signal refracts as it passes through different mediums.

$$n_1 \sin\theta_1 = n_2 \sin\theta_2 \tag{4.18}$$

$$\frac{\sin\theta_1}{v_1} = \frac{\sin\theta_2}{v_2} \tag{4.19}$$

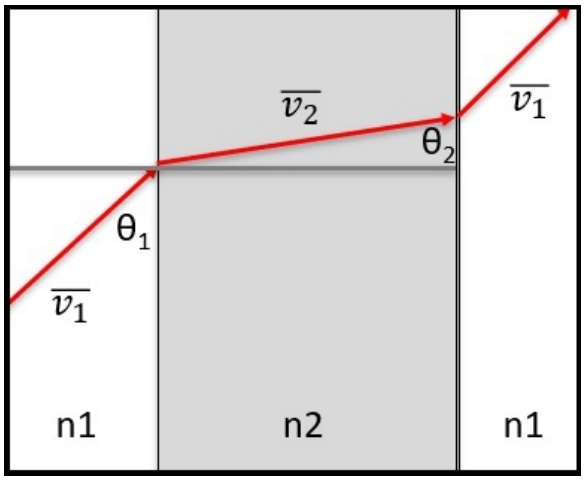

Fig. 4.6. Visual Example of Snell's Law and light passing through arbitrary mediums. For reference, $n_{vacuum} = 1.000$, $n_{air} = 1.000277$. [1]

For astrodynamic applications, refraction is measured as the difference between true elevation, h and observed elevation h', and the refractive index, R, is expressed as $R = h' - h$, which is shown visually in figure 4.5 below.

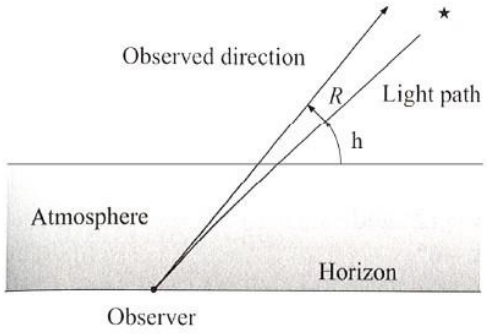

Fig. 4.7. Refraction of a light signal [18]

Computing atmospheric density using an analytic method is very difficult as the composition and distribution of the atmosphere is constantly changing. Montenbruck presents a simplified empirical formula for refraction in his *Satellite Orbits*:

$$R = \frac{p}{T}[3.430289(z' - \sin^{-1}(0.998647 \sin(0.996714z')) - 0.01115929z'], \qquad (4.20)$$

where z' is the observed zenith angle $(90^\circ - h')$. Eq. 4.12 only considers total pressure, p, and temperature, T, which limits the applicability. Instead, this thesis uses a refraction model which combines various empirically derived formulas using ambient temperature, dry air pressure, and water vapor pressure. This refraction model uses elements of Stone's paper on computing atmospheric refraction [28] as a reference. The formulation begins with an integral seen from Smart (1965) and Green (1985), which approximates refraction as a function of wavelength:

$$R(\lambda) = r_o n_o sinz_o \int_1^{n_o} \frac{dn}{n\sqrt{r^2n^2 - r_o^2 n_o^2 sin^2 z_o}} \qquad (4.21)$$

This model assumes a spherically symmetric model for the atmosphere and requires information from the observation site as well as an arbitrary point (for integrating),

such as geocentric distance r, air refractive index n, and observed zenith angle z. The air index is expressed using air densities according to the Gladstone-Dale Law [28]:

$$n = 1 + (n_o - 1)\frac{\rho}{\rho_o} \tag{4.22}$$

This is substituted into Eq. 4.6 and then expanded into a power series, of which the first two terms are used:

$$R(\lambda) = \gamma(1-\beta)\tan z_o - \gamma(\beta - \gamma/2)\tan {z_o}^3 + h.o.t. \tag{4.23}$$

where $\gamma = n_o - 1$, $\beta = \frac{H_o}{r_o}$, and k = 1 (spherically symmetric). H_o is defined as "the height of an equivalent homogeneous atmosphere" [28] and is expressed as the integral:

$$H_o = \frac{1}{\rho_o}\int_0^\infty \rho \, dh \tag{4.24}$$

With the spherical assumption, density can be expressed as $\rho = \rho_o \; e^{-h/h_o}$, which simplifies the β to

$$\beta = 0.001254(\frac{T}{273.15}) \tag{4.25}$$

At this point, the only remaining undertermined value is the air refractive index at the observation site. Ambient air temperature T, dry air pressure P_s, and water vapor pressure P_w are used for the computation below. These equation are derived using empirical approximations given by Owens (1967) [28]:

$$\begin{aligned}(n-1)10^8 = [2371.34 + \frac{683939.7}{(130-\sigma^2)} + \frac{4547.3}{(38.9-\sigma^2)}]D_s + ... \\ + (6487.31 + 58.058\sigma^2 - 0.71150\sigma^4 + 0.08851\sigma^6)D_w\end{aligned} \tag{4.26}$$

$$D_s = [1 + P_s(57.90x10^{-8} - \frac{9.3250x10^{-4}}{T} + \frac{0.25844}{T^2}]\frac{P_s}{T} \tag{4.27}$$

$$\begin{aligned}D_w = [1 + P_w(1 + 3.7x10^{-4}P_w)(-2.37321x10^{-3} + ... \\ + \frac{2.23366}{T} - \frac{710.792}{T^2} + \frac{7.75141x10^4}{T^3})]\frac{P_w}{T}\end{aligned} \tag{4.28}$$

The first step for this model is to select the desired wavelength to find the wave number, $\sigma = \frac{10^4}{\lambda}$. This thesis uses monochromatic light with a wavelength of $\lambda =$ 5000 Angstrom. Then the local atmosphere information is used to compute the D_s and D_w terms in Eq. 4.18 and Eq. 4.19.

Eq. 4.17 returns the air index of refraction. This air index approximates the air index of refraction at the ground station. For this application, refraction index is used

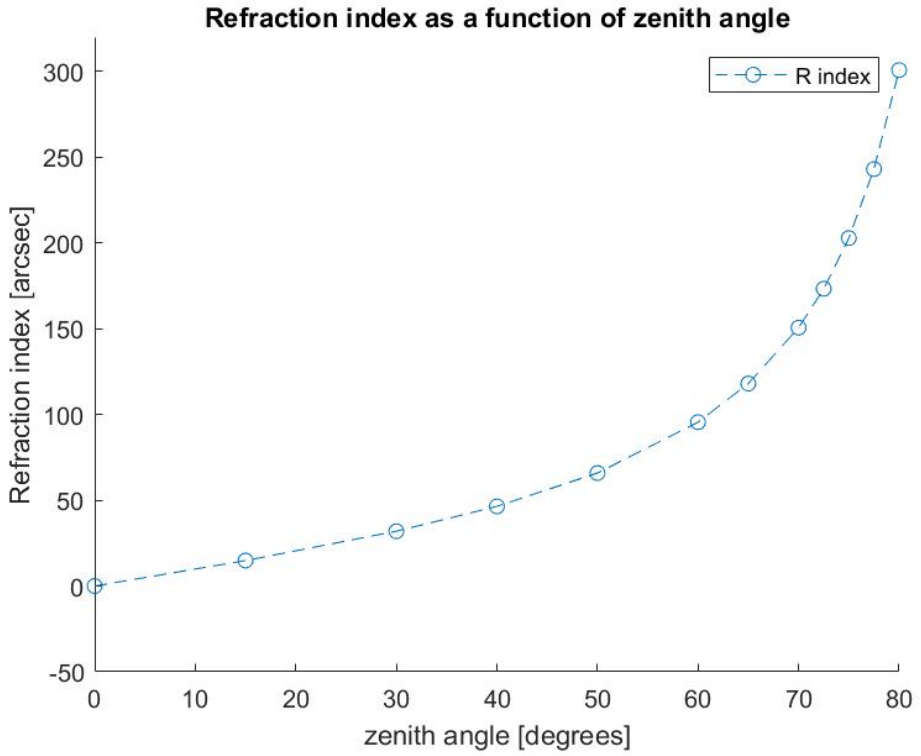

Fig. 4.8. Refraction Index as a function of Zenith Angle

as a function of zenith angle, pressures, and temperature. As seen in Fig. 4.7, The refraction index increases considerably with higher zenith angles. The model shows values of refraction index ranging from 0 to over 300 arcseconds, but this method for computing refraction is only recommended when zenith angles are less than 75 degrees. This is an acceptable restriction since in practice, observations are not taken with such high zenith angles in an effort to minimize atmospheric effects [28].

Preferred measurements occur under 50 degrees zenith, where the refraction index curve is mostly linearly. This refraction model allows for users to input local ambient temperature and pressures without having to reference cumbersome tabulated information.

5. DISTRIBUTION TESTING AND RESULTS

In this chapter, orbit simulations are made in four different orbit regions: GEO, HEO, MEO, and LEO. For each orbit region, one satellite is first propagated for one full orbital period to capture the truth orbit. Truth information for all objects in this chapter are obtained from the space-track.org TLE catalog from 01 September 2019. Propagation is done using the two-body equations of motion (Eq. 2.2) outlined in section 2.1. Second, perfect, error-free optical observations are simulated during a window of 50 minutes with measurements taken every 60 seconds for a total of 51 observations. However, for the LEO scenario, the observation window is reduced to 5 minutes with measurements taken every 6 seconds in order to account for the much short orbital periods in LEO. The simulated observer location is at Purdue University in West Lafayette, Indiana at 0 meters altitude. Each observation contains both topocentric right ascension and declination angle measurements using the topocentric equatorial coordinate system from section 2.2.4. The Gauss IOD method from section 2.4.1 is completed using the first, middle, and last observations, and the IOD solution is improved with all 51 observations using the least squares method from section 2.4.2. The least squares solution is then compared to the original truth orbit in RSW reference frame from section 2.2.6 using the truth as the reference. These differences are the baseline for orbital errors generated solely from the orbit determination process.

In order to study the varying effects of the errors modeled in chapter 4, they are applied in this chapter to the different orbit regions. For each orbital region, the same base scenario is simulated but with the inclusion of a modeled error. After orbit determination, the angle measurements are extracted from the least squares estimate for the same 50-minute observation window. The least squares angles are then compared to the simulated observation angles. The differences in these angles are then used to compile the angle error samples. This angle error samples in both right as-

cension and declination are tested for normality using the Shapiro-Wilk distribution test discussed in section 3.2.2. The distribution test results reveal the usability and validity of the dataset used for orbit determination. The least squares solution is used in the steps leading to the distribution testing in order to simulate a real-world situation where the truth orbit is not known for a newly detected object. The resulting least squares solution is compared to the truth orbit, and the orbital errors are captured in the RSW frame using the original truth orbit as reference. The RSW errors are compared to the baseline RSW errors. These comparisons to the baseline errors serve to capture the impact and magnitude of the errors in question. For each scenario, unless otherwise stated, only one type of error is modeled in order to isolate and capture its sole effect on the particular orbit. The procedure for modeling the error and testing the error distribution are described in detail for the first scenario. All other scenarios follow the same procedure unless otherwise stated.

5.1 Geosynchronous Orbit: INTELSAT 902

The geosynchronous communications satellite, INTELSAT 902 is propagated to a full orbit using two-body motion, which is shown in Fig. 5.1. This orbit has a semi-major axis of 42,165 km, an eccentricity of 0.0003, an inclination of 0.0075°, a RAAN of 158.1469°, an argument of perigee of 1.7019°, and a true anomaly of 62.5649°. Orbital Elements are extracted from the state at the beginning of the observation window. For reference the true, error-free angle measurements for the 50-minute observation window are shown in Fig. 5.1 in degrees. Both angle measurements increase at a nearly linear fashion due to the geosynchronous and circular characteristics of the orbit. The black X's in Fig. 5.1 indicate from where in the orbit the observation are extracted. The method of introducing errors in the GEO scenarios are repeated for the scenarios in each orbital region.

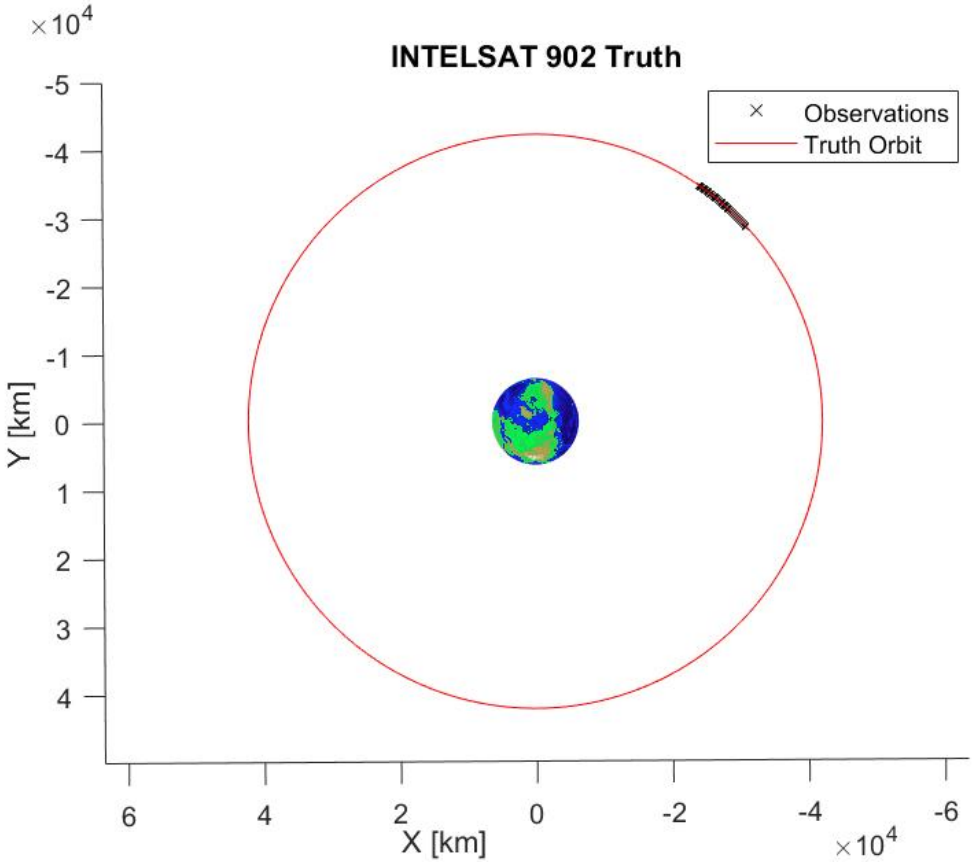

Fig. 5.1. INTELSAT 902: Full truth orbit

With perfect measurements, the least squares method has maximum errors value of 7.1 mm in the radial direction, 34.9 mm in the along-track direction, and 0.3 mm in the cross-track direction. This is in agreement with a error-free scenario serves as a baseline in GEO strictly from the least squares method. Fig. 5.3 shows the trends for these errors over the whole orbit. It can be seen that both the radial and cross-track components experience periodic errors due to the circular nature of the orbit. This is expected because the least squares solution estimates an initial state for the orbit and is most accurate at the initial time used in the orbit determination. The orbital errors in general are largest when far from the initial state estimate. However, in the along-track component, the NLUMVE orbit falls increasingly behind the truth and

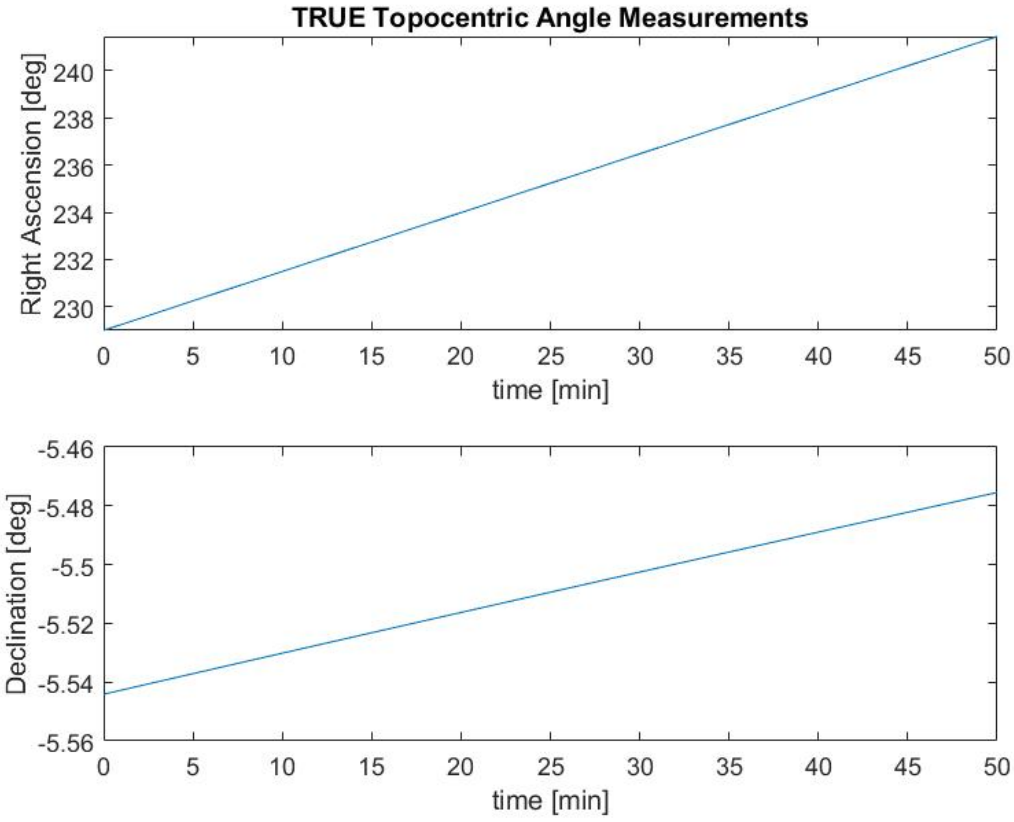

Fig. 5.2. INTELSAT 902: True, error-free angle measurements

does not improve after one period. If the starting position of an orbit is incorrect, then the along-track error component can only increase over many revolutions. This stresses the importance of frequently updating object tracking with new observation. As various levels of timing and measurement errors from chapter 4 are introduced into the scenario, these orbital error values are expected to increase.

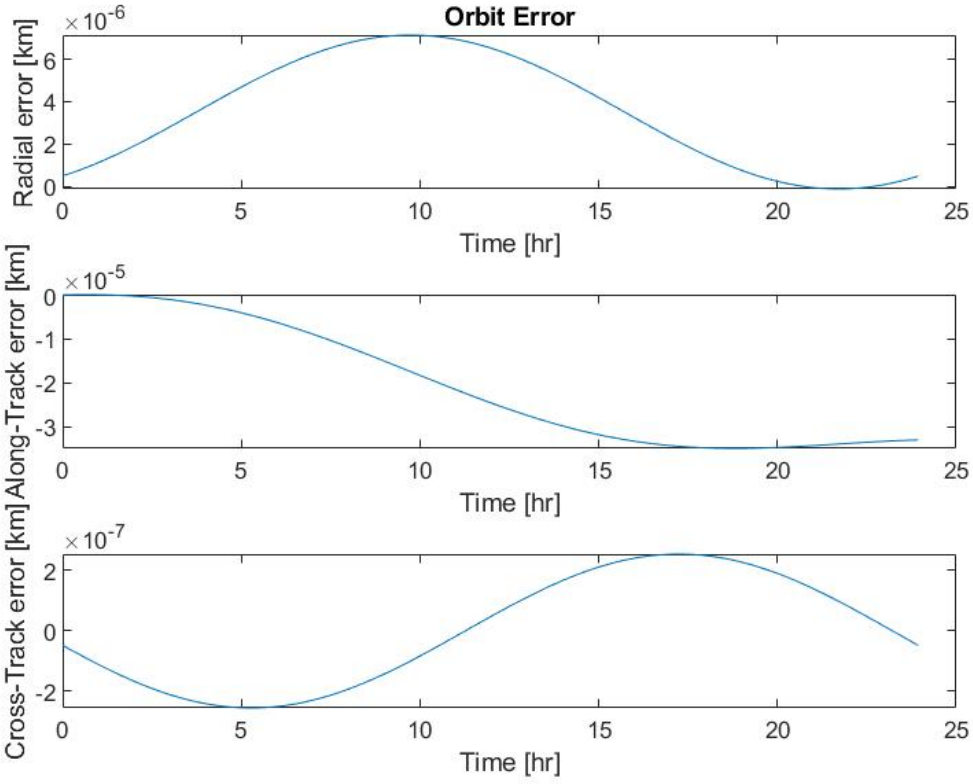

Fig. 5.3. INTELSAT 902: RSW orbital errors, NLUMVE vs truth with no modeled errors

5.1.1 GEO Timing Error

Timing error is introduced in the GEO scenario in order to demonstrate the impact of poor timing in relation to optical measurements as outlined in section 4.1.3 on satellite timing error. The GEO scenario is run using a range of values for the $3\sigma_t$ timing error, 0.001 s to 1.000 s.

$$\Delta t_{error} \sim N(0, \sigma_t^2)[seconds] \tag{5.1}$$

The simulated observations angles have errors computed using the timing error random variable. The erroneous measurements are then compared to the angles extracted

from the least squares estimated orbit solution. The result is an error distribution that contains information about how the simulated observations deviate from the measurements extracted from the least squares estimate.

In Fig. 5.4, it can be seen that the error distribution for the declination measurements is experiencing a nonlinear transformation, which is detected by the Shapiro-Wilk Test. Although the declination errors are small at less than 1 arcsecond for the largest timing error, the tests are still able to indicate that the measurements are not following a normal distribution and would be able to notify users in a GEO scenario that observations may contain errors. The RSW errors in Fig. 5.5 are computed using the least squares estimate orbit propagated to one full orbit compared with the full truth orbit. Table 5.1 displays the Shapiro-Wilk test results. Both test statistic and p-values are shown for both right ascension and declination error distributions. Also displayed are the maximum errors in each of the RSW components.

Increasing the timing error inflates any orbital errors that existed in the base scenario. The right ascension error distribution has relatively large errors for the scenario with largest timing error with some errors exceeding 10 arcseconds, but the distribution does not indicate any violations in normality or unequal variance as seen in Table 5.1. It is important to note however, that the test only identifies if a data set has an unusual distribution. The Shapiro-Wilk Test, or any statistical distribution test, only provides information about the error distribution itself Table 5.1 shows that 3 of 4 of the GEO timing error scenario would test positive for the Shapiro-Wilk test at a significance value of 0.05, but the p-value here does not necessarily correlate to higher or lower orbital errors. This method still requires an orbital analyst to determine the problem in the dataset.

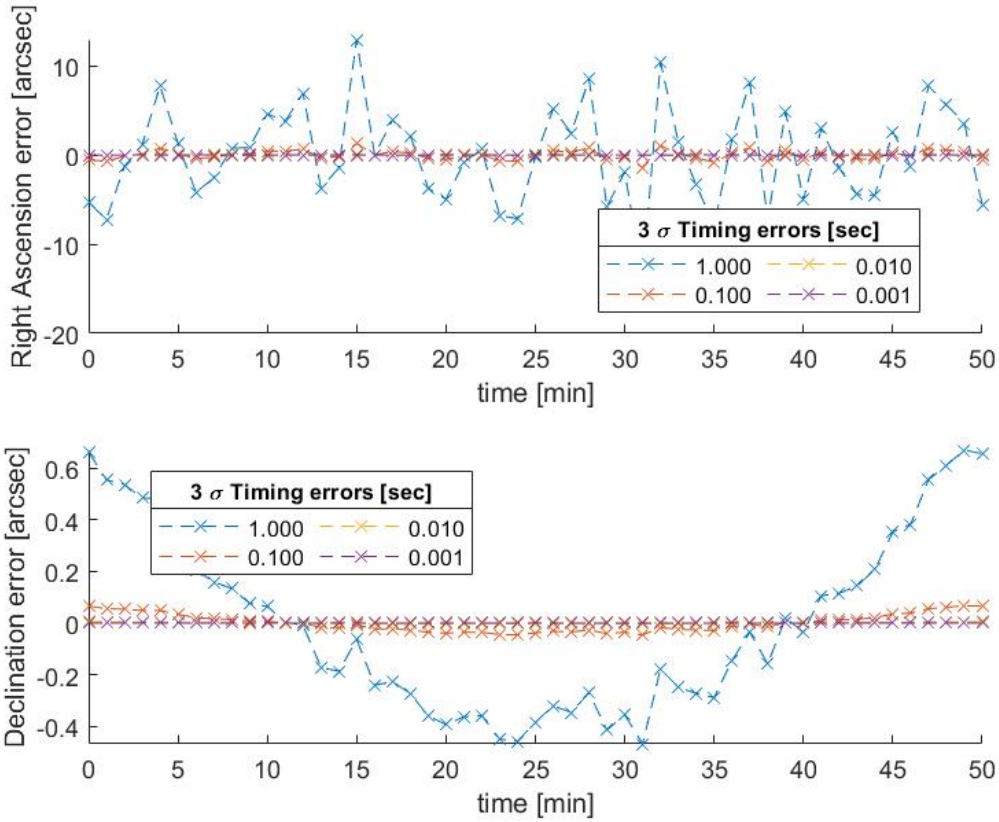

Fig. 5.4. INTELSAT 902: Observation vs NLUMVE angle error distributions for unbiased timing error

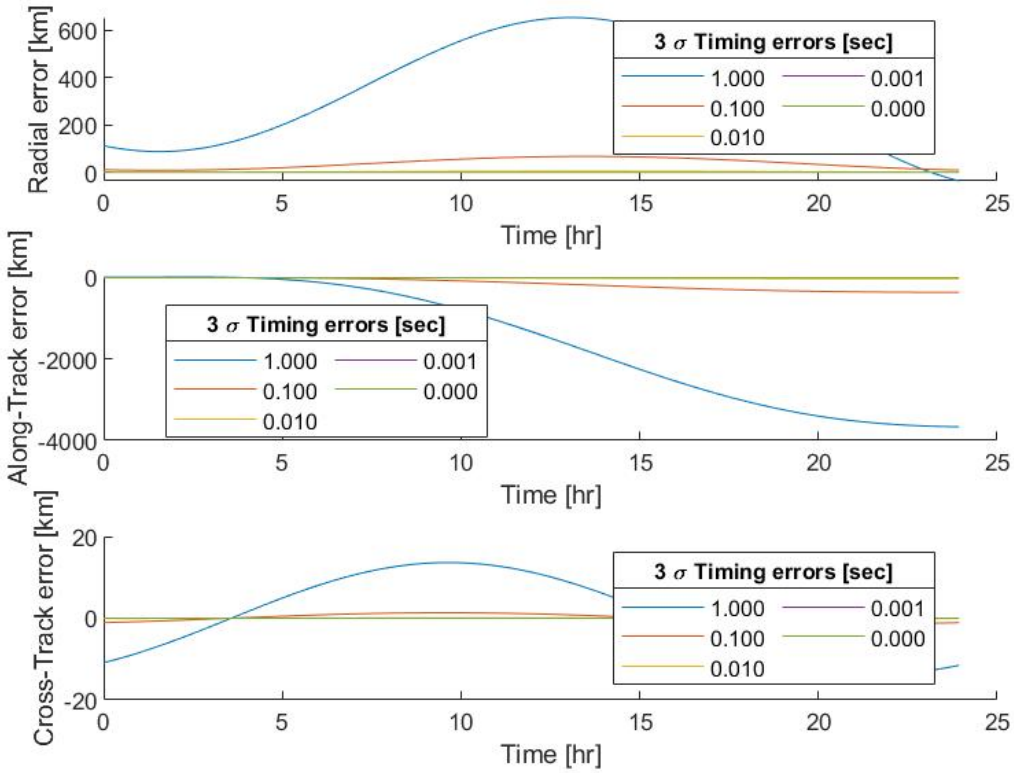

Fig. 5.5. INTELSAT 902: RSW orbital errors, NLUMVE with modeled unbiased timing error vs truth

Table 5.1.
INTELSAT 902: Shapiro-Wilk test results with RSW orbital errors for unbiased timing error scenarios

INTELSAT 902	**Measurements vs. NLUMVE angles SW test**				**NLUMVE vs. Truth Orbit** (max errors)		
3σ Timing Error	W α	α P-val	W δ	δ P-val	Radial Error	Along-Track Error	Cross-Track Error
0.000 s	NaN	NaN	NaN	NaN	0.0071 m	0.0349 m	0.0003 m
0.001 s	0.9668	0.1618	0.9650	0.1357	64.992 m	280.10 m	4.2099 m
0.010 s	0.9871	0.8482	0.8814	1.0635E-04	5,042.0 m	27,049 m	91.036 m
0.100 s	0.9893	0.9243	0.9191	0.0020	67,560 m	359,810 m	1,344.2 m
1.000 s	0.9676	0.1754	0.9094	8.8102E-04	214,790 m	1,139,300 m	5,154.9 m

5.1.2 GEO Timing Bias

Timing bias is introduced in the GEO scenario in order to demonstrate the impact of poor timing in relation to optical measurements. The GEO scenario is run using a range of values for the β_t timing bias, 0.001 s to 1.000 s, and a small 3σ timing error of 0.001 s.

$$\Delta t_{error} \sim N(\beta_t, (.001/3)^2)[seconds] \tag{5.2}$$

It can be seen in Fig. 5.6 that the error distribution for the declination measurements is still experiencing a nonlinear transformations detected by the Shapiro-Wilk Test, and right ascension measurement errors appear random. Fig. 5.7 and Table 5.2 show that for the first case, the primary source of error is from the small 3σ timing error, not the bias, but as the bias increases, the orbital errors increase as well. However, the increases occur more linearly, hinting that fixed timing bias does not cause a change in the distribution of the error. It only shifts it in relation to time. As seen in Table 5.2, the test results for the Shapiro-Wilk test do not change compared to the scenarios in Table 5.1.

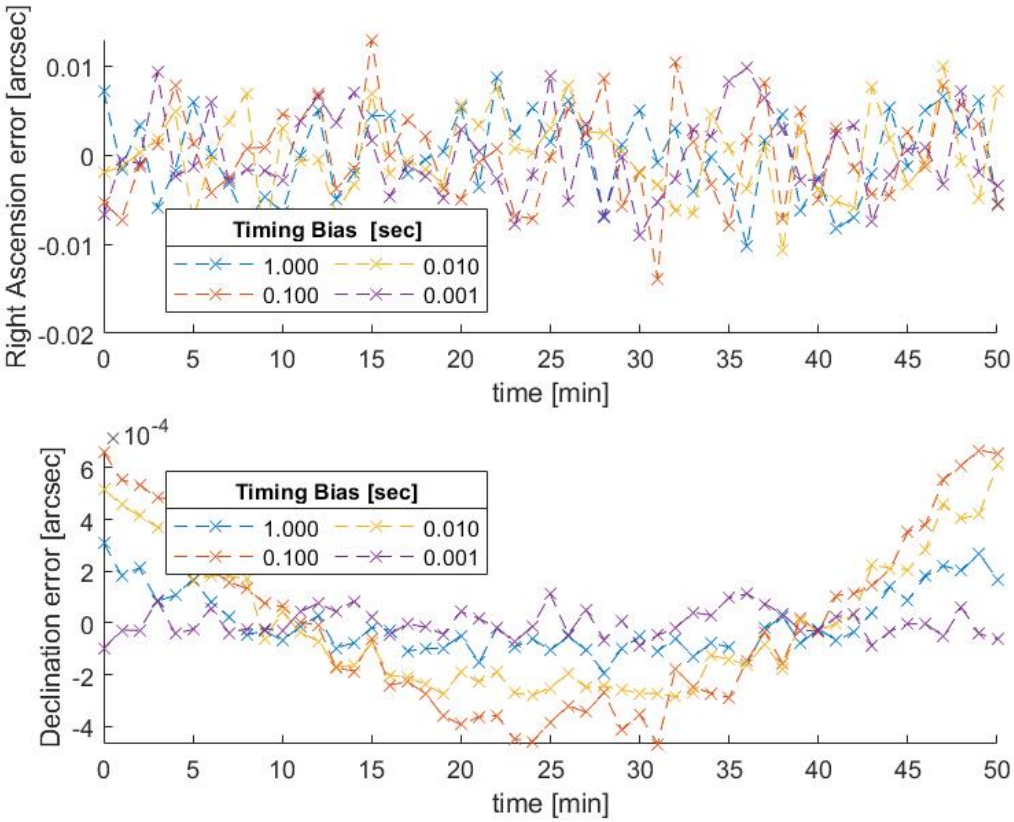

Fig. 5.6. INTELSAT 902: Observation vs NLUMVE angle error distributions for biased timing error

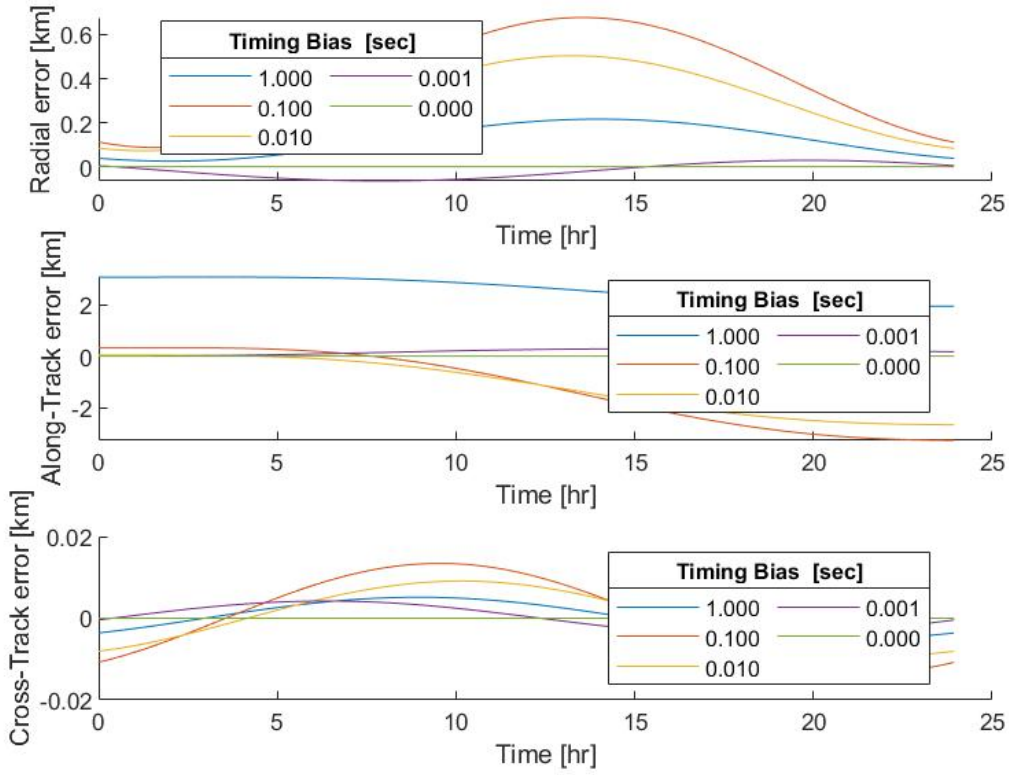

Fig. 5.7. INTELSAT 902: RSW orbital errors, NLUMVE with modeled biased timing error vs truth

Table 5.2.
INTELSAT 902: Shapiro-Wilk test results with RSW orbital errors for biased timing error scenarios

INTELSAT 902	Measurements vs. NLUMVE angles SW test				NLUMVE vs. Truth Orbit (max errors)		
Timing Bias	W α	α P-val	W δ	δ P-val	Radial Error	Along-Track Error	Cross-Track Error
0.000 s	NaN	NaN	NaN	NaN	64.992 m	280.10 m	4.2099 m
0.001 s	0.9668	0.1618	0.9650	0.1357	64.992 m	283.18 m	4.2099 m
0.010 s	0.9871	0.8482	0.8814	1.0635E-04	504.33 m	2,673.7 m	9.1024 m
0.100 s	0.9893	0.9243	0.9191	0.0020	678.02 m	3,282.9 m	13.422 m
1.000 s	0.9676	0.1754	0.9094	8.8102E-04	215.99 m	3,083.4 m	5.1334 m

5.1.3 GEO Sidereal Timing Error

Sidereal timing error is introduced in the GEO scenario in order to demonstrate the impact of poor ground station timing as outlined in section 4.1.4. This simulates ground station location uncertainty as a result of poor timing. The GEO scenario is run using a range of values for the $3\sigma_t$ sidereal timing error, 0.001 s to 1.000 s:

$$\Delta t_{error} \sim N(0, \sigma_t^2)[seconds] \tag{5.3}$$

In Fig. 5.8, the angle error distributions seem random, but in Table 5.3, the distribution testing reveals relatively low p-values under 0.15 despite the declination errors being smaller, less than 0.2 arcsecond. The RSW errors in Fig. 5.9 show larger error values when compared to the truth orbit and emphasize the importance of minimizing Ground station uncertainties when performing orbit determination. The trends for RSW errors over the orbit period are also different. Some of the errors and peaks of the curves have shifted as a result of the sidereal timing error.

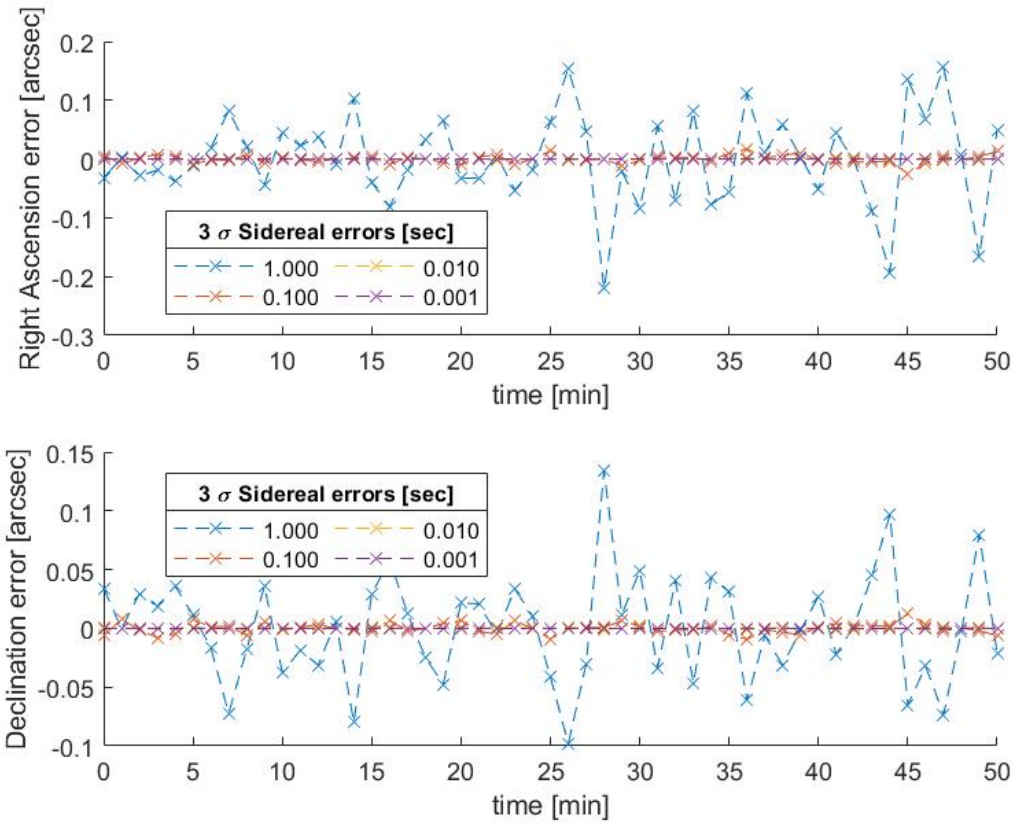

Fig. 5.8. INTELSAT 902: Observation vs NLUMVE angle error distributions for unbiased sidereal timing error

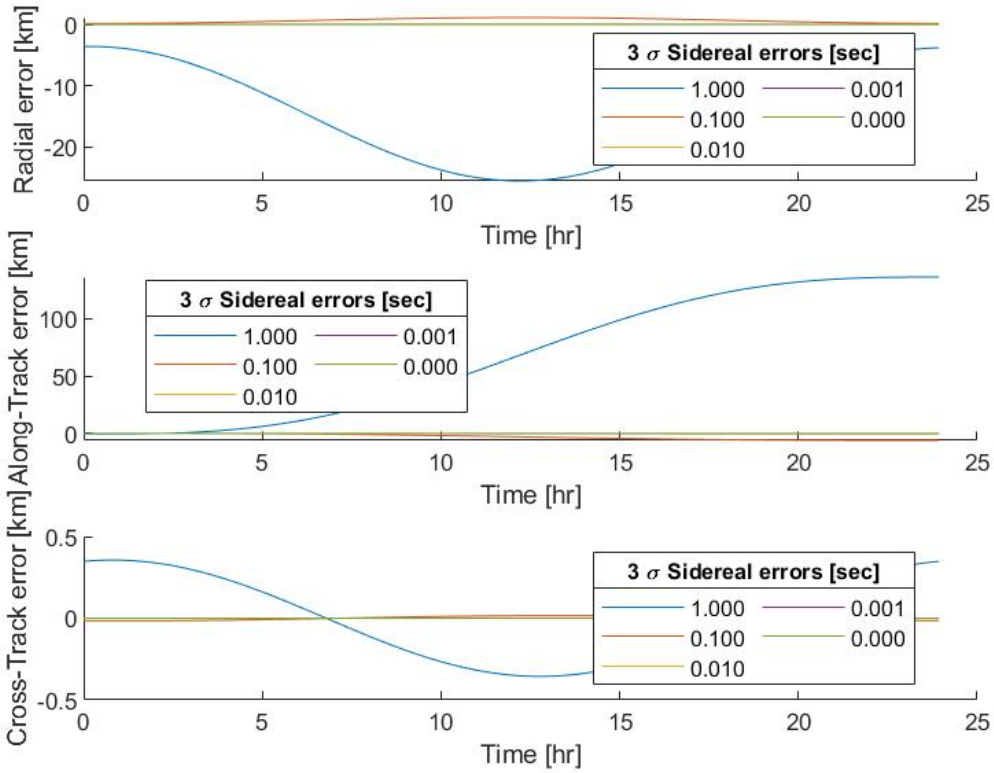

Fig. 5.9. INTELSAT 902: RSW orbital errors, NLUMVE with modeled unbiased sidereal timing error vs truth

Table 5.3.
INTELSAT 902: Shapiro-Wilk test results with RSW orbital errors for unbiased sidereal timing error scenarios

INTELSAT 902	Measurements vs. NLUMVE angles SW test				NLUMVE vs. Truth Orbit (max errors)		
3σ Sidereal Error	W α	α P-val	W δ	δ P-val	Radial Error	Along-Track Error	Cross-Track Error
0.000 s	NaN	NaN	NaN	NaN	0.0071 m	0.0349 m	0.0003 m
0.001 s	0.9803	0.5535	0.9673	0.1705	20.195 m	108.17 m	0.2822 m
0.010 s	0.9796	0.5203	0.9628	0.1101	74.285 m	396.79 m	1.0609 m
0.100 s	0.9641	0.1118	0.9859	0.8015	1,136.7 m	6,084.4 m	16.003 m
1.000 s	0.9659	0.1324	0.9805	0.4769	25,492 m	136,240 m	356.06 m

5.1.4 GEO Sidereal Timing Bias

Sidereal timing bias is introduced in the GEO scenario in order to demonstrate the impact of poorly calibrated equipment relation to ground station measurements. The GEO scenario is run using a range of values for the β_t timing bias, 0.001 s to 1.000 s, and a small 3σ timing error of 0.001 s.

$$\Delta t_{error} \sim N(\beta_t, (.001/3)^2)[seconds] \tag{5.4}$$

It can be seen in Fig. 5.10 that the angle error distributions seem random again, and Fig. 5.11 and Table 5.4 show that for the first case, the primary source of error is from the small 3σ timing error, not the bias. As expected, increasing the bias exaggerates the error trends and shifts the initial state more. The increases seem to occur more linearly, hinting that fixed timing bias does not cause a change in the distribution of the error. It only shifts it in relation to time. As seen in Table 5.4, the test results for the Shapiro-Wilk test do not change compared to the scenarios in Table 5.3.

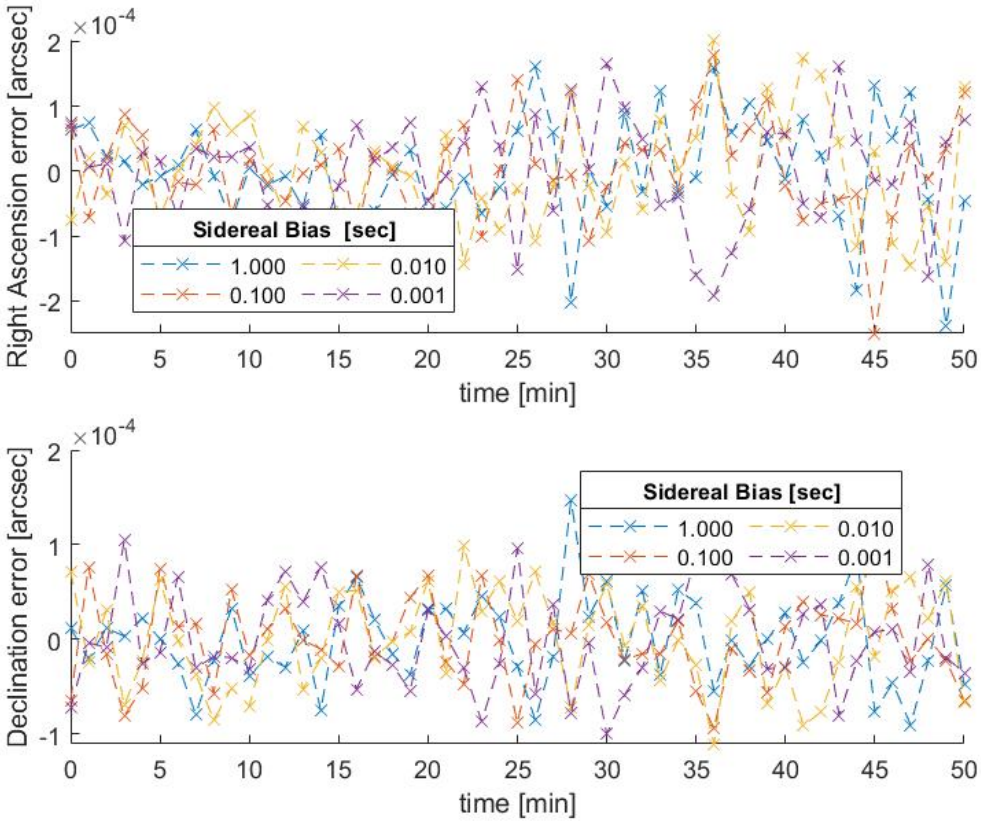

Fig. 5.10. INTELSAT 902: Observation vs NLUMVE angle error distributions for biased sidereal timing error

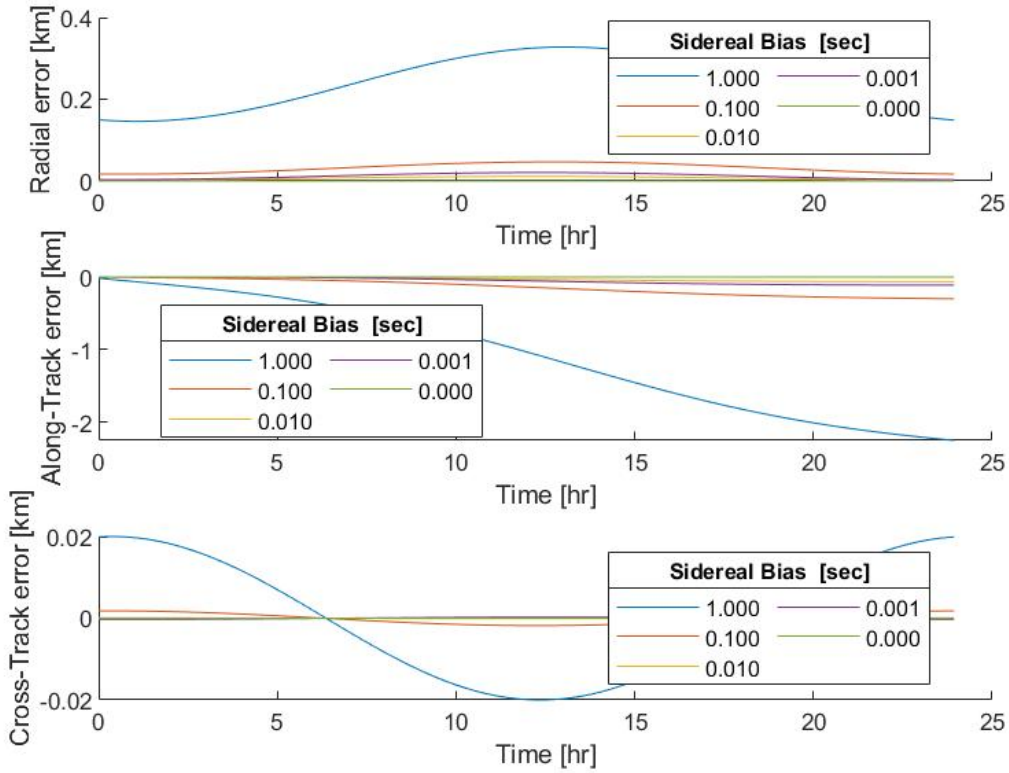

Fig. 5.11. INTELSAT 902: RSW orbital errors, NLUMVE with modeled biased sidereal timing error vs truth

Table 5.4.
INTELSAT 902: Shapiro-Wilk test results with RSW orbital errors for biased sidereal timing error scenarios

INTELSAT 902	**Measurements vs. NLUMVE angles SW test**				**NLUMVE vs. Truth Orbit** (max errors)		
Sidereal Bias	W α	α P-val	W δ	δ P-val	Radial Error	Along-Track Error	Cross-Track Error
0.000 s	NaN	NaN	NaN	NaN	20.195 m	108.17 m	0.2822 m
0.001 s	0.9803	0.5537	0.9673	0.1703	20.546 m	110.56 m	0.2627 m
0.010 s	0.9797	0.5241	0.9627	0.1083	10.938 m	63.533 m	0.0997 m
0.100 s	0.9639	0.1104	0.9849	0.7584	46.627 m	299.21 m	1.8091 m
1.000 s	0.9652	0.1243	0.9728	0.2450	327.79 m	2,247.0 m	20.003 m

5.1.5 GEO Angle Measurement Error

Angle Measurement error is introduced in the GEO scenario in order to demonstrate the impact of poor ground station timing as outlined in section 4.1.1. This can simulate an unbiased pixel position uncertainty. The GEO scenario is run using a range of values for the $3\sigma_{ang}$ angle measurement error, 0.1 arcseconds to 100.0 arcsecs for both right ascension and declination:

$$\Delta ang_{error} \sim N(0, \sigma_{ang}^2)[arcseconds] \tag{5.5}$$

In Fig. 5.12, the angle error distributions show normally distributed errors, which is expected since the inclusion of measurement error does not occur before any transformation through the two-body problem. The results in Table 5.5 confirms that for most of the data sets, there are no unusual patterns in the error distributions. Only the 1.0 arcsec case tests positive for the right ascension observations. The RSW errors in Fig. 5.13 show the largest error values thus far when compared to the truth orbit and suggest that it is most important that angle errors be minimized when performing orbit determination. Here, it is not recommended that distribution testing be used for detecting unbiased measurement error.

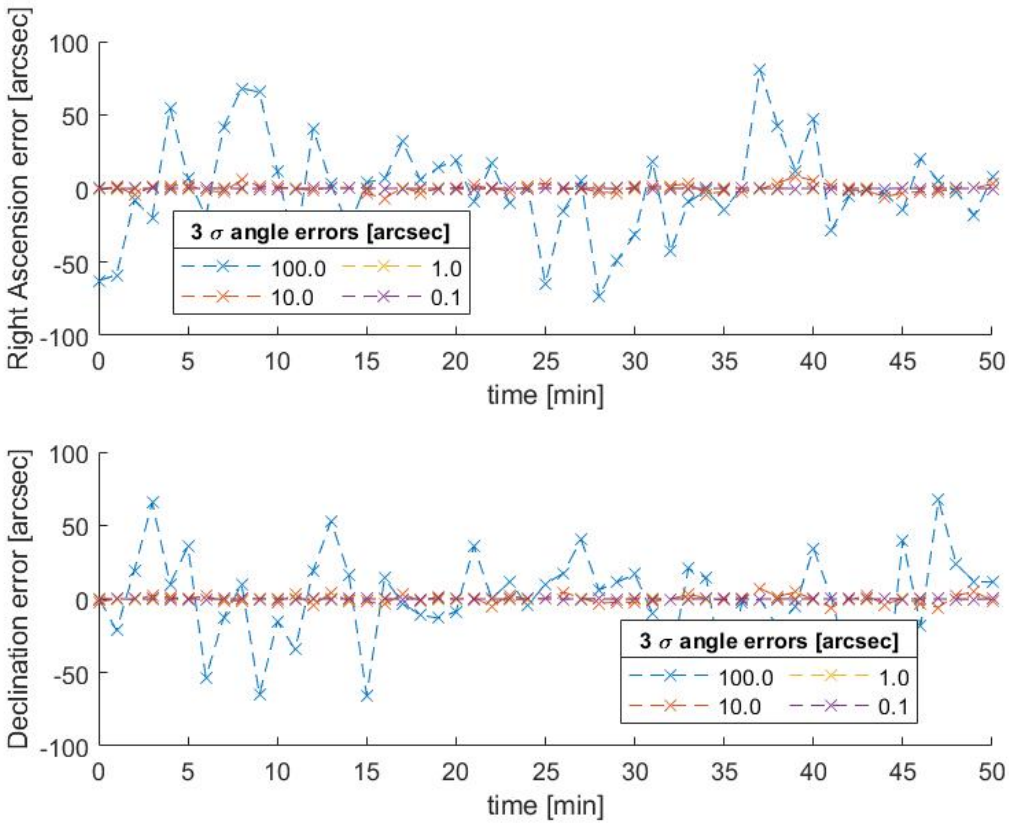

Fig. 5.12. INTELSAT 902: Observation vs NLUMVE angle error distributions for unbiased angle measurement error

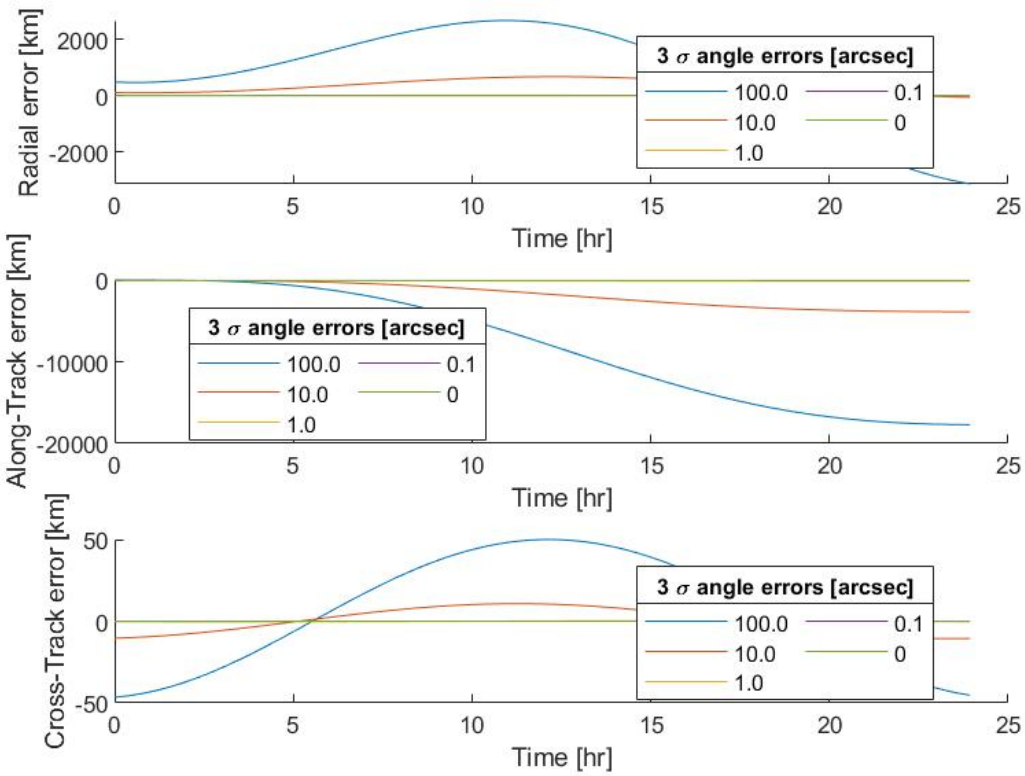

Fig. 5.13. INTELSAT 902: RSW orbital errors, NLUMVE with modeled unbiased angle measurement error vs truth

Table 5.5.
INTELSAT 902: Shapiro-Wilk test results with RSW orbital errors for unbiased angle measurement error scenarios

INTELSAT 902	Measurements vs. NLUMVE angles SW test				NLUMVE vs. Truth Orbit (max errors)		
3σ Angle Error	W α	α P-val	W δ	δ P-val	Radial Error	Along-Track Error	Cross-Track Error
0 arcsec	NaN	NaN	NaN	NaN	0.0071 m	0.0349 m	0.0003 m
0.1 arcsec	0.9860	0.8063	0.9702	0.2253	3,182.3 m	17,031 m	43.684 m
1.0 arcsec	0.9387	0.0109	0.9739	0.3185	13,922 m	70,094 m	298.95 m
10.0 arcsec	0.9782	0.3935	0.9912	0.9680	674,700 m	3,836,400 m	10,772 m
100.0 arcsec	0.9775	0.3709	0.9685	0.1911	3,144,600 m	17,703,000 m	50,062 m

5.1.6 GEO Angle Measurement Bias

Angle measurement bias is introduced in the GEO scenario in order to demonstrate the impact of poorly calibrated equipment relation to optical measurements. This can simulate the errors mentioned in section 4.1.2 on lens distortion. This GEO scenario is run using a range of values for the β_{ang} angle bias, 0.1 arcsecs to 100.0 arcsecs, and a small 3σ angle error of 0.1 arcsecs.

$$\Delta ang_{error} \sim N(\beta_{ang}, (.001/3)^2)[arcseconds] \tag{5.6}$$

It can be seen in Fig. 5.14 that the angle error distributions appear random for all scenarios. Fig. 5.15 and Table 5.6 show again that the distribution testing does not effectively detect angle measurement error. Since the bias does not affect the distribution shape itself, the results are largely similar to the unbiased angle error case. The results indicate that it is not recommended that distribution tests be used for detecting biased angle measurement error.

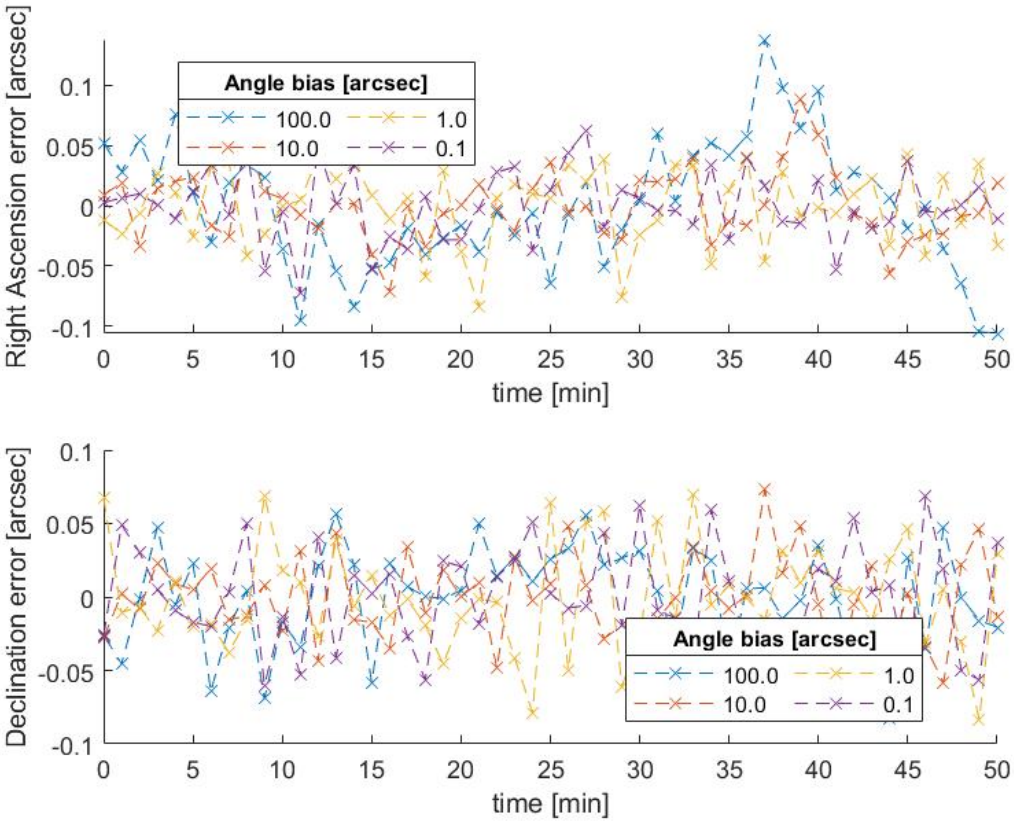

Fig. 5.14. INTELSAT 902: Observation vs NLUMVE angle error distributions for biased angle measurement error

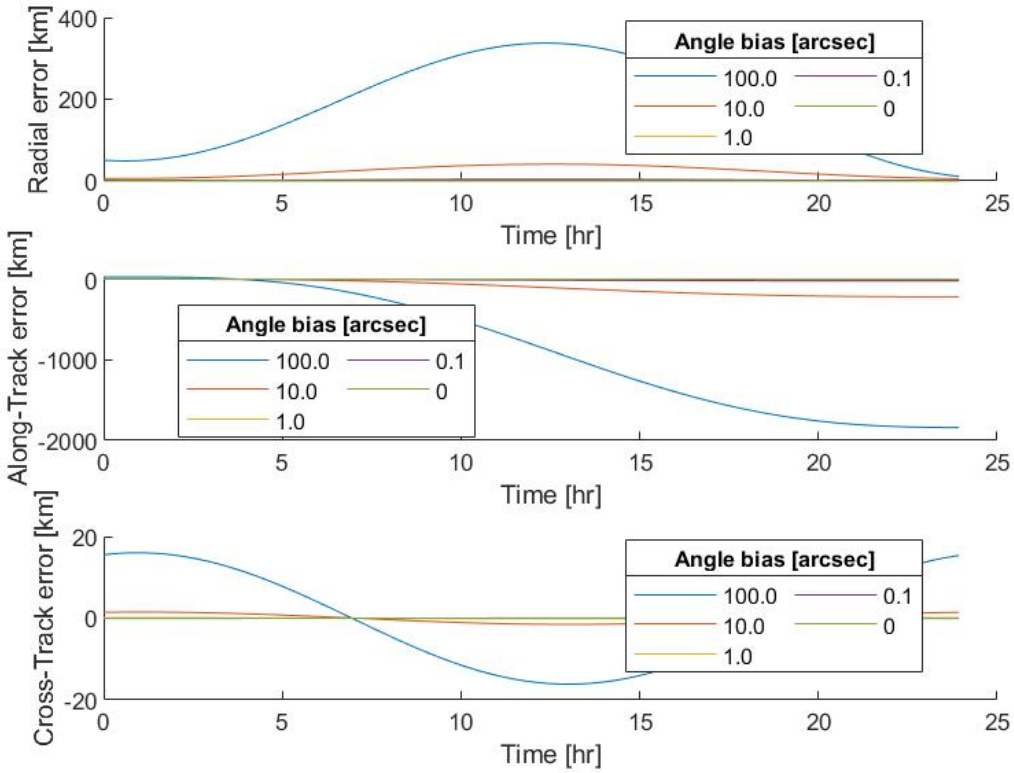

Fig. 5.15. INTELSAT 902: RSW orbital errors, NLUMVE with modeled biased angle measurement error vs truth

Table 5.6.
INTELSAT 902: Shapiro-Wilk test results with RSW orbital errors for biased angle measurement error scenarios

INTELSAT 902	**Measurements vs. NLUMVE angles SW test**				**NLUMVE vs. Truth Orbit** (max errors)		
Angle Bias	W α	α P-val	W δ	δ P-val	Radial Error	Along-Track Error	Cross-Track Error
0 arcsec	NaN	NaN	NaN	NaN	3,182.3 m	17,031 m	43.684 m
0.1 arcsec	0.9861	0.8081	0.9702	0.2255	3,532.0 m	18,838 m	27.679 m
1.0 arcsec	0.9384	0.0106	0.9741	0.3253	4,719.6 m	24,898 m	141.41 m
10.0 arcsec	0.9723	0.2356	0.9913	0.9692	41,023 m	218,620 m	1,513.9 m
100.0 arcsec	0.9915	0.9723	0.9656	0.1446	337,410 m	1,840,300 m	16,142 m

5.2 Highly Elliptical Orbit: MOLNIYA 3-24

For the HEO scenario, the Russian communications satellite, MOLNIYA 3-24 is used. Its full orbit and the observations used are shown in Fig. 5.16 and has a semi-major axis of 22,592 km, an eccentricity of 0.6463, an inclination of 63.9277°, a RAAN of 250.7600°, an argument of perigee of 254.9454°, and a true anomaly of 181.9454°. Orbital Elements are extracted from the state at the beginning of the observation window. For reference, Fig. 5.17 shows right ascension increasing in a near linear fashion and declination increasing at a slowing rate as it approaches apogee in its elliptical orbit in the 50-minute observation window.

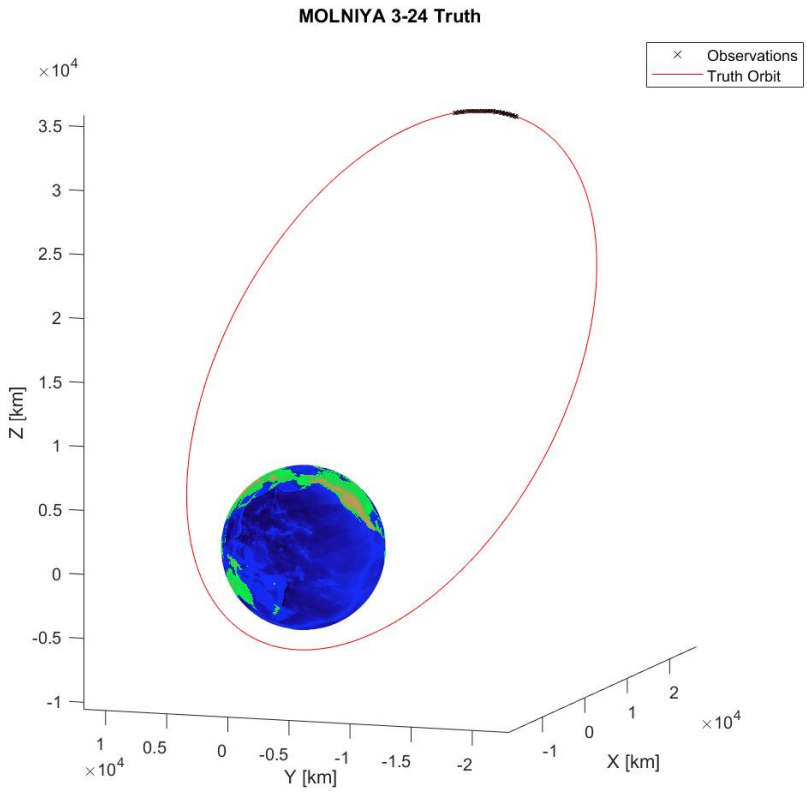

Fig. 5.16. MOLNIYA 3-24: Full truth orbit

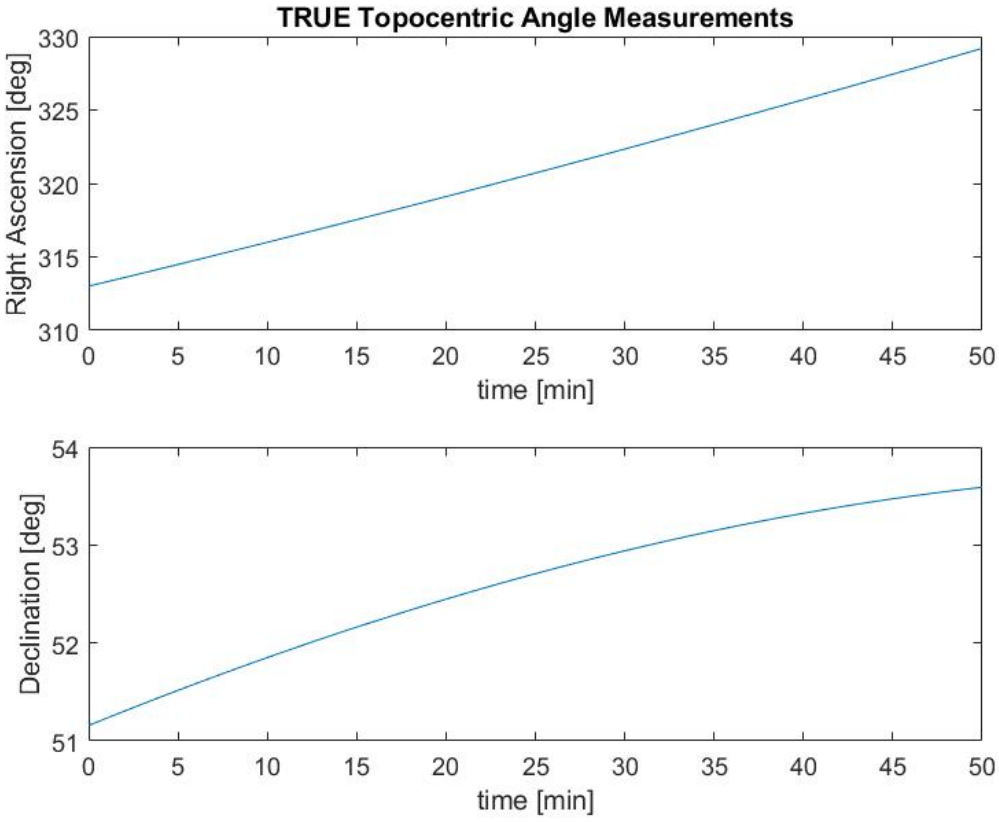

Fig. 5.17. MOLNIYA 3-24: True, error-free angle measurements

Fig. 5.18 shows the RSW orbital errors with the truth as reference. With perfect measurements, the least squares method has maximum errors value of 4.8 mm in the radial direction, 12.6 mm in the along-track direction, and 0.4 mm in the cross-track direction. These values are lower than the errors from the GEO scenario, which is expected, since the magnitude of velocity of MOLNIYA 3-24 at apogee is approximately 1.9528 km/s, and INTELSAT 902 travels at approximately 3.0751 km/s. These errors values serve as a baseline level for RSW errors for this HEO satellite strictly from the least squares method. As errors from chapter 4 are introduced into the scenario, these error values are expected to increase.

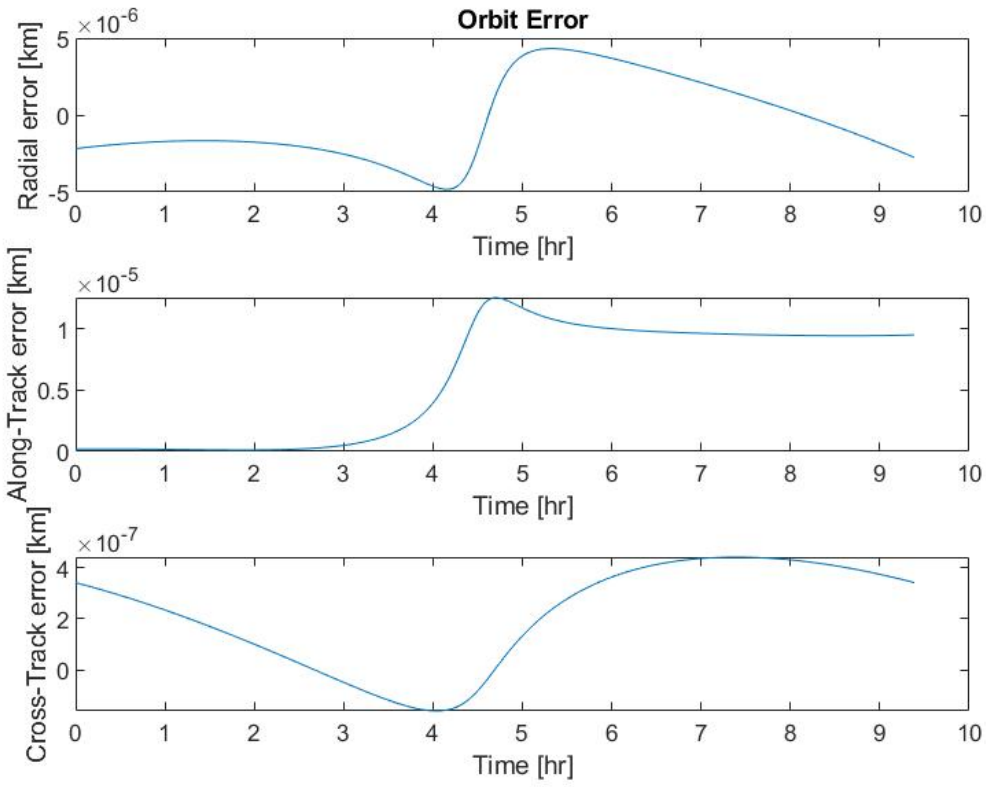

Fig. 5.18. MOLNIYA 3-24: RSW orbital errors, NLUMVE vs truth with no modeled errors

5.2.1 HEO Timing Error

Timing error is introduced in the HEO scenario in order to demonstrate the impact of poor timing in relation to optical measurements. The HEO scenario is run using a range of values for the $3\sigma_t$ timing error, 0.001 s to 1.000 s.

$$\Delta t_{error} \sim N(0, \sigma_t^2)[seconds] \tag{5.7}$$

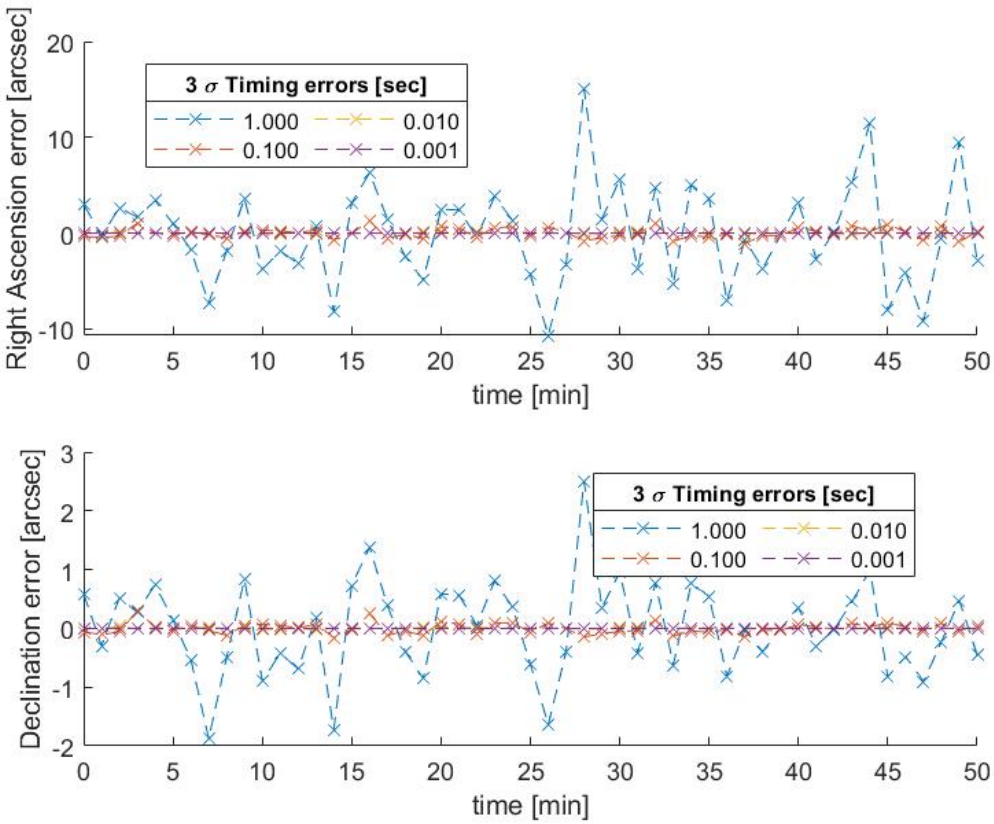

Fig. 5.19. MOLNIYA 3-24: Observation vs NLUMVE angle error distributions for unbiased timing error

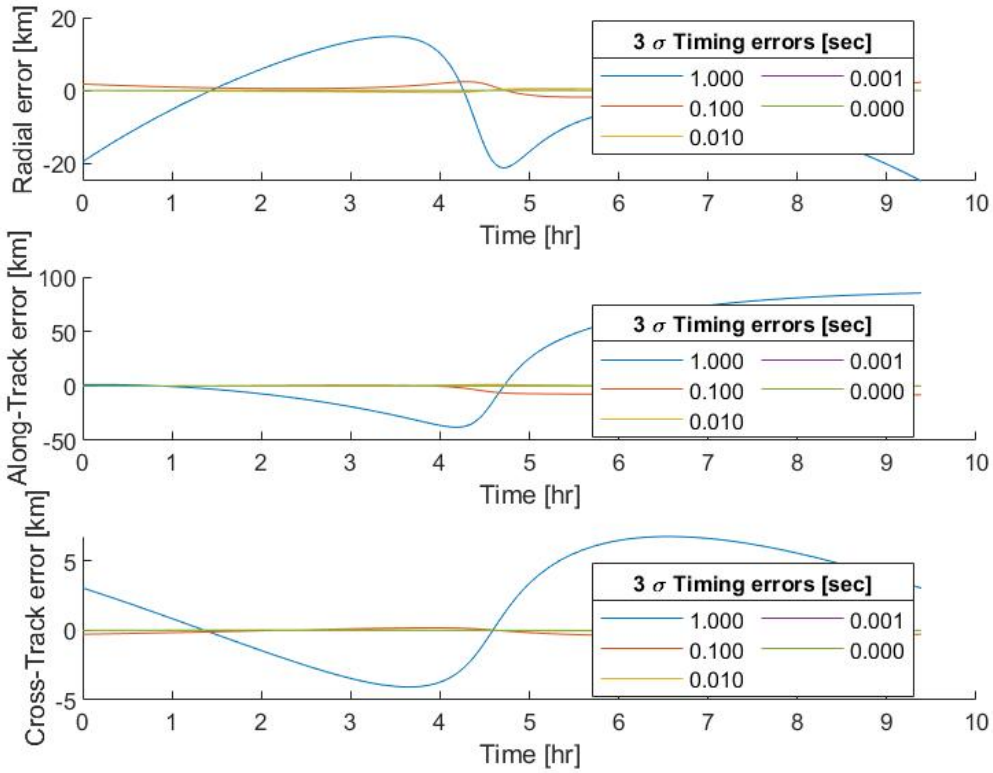

Fig. 5.20. MOLNIYA 3-24: RSW orbital errors, NLUMVE with modeled unbiased timing error vs truth

It is difficult to tell visually in Fig. 5.19 that the error distributions in the angle measurement are experiencing any non-normality. Yet, the Shapiro-Wilk Test still tests positive for the 0.001s HEO scenario, and the p-values for the other scenarios are relatively low. Across the scenarios, the maximum error values are lower than in the GPS timing scenarios due to the lower relative velocity of MOLNIYA 3-24 at apogee. However, the RSW plots in Fig. 5.20 show that the argument of perigee, when the satellite is moving fast, shifts to earlier in the orbit. Because this orbit in not circular, the orientation of the orbit has a large impact on the RSW errors. A shift in either the argument of perigee or the right ascension of the ascending node could serve as an indicator for HEO satellites that a data set of observations has poor timing. Table 5.7 shows the results for the unbiaesd timing error scenarios.

Table 5.7.
MOLNIYA 3-24: Shapiro-Wilk test results with RSW orbital errors for unbiased timing error scenarios

MOLNIYA 3-24	**Measurements vs. NLUMVE angles SW test**				**NLUMVE vs. Truth Orbit** (max errors)		
3σ Timing Error	W α	α P-val	W δ	δ P-val	Radial Error	Along-Track Error	Cross-Track Error
0.000 s	NaN	NaN	NaN	NaN	0.0048 m	0.0126 m	0.0004 m
0.001 s	0.9716	0.2576	0.9727	0.2859	37.706 m	89.824 m	3.9534 m
0.010 s	0.9790	0.4965	0.9480	0.0277	559.71 m	1,369.7 m	38.455 m
0.100 s	0.9676	0.1760	0.9603	0.0803	2,413.6 m	8,203.5 m	417.53 m
1.000 s	0.9772	0.3627	0.9607	0.0827	24,778 m	85,312 m	6,752.4 m

5.2.2 HEO Timing Bias

Timing bias is introduced in the HEO scenario in order to demonstrate the impact of poor timing in relation to optical measurements. The HEO scenario is run using a range of values for the β_t timing bias, 0.001 s to 1.000 s, and a small 3σ timing error of 0.001 s.

$$\Delta t_{error} \sim N(\beta_t, (.001/3)^2)[seconds] \tag{5.8}$$

Fig. 5.21 shows more random distributions for the angle errors, but the cases with larger cases still test positive for non-normality. As seen in Fig. 5.22, for the first

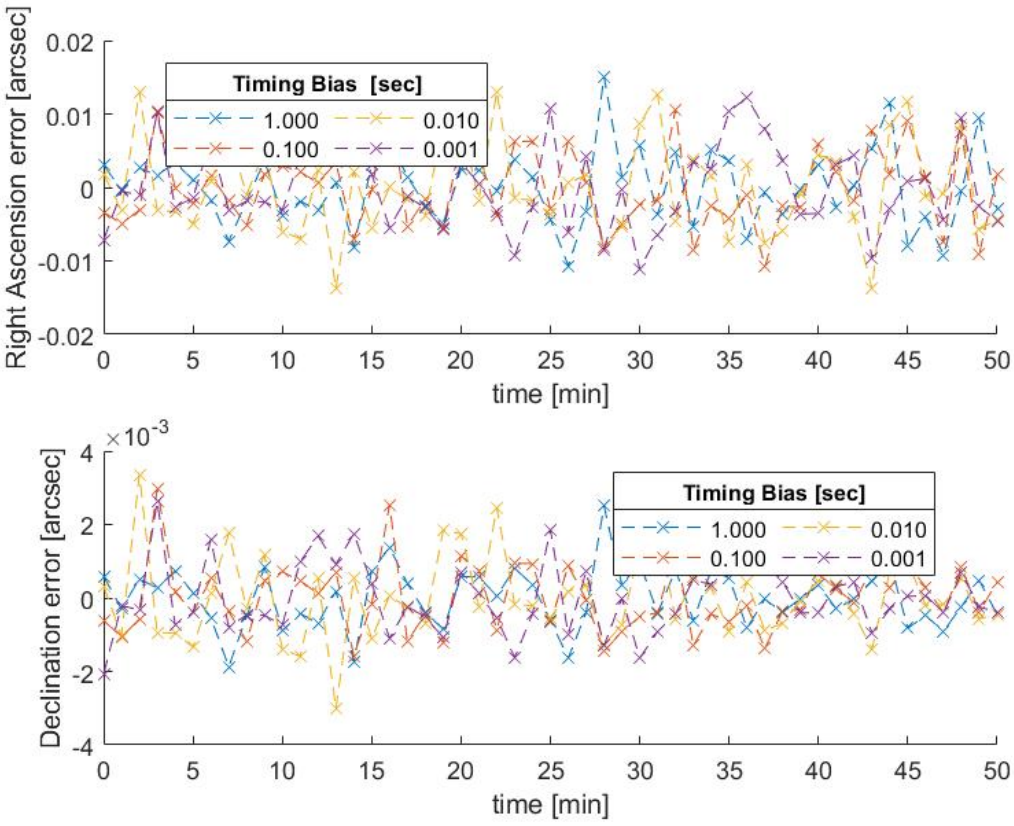

Fig. 5.21. MOLNIYA 3-24: Observation vs NLUMVE angle error distributions for biased timing error

case, the primary source of error is still from the small 3σ timing error, but the effect of bias is more prominent in this HEO scenario due to the elliptical shape since the magnitude of velocity changes along the orbit path. Poor timing can result in the wrong velocity at the initial state estimation. The effect is similar to section 5.1.2 where the argument of perigee and right ascension of the ascending node experience shifts, causing a misalignment in the orbit orientation. As timing bias increases, this shift in orientation will increase proportionally. Like the GEO scenario, the test results for the Shapiro-Wilk test on the angle errors do not change, which can be seen in Table 5.8.

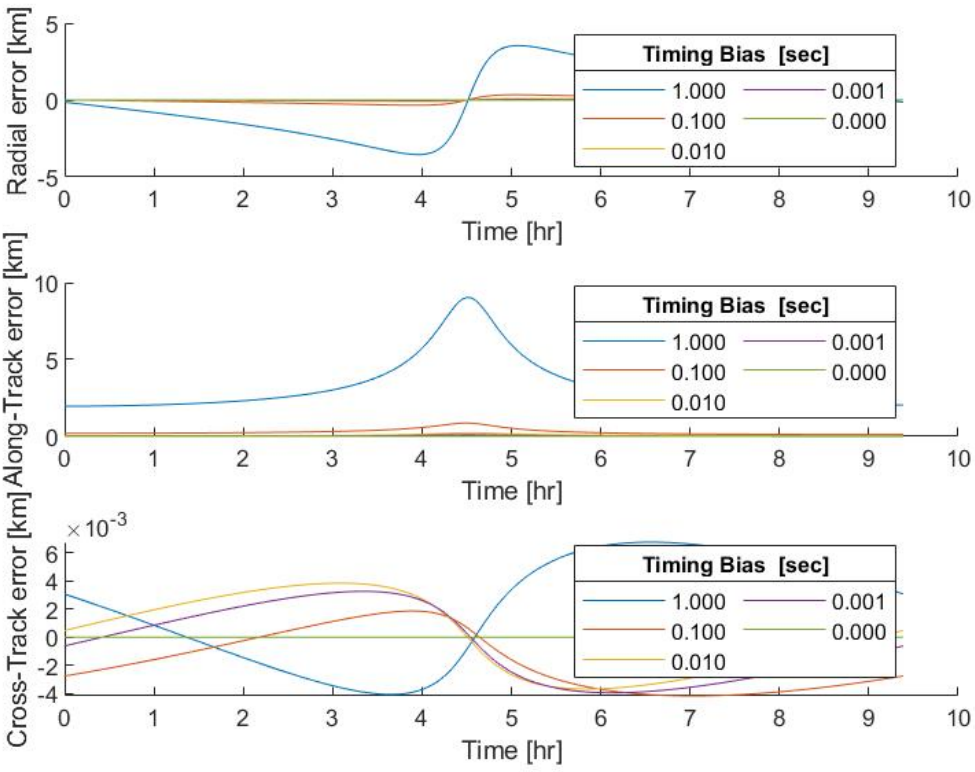

Fig. 5.22. MOLNIYA 3-24: RSW orbital errors, NLUMVE with biased timing error vs truth

Table 5.8.
MOLNIYA 3-24: Shapiro-Wilk test results with RSW orbital errors for biased timing error scenarios

MOLNIYA 3-24	**Measurements vs. NLUMVE angles SW test**				**NLUMVE vs. Truth Orbit** (max errors)		
Timing Bias	W α	α P-val	W δ	δ P-val	Radial Error	Along-Track Error	Cross-Track Error
0.000 s	NaN	NaN	NaN	NaN	37.706 m	89.824 m	3.9534 m
0.001 s	0.9716	0.2576	0.9727	0.2859	41.263 m	98.886 m	3.9534 m
0.010 s	0.9676	0.1760	0.9603	0.0803	91.473 m	227.37 m	3.8454 m
0.100 s	0.9790	0.4965	0.9480	0.0277	341.77 m	858.83 m	4.1744 m
1.000 s	0.9772	0.3627	0.9607	0.0827	3,547.2 m	9,039.0 m	6.7641 m

5.2.3 HEO Sidereal Timing Error

Sidereal timing error is introduced in the HEO scenario, which is run using a range of values for the $3\sigma_t$ sidereal timing error, 0.001 s to 1.000 s:

$$\Delta t_{error} \sim N(0, \sigma_t^2)[seconds] \tag{5.9}$$

In Fig. 5.23, the declination error distribution undergoes a nonlinear transformation as the initial state estimate from the least squares method does not align with the measurements. This can be explained by the object velocity retarding as it approaching apogee. Table 5.9 shows that the distribution testing detected problems with all declination observation sets. The RSW errors in Fig. 5.24 show emphasized curves for the larger error values. The peaks occur when the object is moving fastest in its orbit, which is at perigee. It can also be seen in the along-track component plot, that the error values do not return to a minimum and that the orbit needs additional observations in order to return to the initial state.

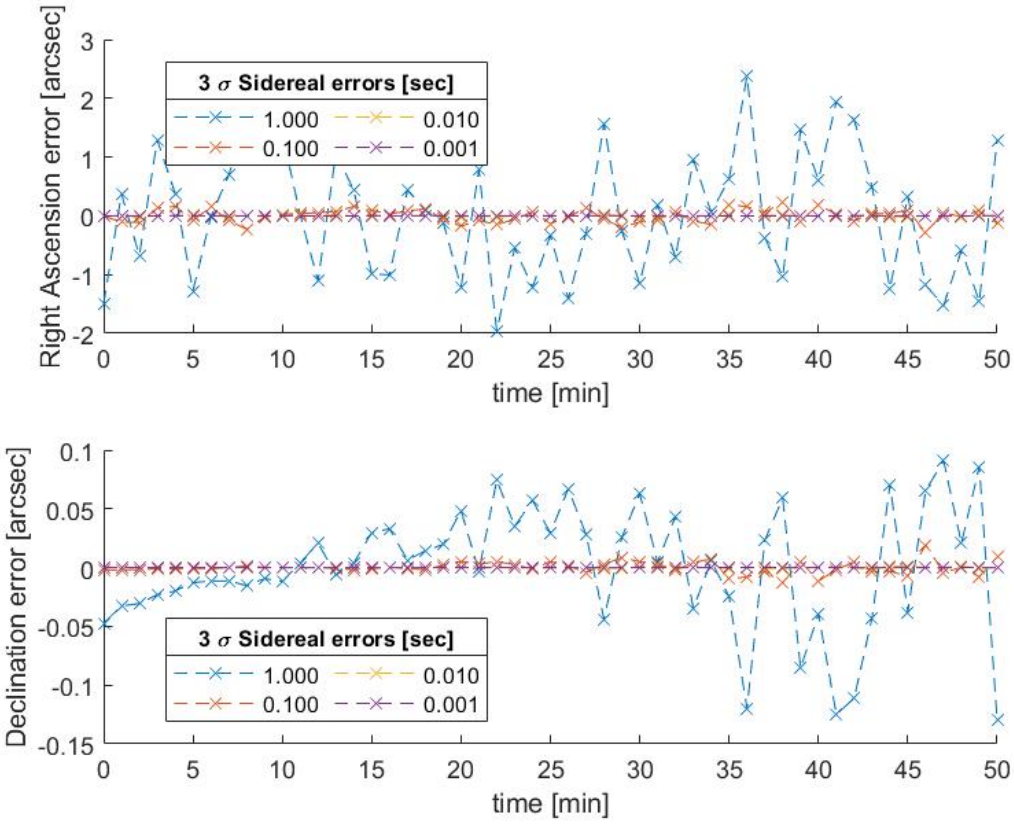

Fig. 5.23. MOLNIYA 3-24: Observation vs NLUMVE angle error distributions for unbiased sidereal timing error

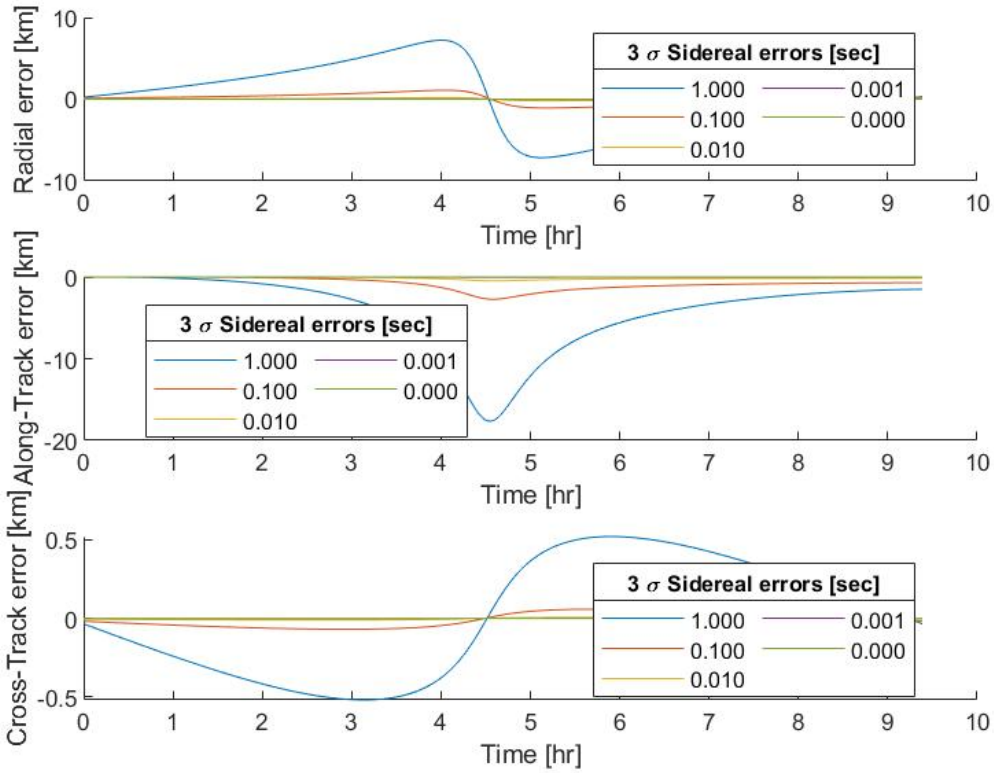

Fig. 5.24. MOLNIYA 3-24: RSW orbital errors, NLUMVE with modeled unbiased sidereal timing error vs truth

Table 5.9.
MOLNIYA 3-24: Shapiro-Wilk test results with RSW orbital errors for unbiased sidereal timing error scenarios

MOLNIYA 3-24	**Measurements vs. NLUMVE angles SW test**				**NLUMVE vs. Truth Orbit** (max errors)		
3σ Sidereal Error	W α	α P-val	W δ	δ P-val	Radial Error	Along-Track Error	Cross-Track Error
0.000 s	NaN	NaN	NaN	NaN	0.0048 m	0.0126 m	0.0004 m
0.001 s	0.9689	0.1997	0.9480	0.0277	19.341 m	48.016 m	1.0966 m
0.010 s	0.9714	0.2527	0.9303	0.0068	190.36 m	472.53 m	9.9902 m
0.100 s	0.9827	0.6560	0.9302	0.0067	1,101.7 m	2,724.0 m	69.165 m
1.000 s	0.9674	0.1722	0.9555	0.0524	7,219.4 m	17,646 m	521.49 m

5.2.4 HEO Sidereal Timing Bias

Sidereal timing bias is introduced in the HEO scenario. It is run using a range of values for the β_t timing bias, 0.001 s to 1.000 s, and a small 3σ timing error of 0.001 s.

$$\Delta t_{error} \sim N(\beta_t, (.001/3)^2)[seconds] \tag{5.10}$$

Fig. 5.25 shows that the angle error distributions from the unbiased scenarios are emphasized in this biased scenario. Fig. 5.26 and Table 5.10 similar results where all declination observation sets test positive with the Shapiro-Wilk Test. The bias has a great effect on the least squares method's ability to estimate the intiail state. With errors in the initial state, orbit RSW errors cannot return to a lower error state; it can only become worse.

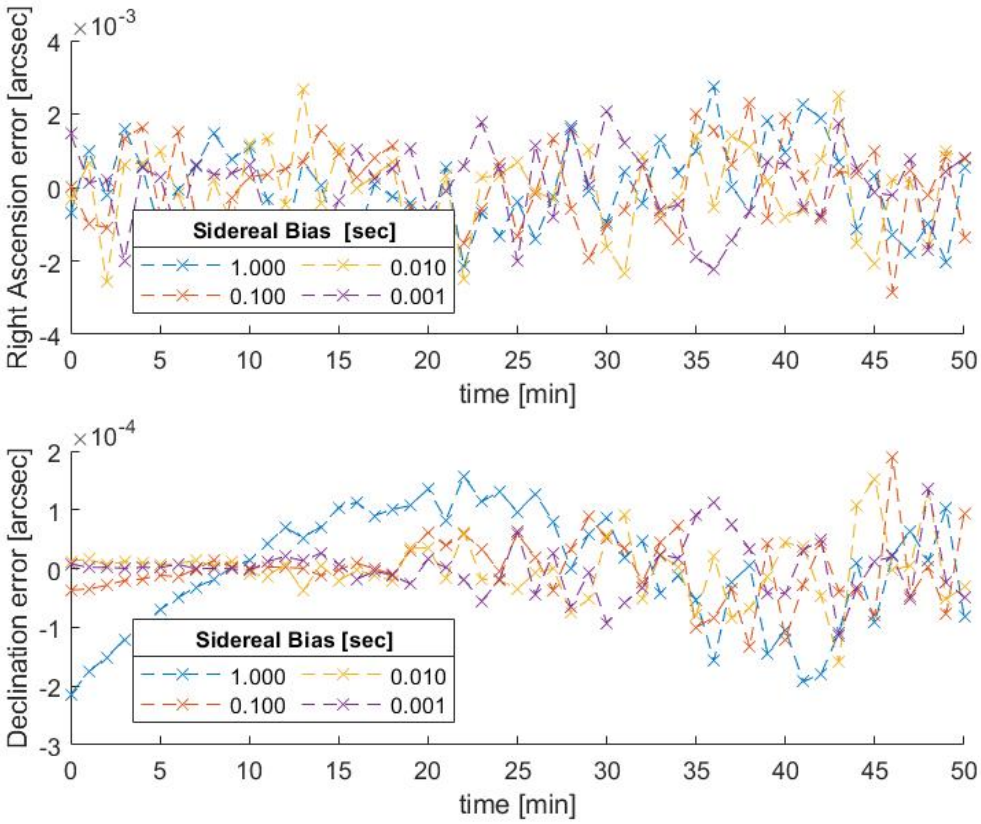

Fig. 5.25. MOLNIYA 3-24: Observation vs NLUMVE angle error distributions for biased sidereal timing error

Table 5.10.
MOLNIYA 3-24: Shapiro-Wilk test results with RSW orbital errors for biased sidereal timing error scenarios

MOLNIYA 3-24	**Measurements vs. NLUMVE angles SW test**				**NLUMVE vs. Truth Orbit** (max errors)		
Sidereal Bias	W α	α P-val	W δ	δ P-val	Radial Error	Along-Track Error	Cross-Track Error
0.000 s	NaN	NaN	NaN	NaN	19.341 m	48.016 m	1.0966 m
0.001 s	0.9689	0.1998	0.9479	0.0275	19.748 m	49.097 m	1.1331 m
0.010 s	0.9713	0.2495	0.9284	0.0058	23.101 m	58.051 m	2.2967 m
0.100 s	0.9839	0.7120	0.9535	0.0440	51.753 m	135.38 m	19.255 m
1.000 s	0.9820	0.6271	0.9479	0.0257	414.92 m	1,099.7 m	188.87 m

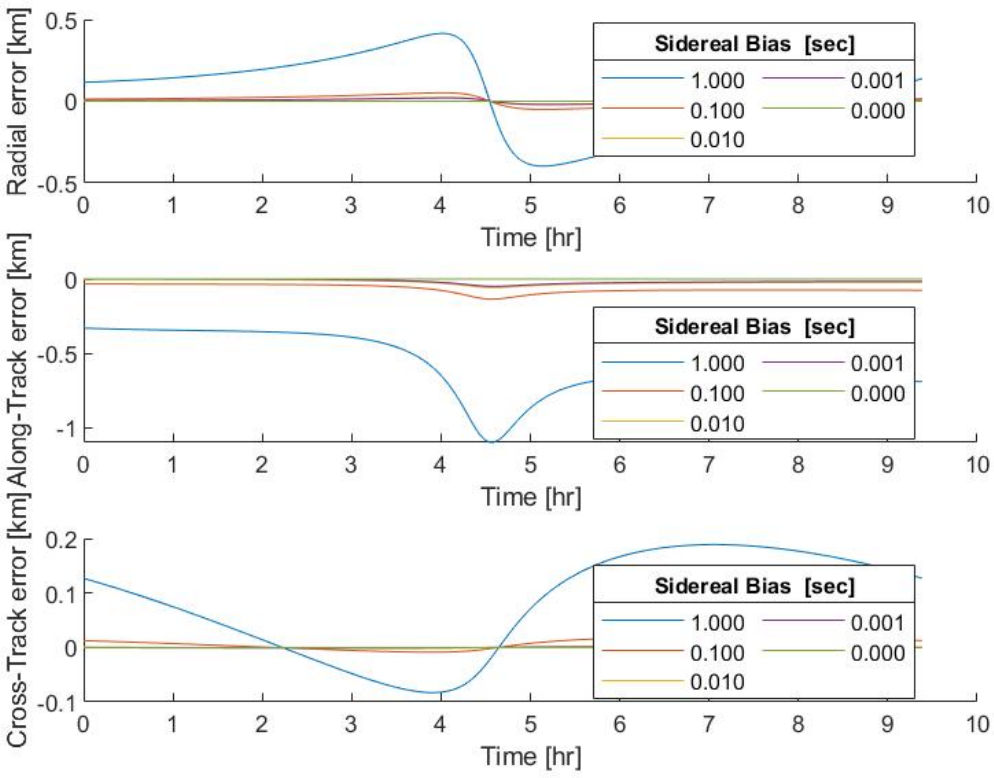

Fig. 5.26. MOLNIYA 3-24: RSW orbital errors, NLUMVE with modeled biased sidereal timing error vs truth

5.2.5 HEO Angle Measurement Error

Angle Measurement error is introduced in the HEO scenario and is run using a range of values for the $3\sigma_{ang}$ angle measurement error, 0.1 arcseconds to 100.0 arcsecs for both right ascension and declination:

$$\Delta ang_{error} \sim N(0, \sigma^2_{ang})[arcseconds] \tag{5.11}$$

In Fig. 5.27, the angle error distributions show normally distributed errors, which is agreement with the results of the GEO scenarios. The results in Table 5.11 confirms that for most of the data sets, there are no unusual patterns in the error distributions.

Not one of the cases tests positive for the right ascension or declination observations. The RSW errors in Fig. 5.28 show the most severe error values thus far for the HEO scenarios exceeding 1,000 km in the along-track component at perigee. Again, this shows the importance of angle error correction before performing orbit determination. Again, it is not recommended that distribution testing be used for detecting unbiased measurement error.

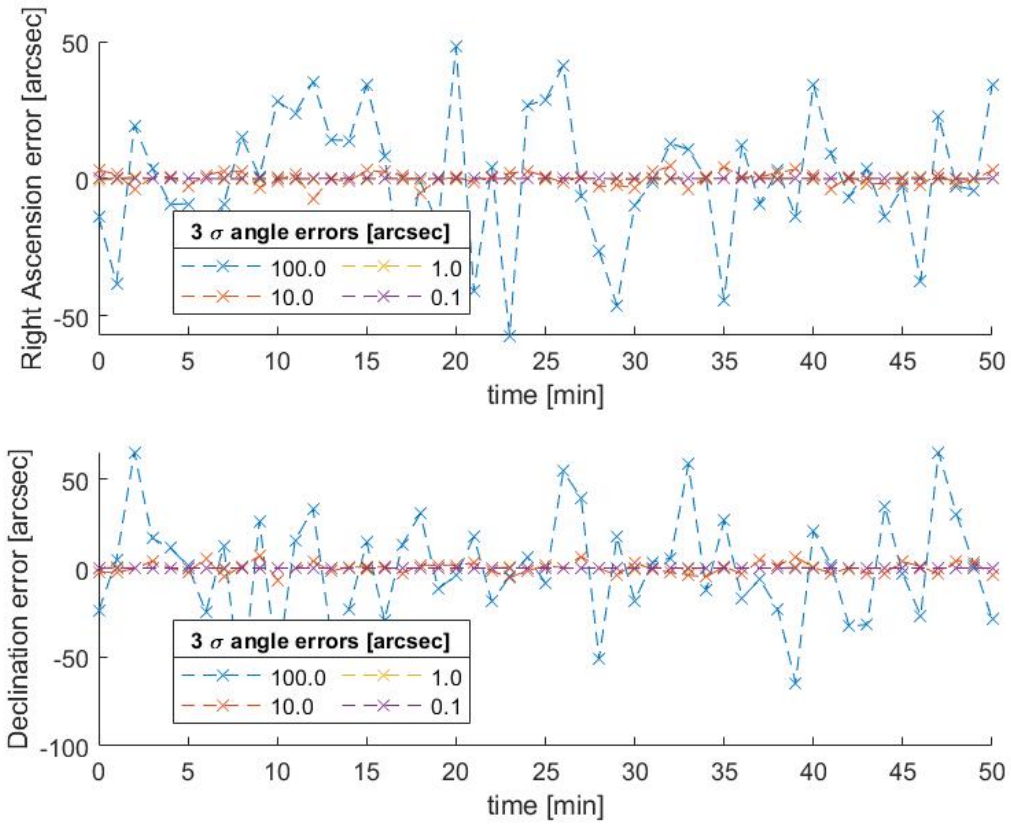

Fig. 5.27. MOLNIYA 3-24: Observation vs NLUMVE angle error distributions for unbiased angle measurement error

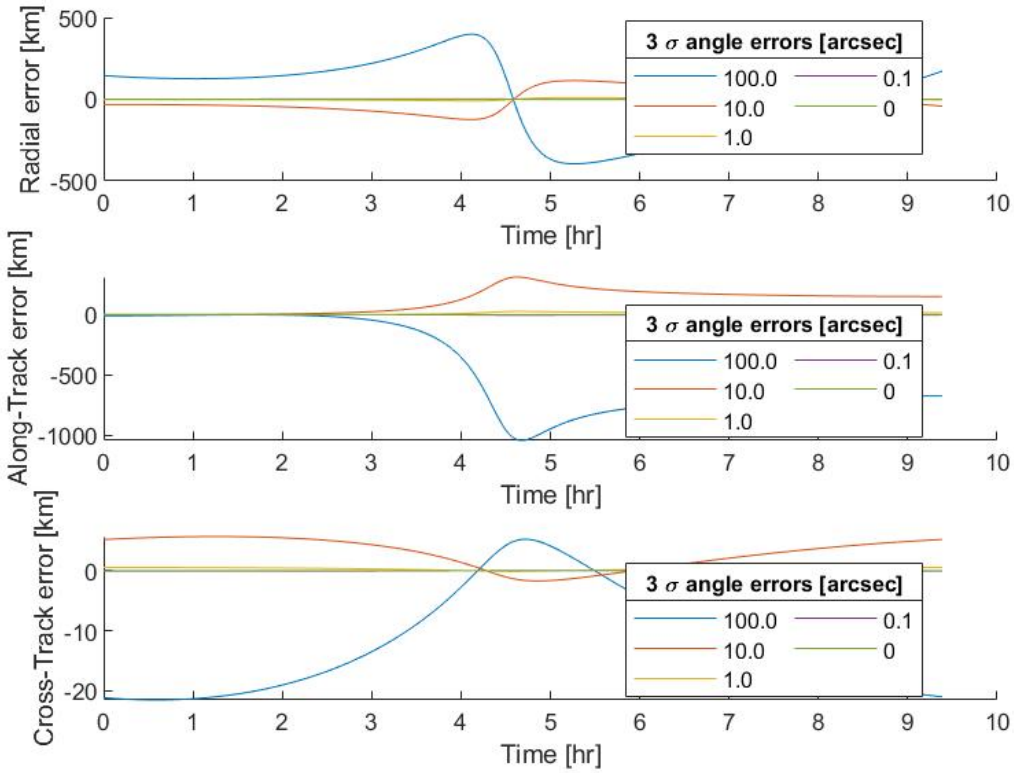

Fig. 5.28. MOLNIYA 3-24: RSW orbital errors, NLUMVE with modeled unbiased angle measurement error vs truth

Table 5.11.
MOLNIYA 3-24: Shapiro-Wilk test results with RSW orbital errors for unbiased angle measurement error scenarios

MOLNIYA 3-24	**Measurements vs. NLUMVE angles SW test**				**NLUMVE vs. Truth Orbit** (max errors)		
3σ Angle Error	W α	α P-val	W δ	δ P-val	Radial Error	Along-Track Error	Cross-Track Error
0 arcsec	NaN	NaN	NaN	NaN	0.0048 m	0.0126 m	0.0004 m
0.1 arcsec	0.9718	0.2614	0.9819	0.6239	1,583.8 m	3,992.1 m	72.588 m
1.0 arcsec	0.9872	0.8524	0.9894	0.9266	10,614 m	26,979 m	530.55 m
10.0 arcsec	0.9707	0.2370	0.9789	0.4919	124,460 m	311,260 m	5,666.5 m
100.0 arcsec	0.9768	0.4147	0.9872	0.8522	397,860 m	1,040,700 m	21,501 m

5.2.6 HEO Angle Measurement Bias

Angle measurement bias is introduced in the HEO scenario and is run using a range of values for the β_{ang} angle bias, 0.1 arcsecs to 100.0 arcsecs, and a small 3σ angle error of 0.1 arcsecs.

$$\Delta ang_{error} \sim N(\beta_{ang}, (.001/3)^2)[arcseconds] \tag{5.12}$$

It can be seen in Fig. 5.29 that the angle error distributions appear random for all scenarios. Fig. 5.30 and Table 5.12 show again that the distribution testing does not effectively detect angle measurement error. Since the bias does not affect the distribution shape itself, the distribution test results the scenarios with unbiased angle error. It is not recommended that distribution tests be used for detecting biased angle measurement error.

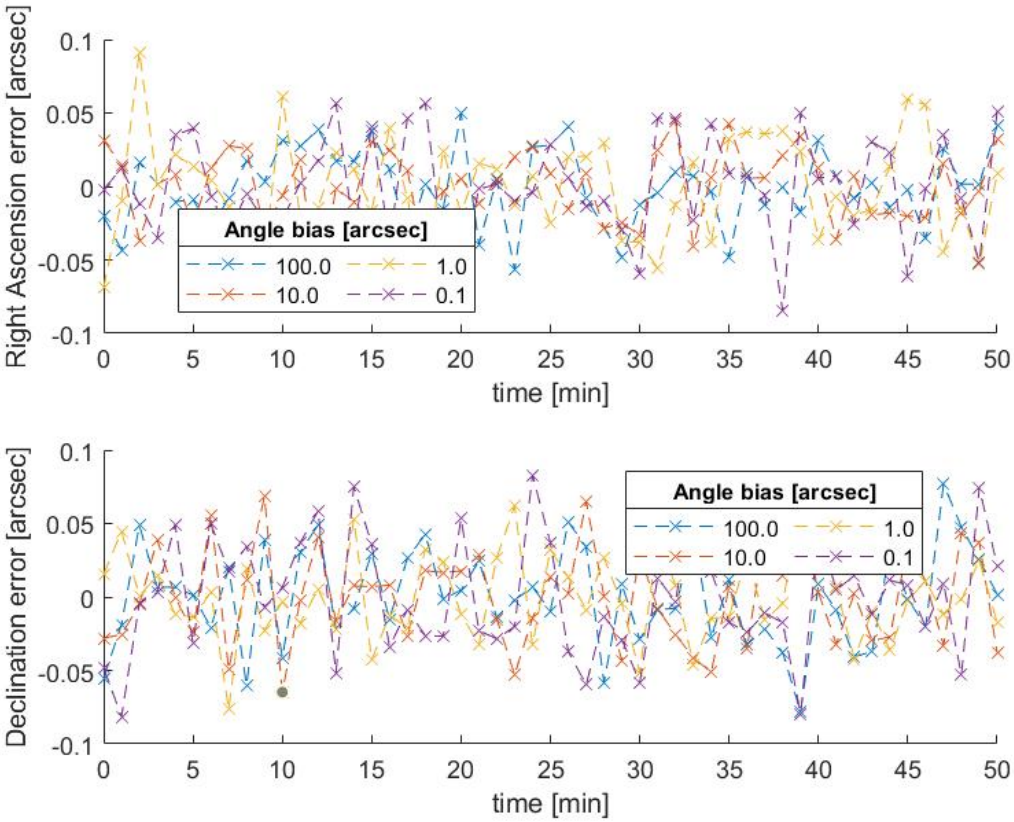

Fig. 5.29. MOLNIYA 3-24: Observation vs NLUMVE angle error distributions for biased angle measurement error

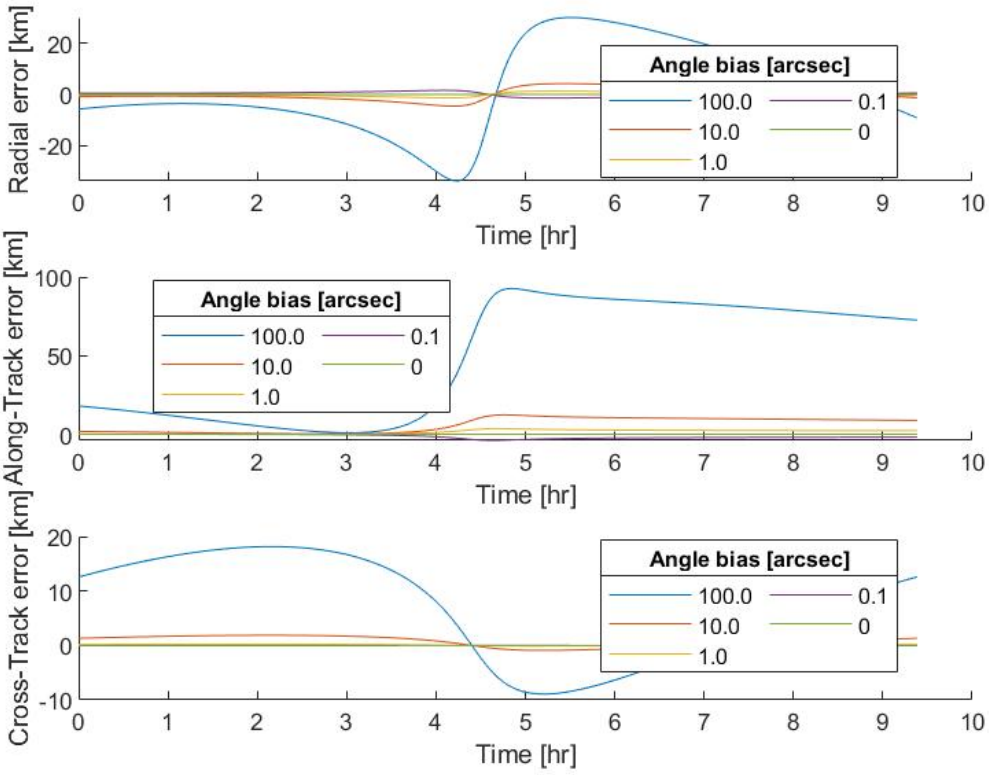

Fig. 5.30. MOLNIYA 3-24: RSW orbital errors, NLUMVE with modeled biased angle measurement error vs truth

Table 5.12.
MOLNIYA 3-24: Shapiro-Wilk test results with RSW orbital errors for biased angle measurement error scenarios

MOLNIYA 3-24	**Measurements vs. NLUMVE angles SW test**				**NLUMVE vs. Truth Orbit** (max errors)		
Angle Bias	W α	α P-val	W δ	δ P-val	Radial Error	Along-Track Error	Cross-Track Error
0 arcsec	NaN	NaN	NaN	NaN	1,583.8 m	3,992.1 m	72.588 m
0.1 arcsec	0.9718	0.2615	0.9819	0.6238	1,551.3 m	3,903.6 m	55.637 m
1.0 arcsec	0.9872	0.8529	0.9892	0.9216	1,392.8 m	3,603.8 m	225.03 m
10.0 arcsec	0.9704	0.2301	0.9782	0.4650	4,597.0 m	12,315 m	1,871.0 m
100.0 arcsec	0.9804	0.5563	0.9898	0.9385	33,702 m	92,642 m	18,154 m

5.3 Medium Earth Orbit: NAVSTAR 39 (USA 128)

For the MEO scenario, the American GPS satellite, NAVSTAR 39 is used, and its full circular orbit is shown in Fig. 5.31. It has a semi-major axis of 27,881 km, an eccentricity of 0.0027, an inclination of 55.5572°, a RAAN of 322.8298°, an argument of perigee of 162.3140°, and a true anomaly of 19.3067°. Orbital Elements are extracted from the state at the beginning of the observation window. For reference Fig. 5.32 shows right ascension increasing and declination decreasing nearly linearly during the 50-minute observation window.

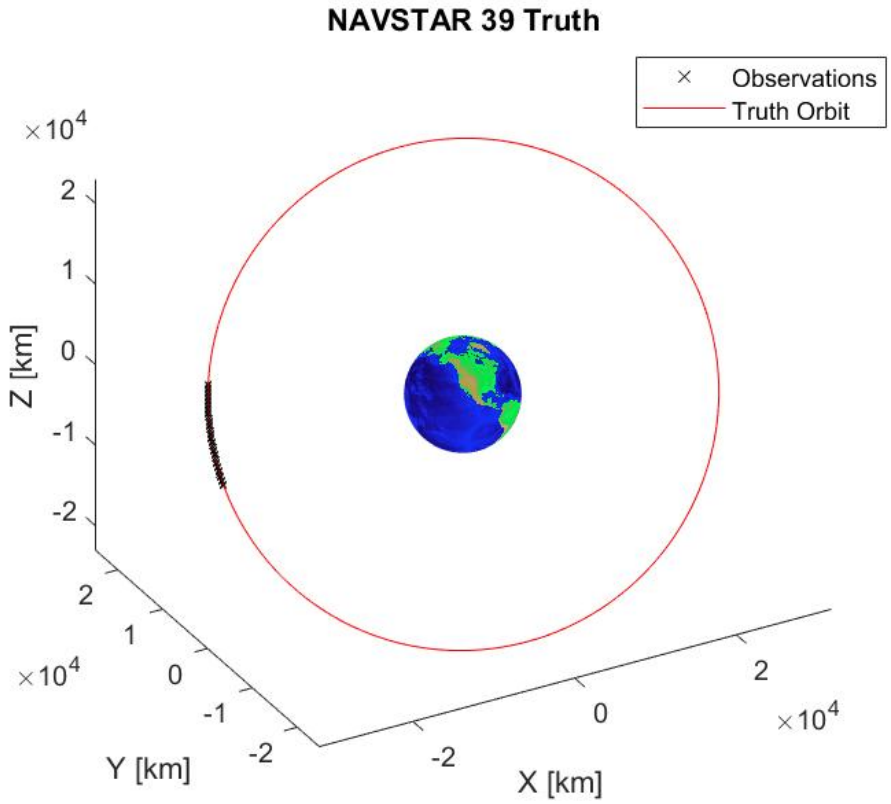

Fig. 5.31. NAVSTAR 39 (USA 128): Full truth orbit

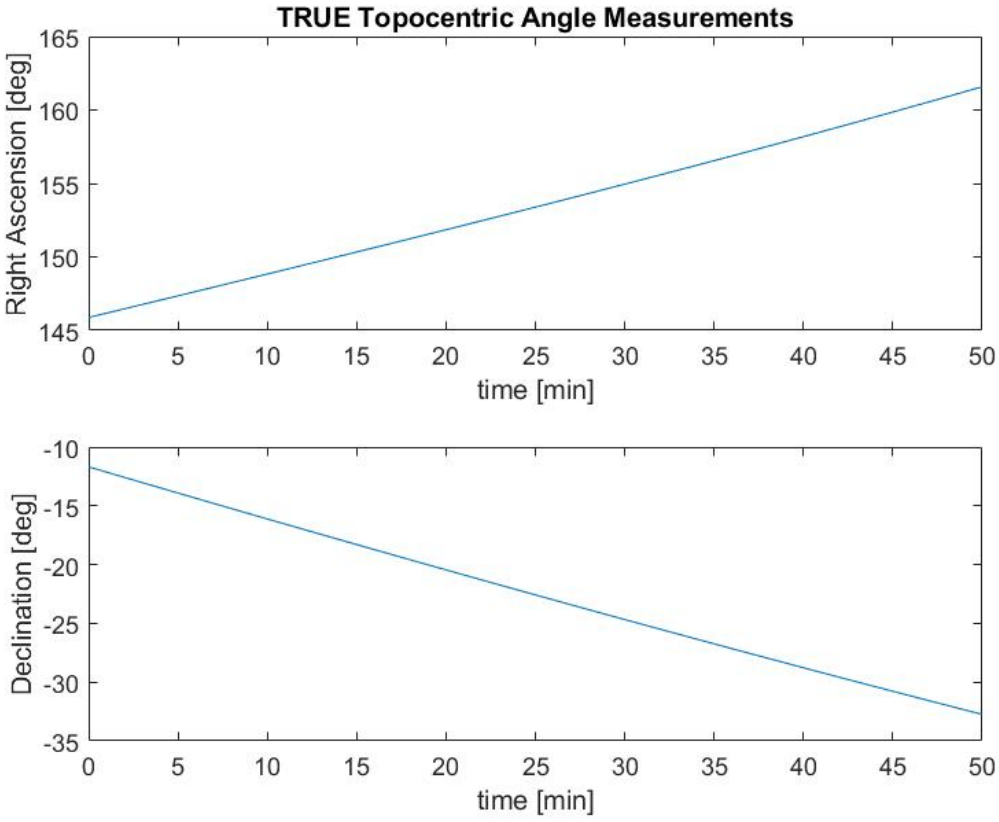

Fig. 5.32. NAVSTAR 39 (USA 128): True, error-free angle measurements

In Fig. 5.33, the least squares solution compared to the truth shows maximum errors value of 17.38 cm in the radial direction, 91.34 cm in the along-track direction, and 2.2 mm in the cross-track direction. This serves as a baseline level for RSW errors in MEO strictly from the least squares method. As expected, these values are much larger than the two previous orbit regions since the velocity of the satellite is higher, at approximately 3.7906 km/s. The trends during the whole orbit are similar to the previous scenarios where the orbital errors increase as the orbit is farthest from the initial state estimate and decrease with the orbit period for both the radial and cross-track components. The along-track component errors most resemble the GEO circular orbit in section 5.1: the estimate orbit trails farther behind after one orbit

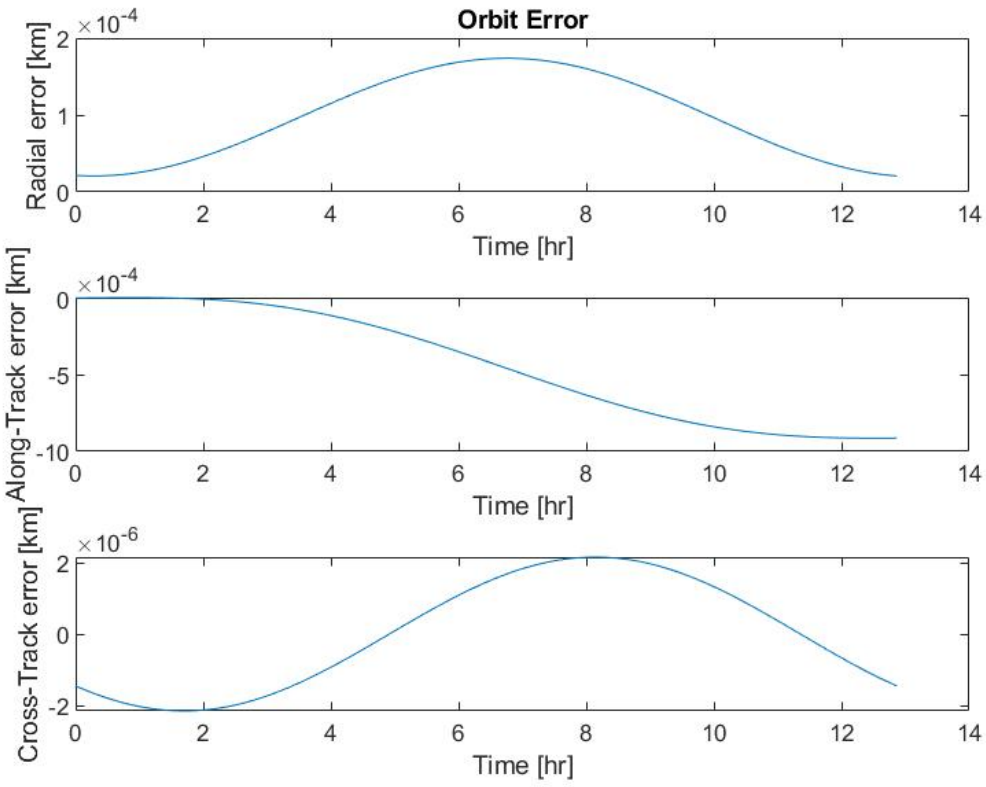

Fig. 5.33. NAVSTAR 39 (USA 128): RSW orbital errors, NLUMVE vs truth with no modeled errors

and does not improve cyclically. As errors from chapter 4 are introduced into the scenario, the orbital errors are expected to increase and become more pronounced due to the higher velocity.

5.3.1 MEO Timing Error

Timing error is introduced in the MEO scenario in order to demonstrate the impact of poor timing in relation to optical measurements. The MEO scenario is run using a range of values for the $3\sigma_t$ timing error, 0.001 s to 1.000 s.

$$\Delta t_{error} \sim N(0, \sigma_t^2)[seconds] \tag{5.13}$$

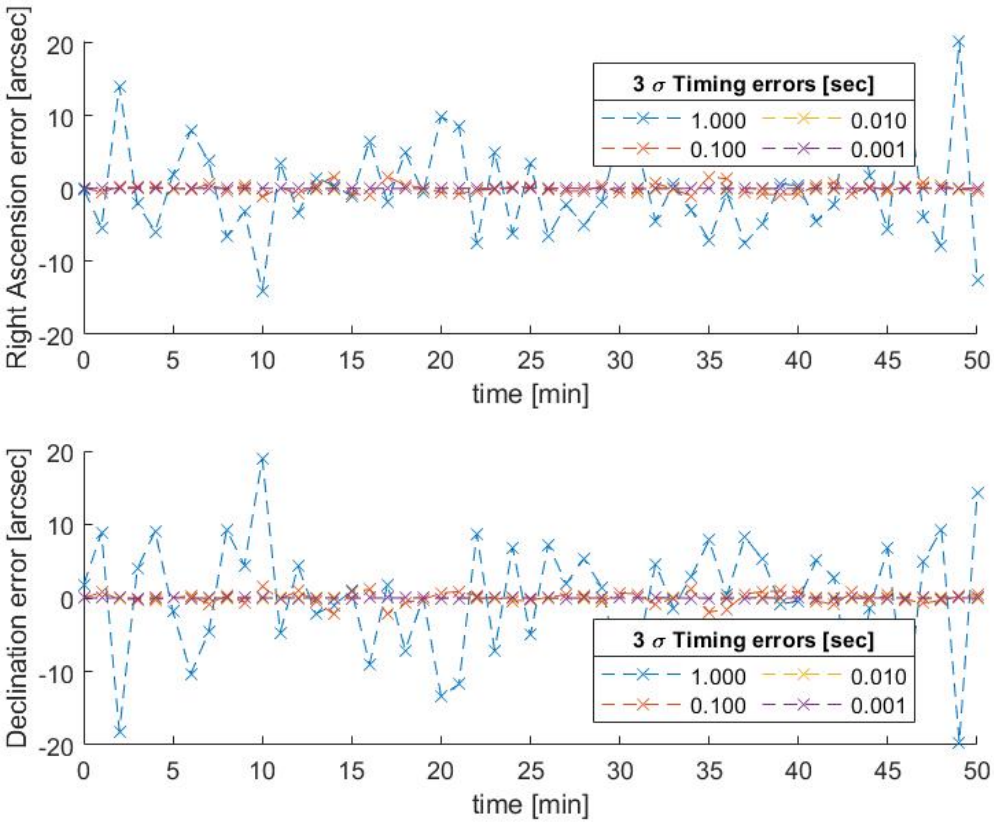

Fig. 5.34. NAVSTAR 39 (USA 128): Observation vs NLUMVE angle error distributions for unbiased timing error

Although the base error values for the MEO scenario were higher, the largest orbital error values of the 1.000s timing error scenario are not as high as the GEO scenario. Since the angle errors shown in Fig. 5.34 are computed using the least squares estimate, it is possible the test results are less informative. As errors become larger, the least squares estimate becomes less accurate when compared to the truth. Fig. 5.35 shows much larger values in RSW errors than previous scenarios. The combined effect presents difficulties in identifying the true errors of the angles. Though this is not favorable, testing was complete in this fashion to simulate lack of information in an operational environment. The results in Table 5.13 show that even still, the Shapiro-Wilk test is able to detect at least one scenario with a non-normal

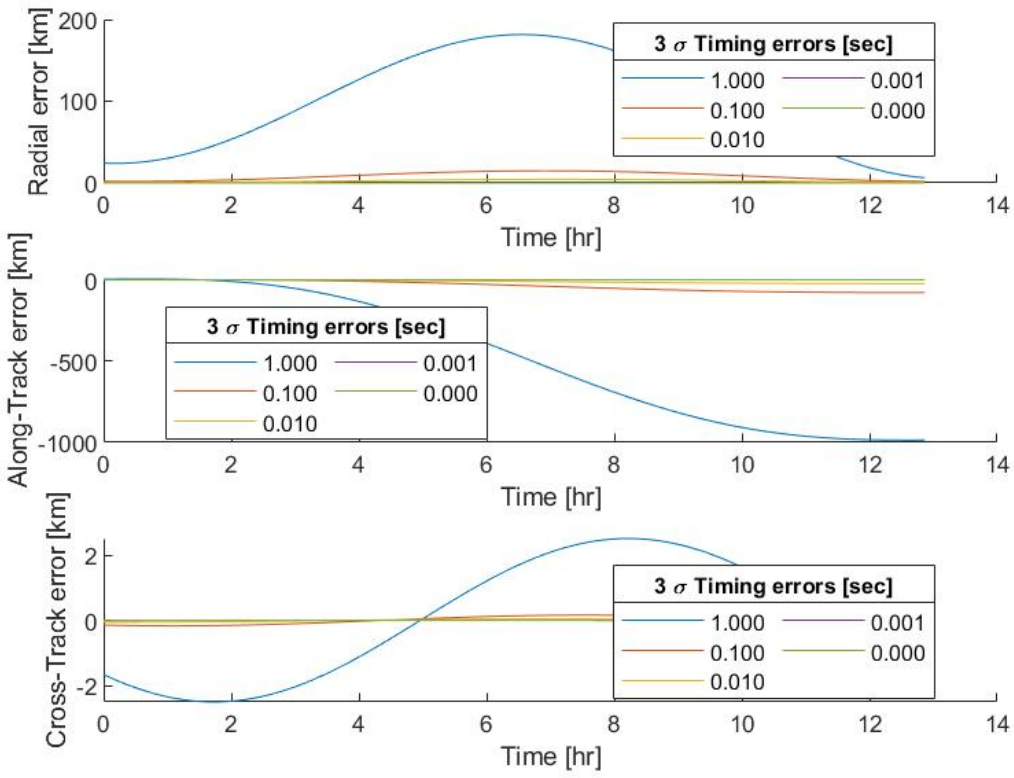

Fig. 5.35. NAVSTAR 39 (USA 128): RSW orbital errors, NLUMVE with unbiased timing error vs truth

distribution. The 0.001s and the 1.000s still have relatively low p-values under 0.25 and should prompt an orbit analyst to examine the observations closely, especially in the early stages of orbit determination. Performing the Shapiro-Wilk test, even with very little prior information can still be useful when sharing observation data.

Table 5.13.
NAVSTAR 39 (USA 128): Shapiro-Wilk test results with RSW orbital errors unbiased timing error scenarios

NAVSTAR 39	**Measurements vs. NLUMVE angles SW test**				**NLUMVE vs. Truth Orbit** (max errors)		
3σ Timing Error	W α	α P-val	W δ	δ P-val	Radial Error	Along-Track Error	Cross-Track Error
0.000 s	NaN	NaN	NaN	NaN	0.1738 m	0.9134 m	0.0022 m
0.001 s	0.9692	0.2055	0.9656	0.1443	18.043 m	38.653 m	1.0455 m
0.010 s	0.9933	0.9926	0.9836	0.6974	4,334.5 m	23,097 m	49.895 m
0.100 s	0.9541	0.0466	0.9508	0.0350	14,803 m	783,870 m	163.58 m
1.000 s	0.9552	0.0512	0.9694	0.2089	181,630 m	985,820 m	2503.6 m

5.3.2 MEO Timing Bias

Timing bias is introduced in the MEO scenario in order to demonstrate the impact of poor timing in relation to optical measurements. The MEO scenario is run using a range of values for the β_t timing bias, 0.001 s to 1.000 s, and a small 3σ timing error of 0.001 s.

$$\Delta t_{error} \sim N(\beta_t, (.001/3)^2)[seconds] \tag{5.14}$$

Because the GPS satellite orbit is circular, timing bias does not have as large of effect as the HEO scenario. The resultant effect on the orbit RSW errors is similar to the GEO scenario, and like the GEO scenario, the test results for the Shapiro-Wilk test on the angle errors do not change. The simplest way to determine if there is a timing bias is to note the periodical changes in the RSW errors. For example, Fig. 5.37 shows that after one period, the radial and cross-track errors return to the same point, but the along-track component only gets larger. The delay in timing causes the estimate to trail behind the true orbit unless further corrections are made with more measurements.

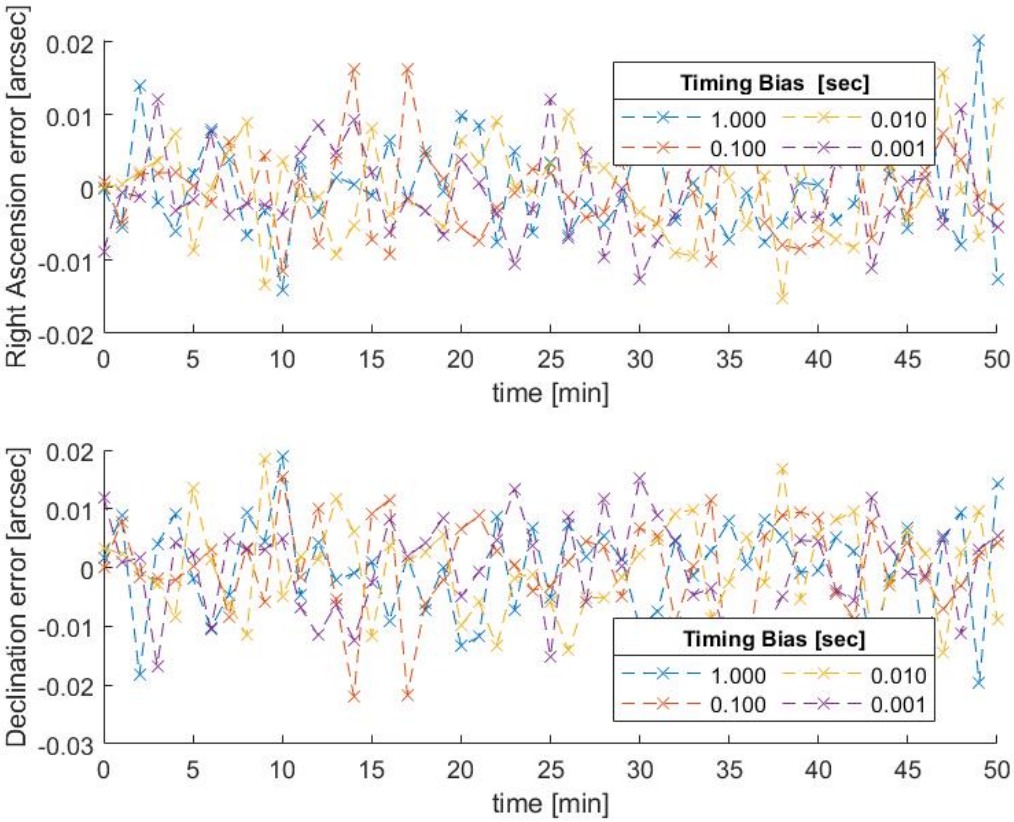

Fig. 5.36. NAVSTAR 39 (USA 128): Observation vs NLUMVE angle error distributions for biased timing error

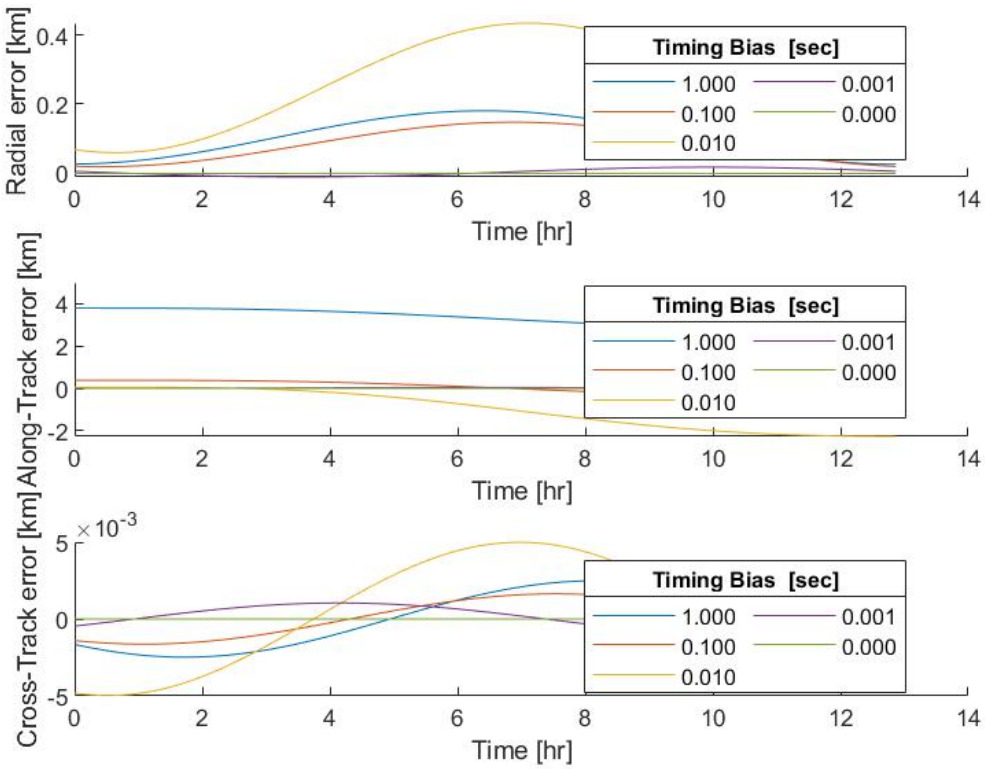

Fig. 5.37. NAVSTAR 39 (USA 128): RSW orbital errors, NLUMVE with biased timing error vs truth

Table 5.14.
NAVSTAR 39 (USA 128): Shapiro-Wilk test results with RSW orbital errors for biased timing error scenarios

NAVSTAR 39	Measurements vs. NLUMVE angles SW test				NLUMVE vs. Truth Orbit (max errors)		
Timing Bias	W α	α P-val	W δ	δ P-val	Radial Error	Along-Track Error	Cross-Track Error
0.000 s	NaN	NaN	NaN	NaN	18.043 m	38.653 m	1.0455 m
0.001 s	0.9692	0.2055	0.9656	0.1443	18.035 m	42.424 m	1.0455 m
0.010 s	0.9933	0.9926	0.9836	0.6974	433.69 m	50.736 m	4.9903 m
0.100 s	0.9541	0.0466	0.9508	0.0350	147.87 m	405.20 m	1.6367 m
1.000 s	0.9552	0.0512	0.9694	0.2089	180.71 m	3,794.7 m	2.4871 m

5.3.3 MEO Sidereal Timing Error

Sidereal timing error is introduced in the MEO scenario, which is run using a range of values for the $3\sigma_t$ sidereal timing error, 0.001 s to 1.000 s:

$$\Delta t_{error} \sim N(0, \sigma_t^2)[seconds] \tag{5.15}$$

In Fig. 5.38, there are no apparent abnormalities in the angle error distributions. Table 5.15 confirms that for the scenarios, the distributions were not significantly non-normal. The 0.010 s and 1.000 s cases are marked with low p-values for their declination distributions. The RSW errors in Fig. 5.39 show large error values again, which is expected because the GPS satellite is moving at a higher velocity. The peaks occur when the object is farthest from its initial state estimate from the least squares method. It can also be seen in the along-track component plot, that the error values do not return to a minimum and that the orbit needs additional observations in order to return to the initial state. For closer orbit regions, the distribution testing is less effective, but was still able to detect the worst-case scenario here in MEO.

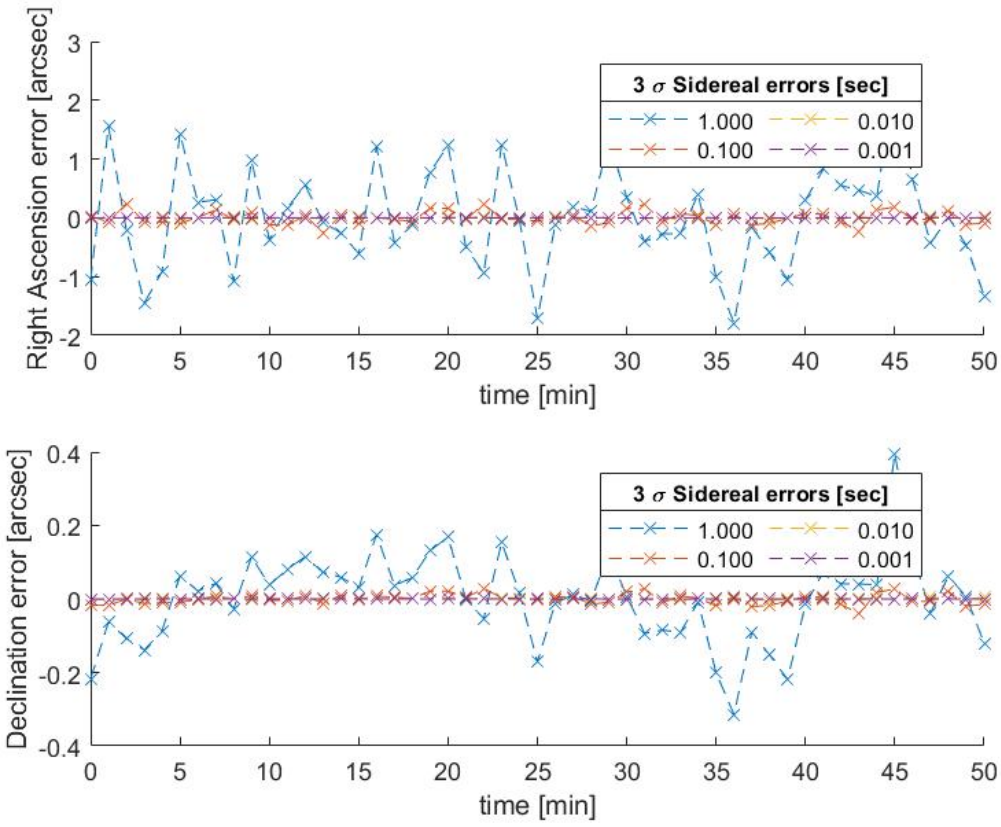

Fig. 5.38. NAVSTAR 39 (USA 128): Observation vs NLUMVE angle error distributions for unbiased sidereal timing error

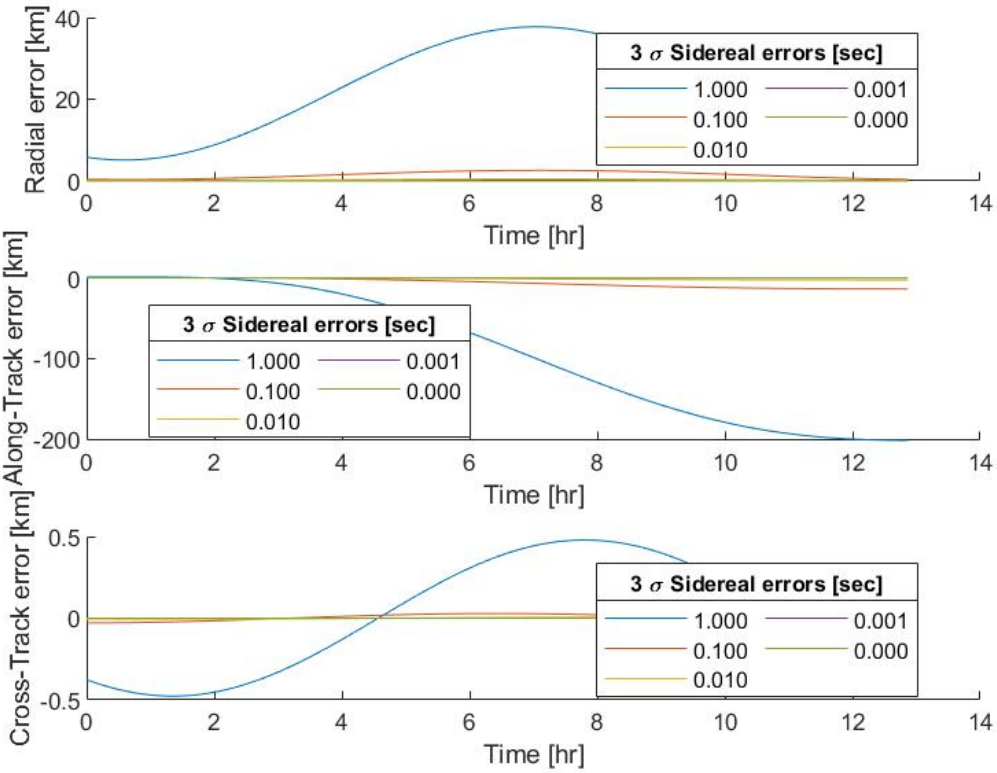

Fig. 5.39. NAVSTAR 39 (USA 128): RSW orbital errors, NLUMVE with modeled unbiased sidereal timing error vs truth

Table 5.15.
NAVSTAR 39 (USA 128): Shapiro-Wilk test results with RSW orbital errors for unbiased sidereal timing error scenarios

NAVSTAR 39	**Measurements vs. NLUMVE angles SW test**				**NLUMVE vs. Truth Orbit** (max errors)		
3σ Sidereal Error	W α	α P-val	W δ	δ P-val	Radial Error	Along-Track Error	Cross-Track Error
0.000 s	NaN	NaN	NaN	NaN	0.1738 m	0.9134 m	0.0022 m
0.001 s	0.9633	0.1151	0.9855	0.7857	35.949 m	191.06 m	0.4682 m
0.010 s	0.9876	0.8693	0.9561	0.0554	501.36 m	2,665.6 m	6.7592 m
0.100 s	0.9716	0.2563	0.9741	0.2757	2,584.9 m	13,715 m	28.727 m
1.000 s	0.9882	0.8897	0.9582	0.0663	37,728 m	201,530 m	478.49 m

5.3.4 MEO Sidereal Timing Bias

Sidereal timing bias is introduced in the MEO scenario. It is run using a range of values for the β_t timing bias, 0.001 s to 1.000 s, and a small 3σ timing error of 0.001 s.

$$\Delta t_{error} \sim N(\beta_t, (.001/3)^2)[seconds] \tag{5.16}$$

Fig. 5.40 shows that for the most extreme case, both the right ascension and declination error distribution experience very pronounced nonlinear transformations. Table 5.16 confirms that the distribution testing is able to detect medium to high levels of sidereal timing bias. Fig. 5.41 shows that the bias here has shifted the initial state from the least squares method and causes large errors over the whole orbital period.

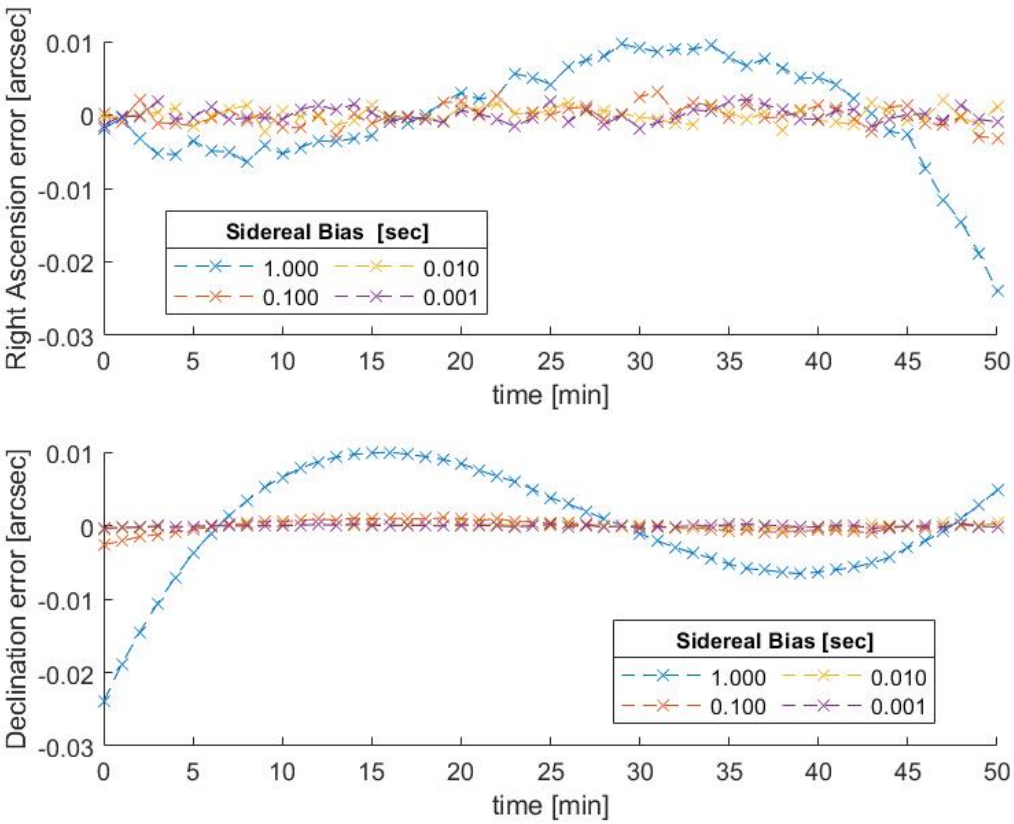

Fig. 5.40. NAVSTAR 39 (USA 128): Observation vs NLUMVE angle error distributions for biased sidereal timing error

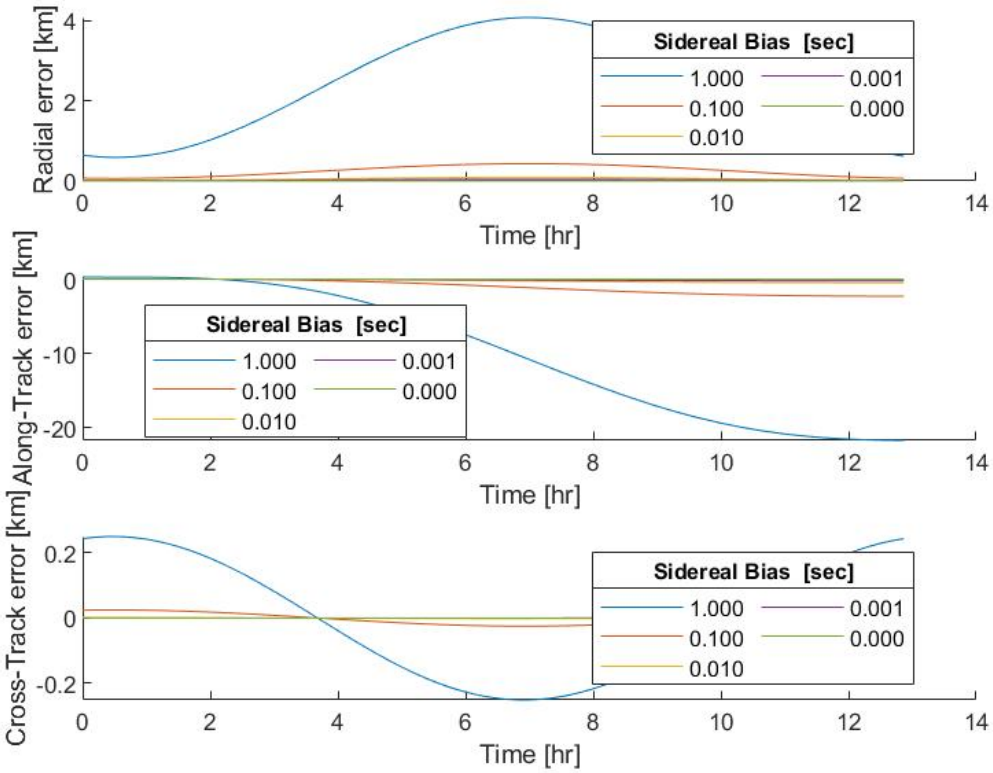

Fig. 5.41. NAVSTAR 39 (USA 128): RSW orbital errors, NLUMVE with modeled biased sidereal timing error vs truth

Table 5.16.
NAVSTAR 39 (USA 128): Shapiro-Wilk test results with RSW orbital errors for biased sidereal timing error scenarios

NAVSTAR 39	Measurements vs. NLUMVE angles SW test				NLUMVE vs. Truth Orbit (max errors)		
Sidereal Bias	W α	α P-val	W δ	δ P-val	Radial Error	Along-Track Error	Cross-Track Error
0.000 s	NaN	NaN	NaN	NaN	35.949 m	191.06 m	0.4682 m
0.001 s	0.9692	0.1113	0.9841	0.7212	39.989 m	212.53 m	0.2644 m
0.010 s	0.9865	0.8253	0.9803	0.5496	90.694 m	482.06 m	1.9578 m
0.100 s	0.9886	0.9019	0.9425	0.0176	430.01 m	2,284.7 m	24.929 m
1.000 s	0.9163	0.0024	0.9311	0.0072	4,076.9 m	21,673 m	251.68 m

5.3.5 MEO Angle Measurement Error

Angle Measurement error is introduced in the MEO scenario and is run using a range of values for the $3\sigma_{ang}$ angle measurement error, 0.1 arcseconds to 100.0 arcsecs for both right ascension and declination:

$$\Delta ang_{error} \sim N(0, \sigma^2_{ang})[arcseconds] \tag{5.17}$$

In Fig. 5.42, the angle error distributions show normally distributed errors, which is agreement with the results of the GEO and HEO scenarios. The results in Table 5.17 confirms that for most of the data sets. Only one of the cases tests positive for the declination observations; however, depending on the significance level of the test used, this may go unnoticed with p value of 0.0835. The RSW errors in Fig. 5.43 show the most severe error values thus far for the MEO scenarios exceeding 4,000 km in the along-track component at perigee. This is extremely large considering the truth orbit has a semi-major axis of 27,881 km. The distribution was unable to detect these egregious errors. This shows the importance of angle error correction before performing orbit determination. Again, it is not recommended that distribution testing be used for detecting unbiased measurement error.

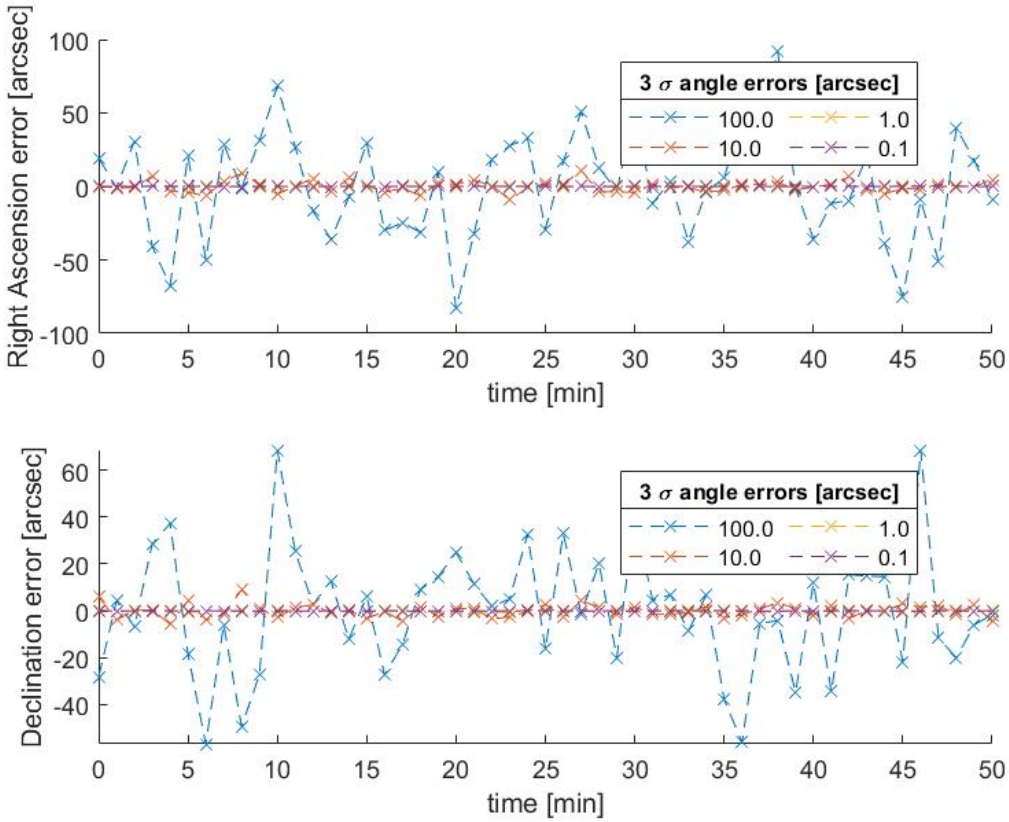

Fig. 5.42. NAVSTAR 39 (USA 128): Observation vs NLUMVE angle error distributions for unbiased angle measurement error

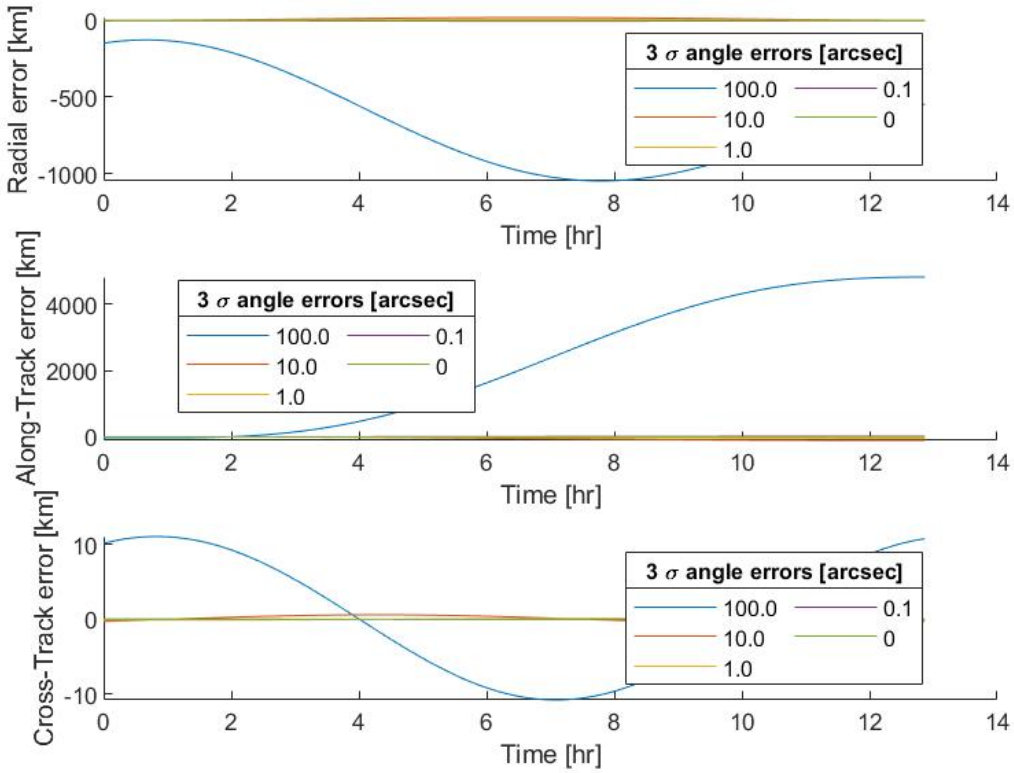

Fig. 5.43. NAVSTAR 39 (USA 128): RSW orbital errors, NLUMVE with modeled unbiased angle measurement error vs truth

Table 5.17.
NAVSTAR 39 (USA 128): Shapiro-Wilk test results with RSW orbital errors for unbiased angle measurement error scenarios

NAVSTAR 39	Measurements vs. NLUMVE angles SW test				NLUMVE vs. Truth Orbit (max errors)		
3σ Angle Error	W α	α P-val	W δ	δ P-val	Radial Error	Along-Track Error	Cross-Track Error
0 arcsec	NaN	NaN	NaN	NaN	0.1738 m	0.9134 m	0.0022 m
0.1 arcsec	0.9708	0.2050	0.9778	0.3805	2,614.3 m	14,028 m	28.715 m
1.0 arcsec	0.9824	0.6465	0.9600	0.0835	8,592.5 m	45,760 m	104.34 m
10.0 arcsec	0.9805	0.4744	0.9724	0.2373	20,699 m	109,540 m	593.77 m
100.0 arcsec	0.9909	0.9632	0.9807	0.4851	1,048,000 m	4,814,700 m	11,007 m

5.3.6 MEO Angle Measurement Bias

Angle measurement bias is introduced in the MEO scenario and is run using a range of values for the β_{ang} angle bias, 0.1 arcsecs to 100.0 arcsecs, and a small 3σ angle error of 0.1 arcsecs.

$$\Delta ang_{error} \sim N(\beta_{ang}, (.001/3)^2)[arcseconds] \tag{5.18}$$

It can be seen in Fig. 5.44 that the angle error distributions appear random for all scenarios. Fig. 5.45 and Table 5.18 show that some of the shifts in the errors allow the distribution testing to be more effective in detecting angle measurement error bias. At this nearer orbit region, the distribution testing marked all of the cases with relatively low p-values under 0.200. These results indicate that it is possible that distribution tests can detect biased angle measurement error.

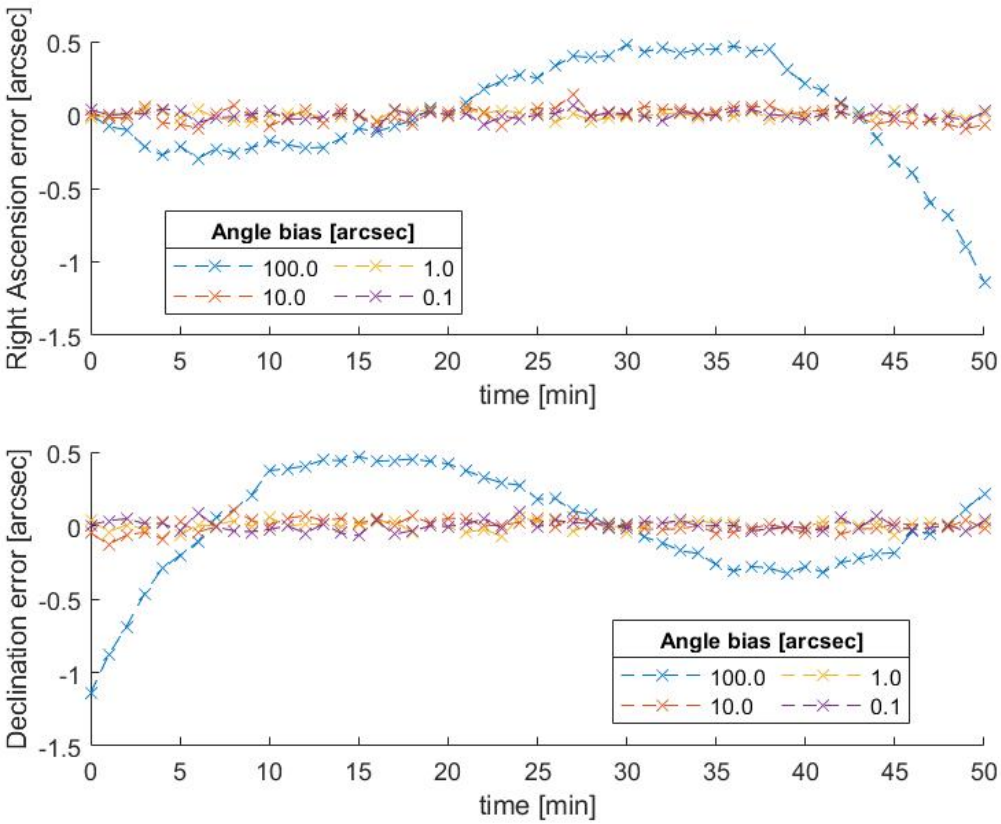

Fig. 5.44. NAVSTAR 39 (USA 128): Observation vs NLUMVE angle error distributions for biased angle measurement error

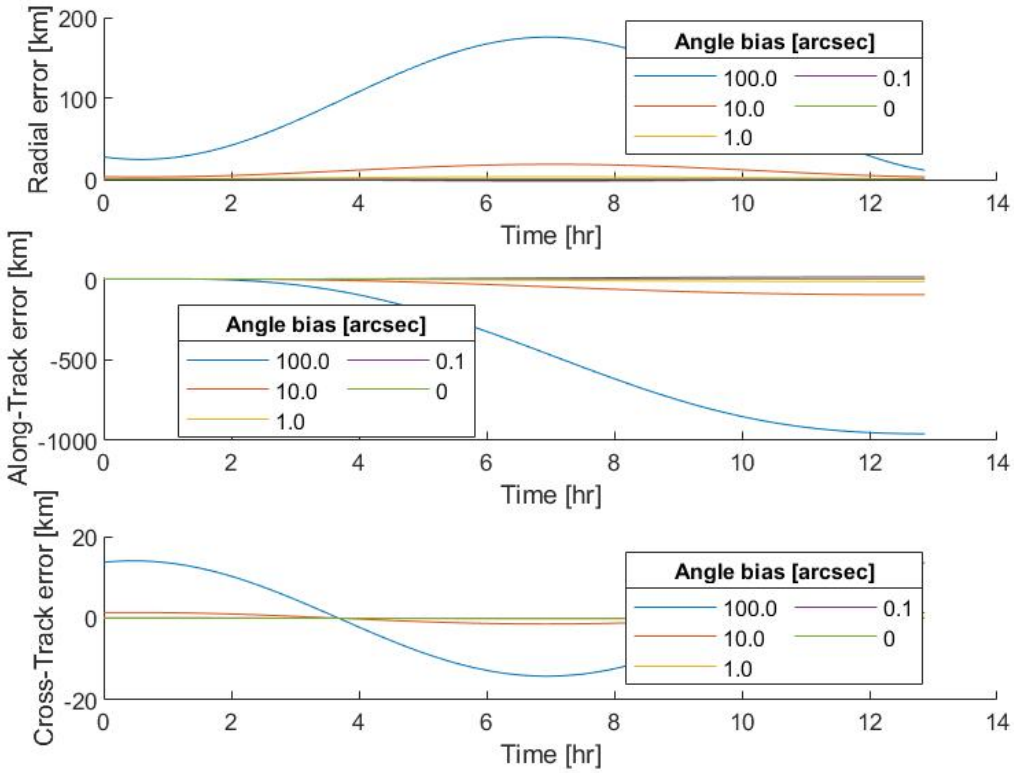

Fig. 5.45. NAVSTAR 39 (USA 128): RSW orbital errors, NLUMVE with modeled biased angle measurement error vs truth

Table 5.18.
NAVSTAR 39 (USA 128): Shapiro-Wilk test results with RSW orbital errors for biased angle measurement error scenarios

NAVSTAR 39	Measurements vs. NLUMVE angles SW test				NLUMVE vs. Truth Orbit (max errors)		
Angle Bias	W α	α P-val	W δ	δ P-val	Radial Error	Along-Track Error	Cross-Track Error
0 arcsec	NaN	NaN	NaN	NaN	2,614.3 m	14,028 m	28.715 m
0.1 arcsec	0.9706	0.2021	0.9769	0.3511	2,461.6 m	13,070 m	42.749 m
1.0 arcsec	0.9729	0.2915	0.9561	0.0572	2,655.4 m	14,157 m	131.41 m
10.0 arcsec	0.9671	0.1679	0.9785	0.4052	18,141 m	96,966 m	1,407.9 m
100.0 arcsec	0.9252	0.0046	0.9261	0.0049	175,720 m	959,370 m	14,189 m

5.4 Low Earth Orbit: IRIDIUM 96

For LEO, the communications satellite, IRIDIUM 96 is selected, shown in Fig. 5.46. It has a semi-major axis of 6,775 km, an eccentricity of 0.0168, an inclination of 86.3664°, a RAAN of 295.2318°, an argument of perigee of 312.9567°, and a true anomaly of 83.2615°. Orbital Elements are extracted from the state at the beginning of the observation window. The same observation window as the previous satellites is not viable because of the shorter orbitals periods of LEO (approximately 80-130 minutes). Instead, observations are extracted for a 5-minute window at 6-second intervals. Observer conditions are the same at Purdue University, West Lafayette, Indiana. This simulation ensures the same sample size as before, $n = 51$. As before, these observations have perfect, error-free angle measurements, topocentric right ascension and declination. For reference, the true angle measurements for the observation window are shown in Fig. 5.47 in degrees. Both right ascension and declination are increasing nearly linear for the duration of the observation window. The same method for orbit determination is used as before.

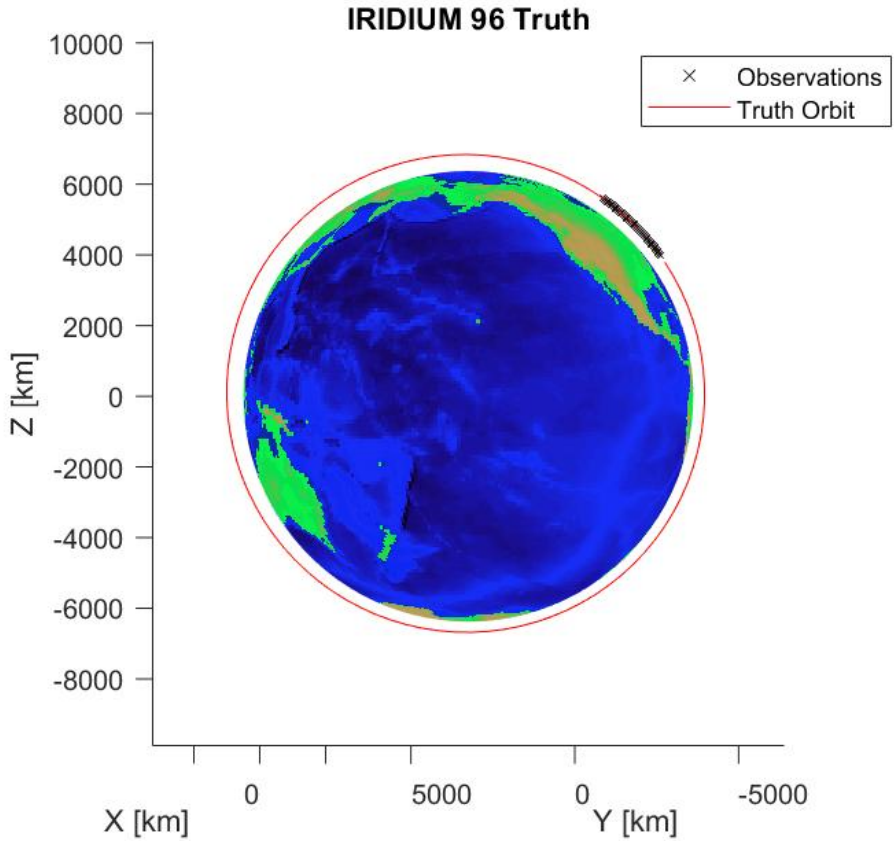

Fig. 5.46. IRIDIUM 96: Full truth orbit

Fig. 5.48 shows the RSW errors for the error-free least squares solution compare to the truth orbit. With perfect measurements, the least squares method has maximum errors value of 6.5 mm in the radial direction, 31.4 mm in the along-track direction, and 0.3 mm in the cross-track direction. This serves as a baseline level for RSW errors in LEO strictly from the least squares method. The trends indicate that the least squares solution has a smaller orbital radius and as a result, the NLUMVE remains ahead of the truth orbit seen in the along-track component of the Fig. 5.48. Although the velocity of this LEO satellite is much higher than before, at approximately 7.6874 km/s, these error values are lower than even the MEO and GEO examples because the observations are made in a smaller window with higher frequency. However, as

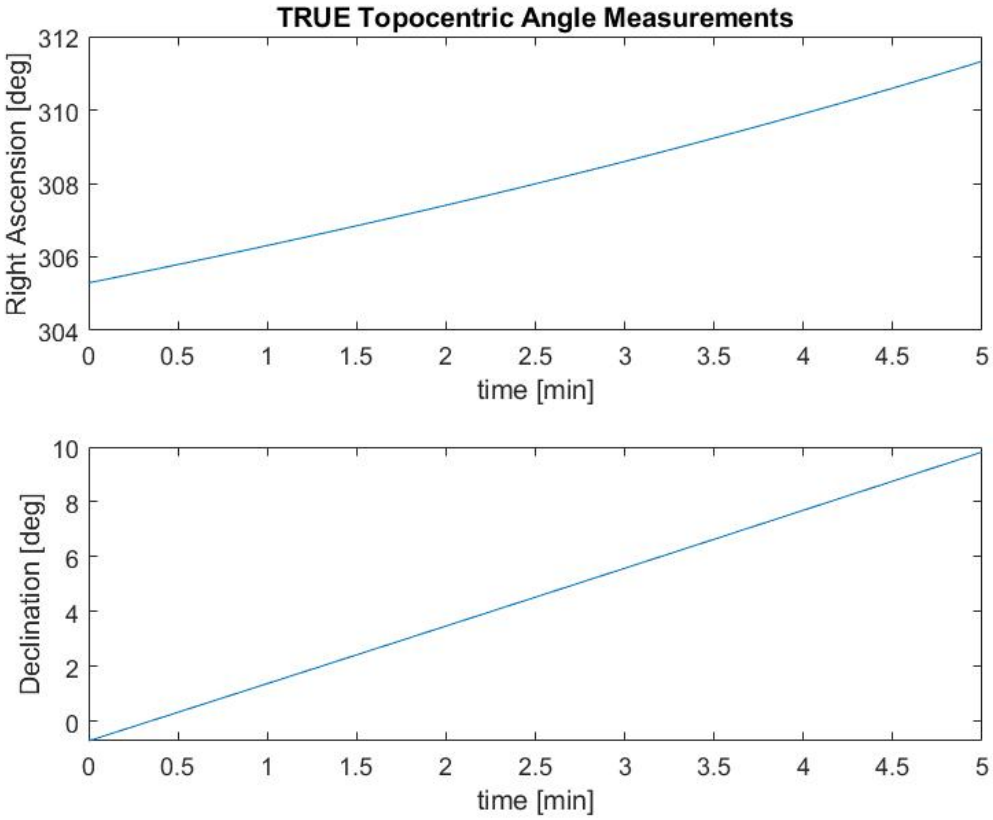

Fig. 5.47. IRIDIUM 96: True, error-free angle measurements

errors from chapter 4 are introduced into the scenario, these error values are expected to increase in a more exaggerated fashion due to the high velocity.

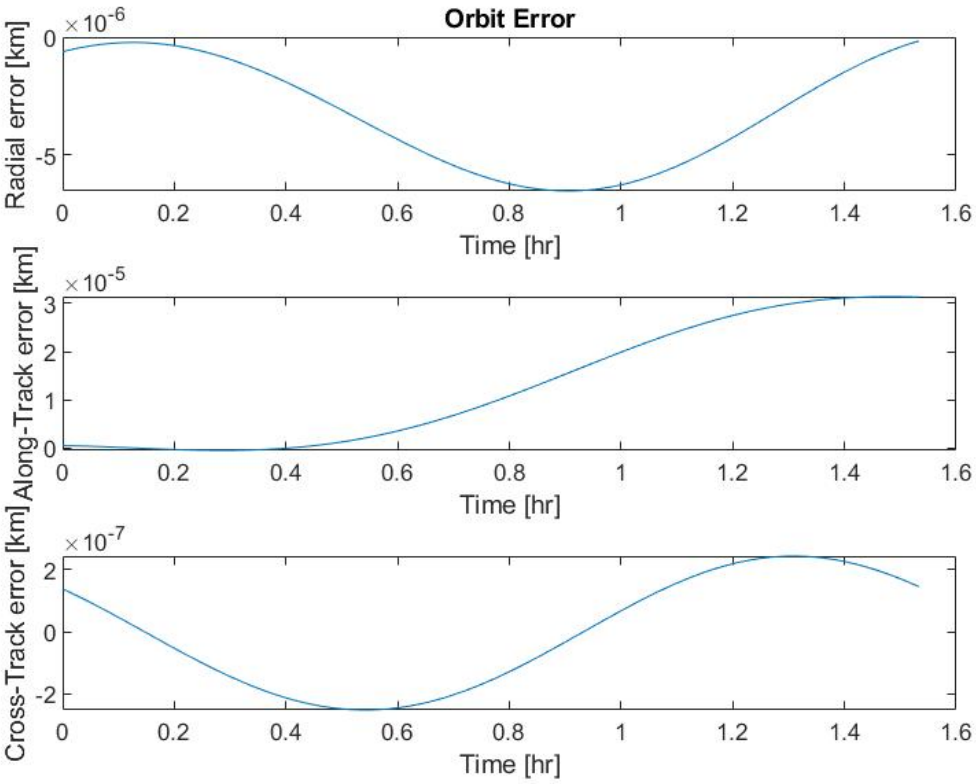

Fig. 5.48. IRIDIUM 96: RSW orbital errors, NLUMVE vs truth with no modeled errors

5.4.1 LEO Timing Error

Timing error is introduced in the LEO scenario in order to demonstrate the impact of poor timing in relation to optical measurements. The LEO scenario is run using a range of values for the $3\sigma_t$ timing error, 0.001 s to 1.000 s.

$$\Delta t_{error} \sim N(0, \sigma_t^2)[seconds] \tag{5.19}$$

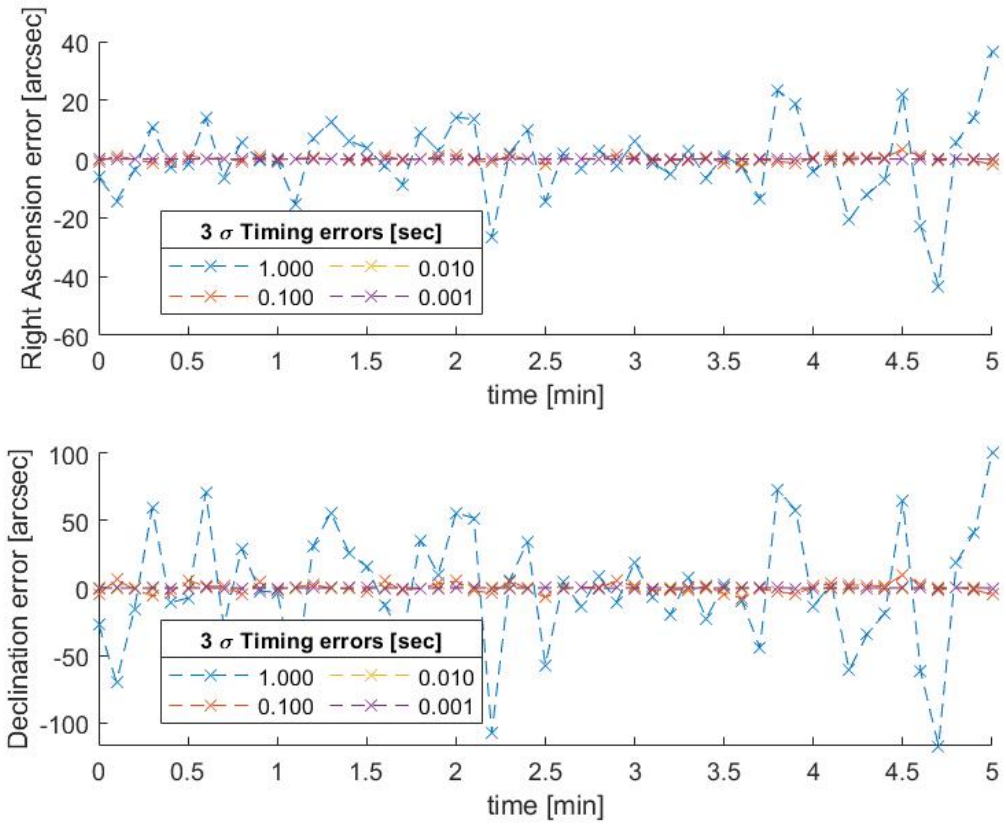

Fig. 5.49. IRIDIUM 96: Observation vs NLUMVE angle error distributions for unbiased timing error

Even with very small timing error introduced, the resultant RSW errors for the LEO scenario increase dramatically, considering the smaller size of the orbit. However,

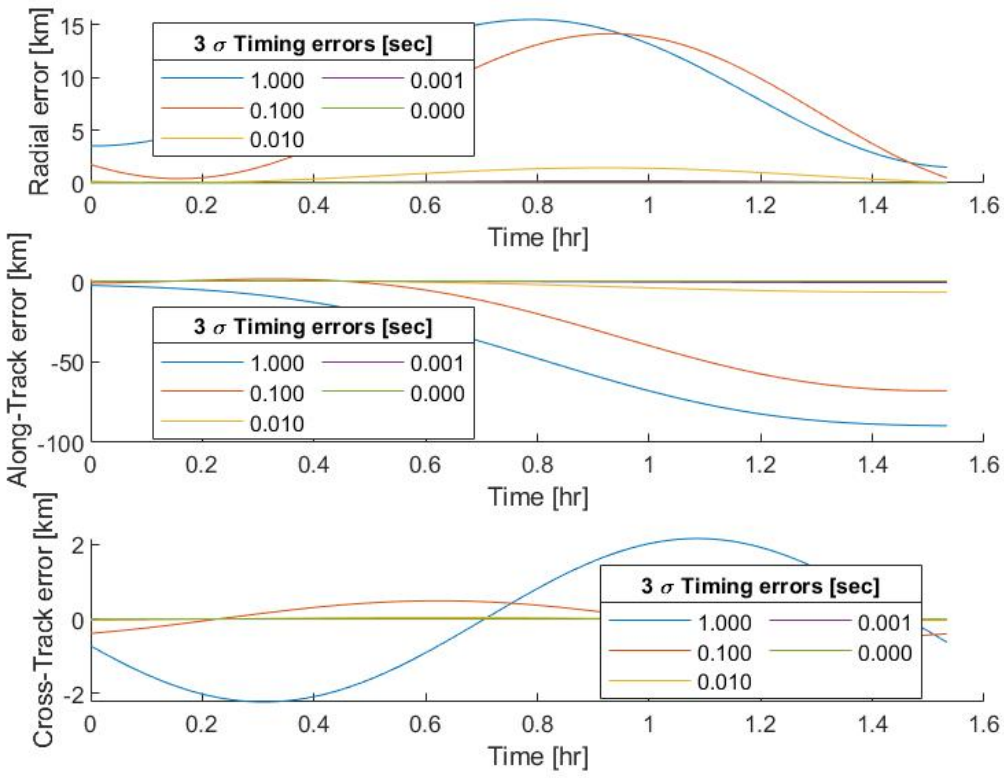

Fig. 5.50. IRIDIUM 96: RSW orbital errors for timing error

Fig. 5.49 shows randomly distributed angle errors, and only 2 of the 4 scenarios have relatively low p-values, seen in Table 5.19. It can be concluded that Shapiro-Wilk test not be recommended for LEO and small data sets of approximately 50 observations or less. The least squares method does not converge well when erroneous measurements are used to attempt orbit improvement. This is acceptable, noting that optical sensors are not typically tasked to track LEO objects since radar is more apt for the lower orbital regions.

Table 5.19.
IRIDIUM 96: Shapiro-Wilk test results with RSW orbital errors for unbiased timing error scenarios

IRIDIUM 96	**Measurements vs. NLUMVE angles SW test**				**NLUMVE vs. Truth Orbit** (max errors)		
3σ Timing Error	W α	α P-val	W δ	δ P-val	Radial Error	Along-Track Error	Cross-Track Error
0.000 s	NaN	NaN	NaN	NaN	0.0065 m	0.0314 m	0.0003 m
0.001 s	0.9799	0.5333	0.9673	0.1710	183.27 m	863.87 m	6.9920 m
0.010 s	0.9793	0.5090	0.9677	0.1767	1433.7 m	6858.0 m	43.858 m
0.100 s	0.9604	0.0805	0.9869	0.8417	14,155 m	68,026 m	490.05 m
1.000 s	0.9598	0.0767	0.9823	0.5507	15,499 m	89,688 m	2,227.8 m

5.4.2 LEO Timing Bias

Timing bias is introduced in the LEO scenario in order to demonstrate the impact of poor timing in relation to optical measurements. The LEO scenario is run using a range of values for the β_t timing bias, 0.001 s to 1.000 s, and a small 3σ timing error of 0.001 s.

$$\Delta t_{error} \sim N(\beta_t, (.001/3)^2)[seconds] \tag{5.20}$$

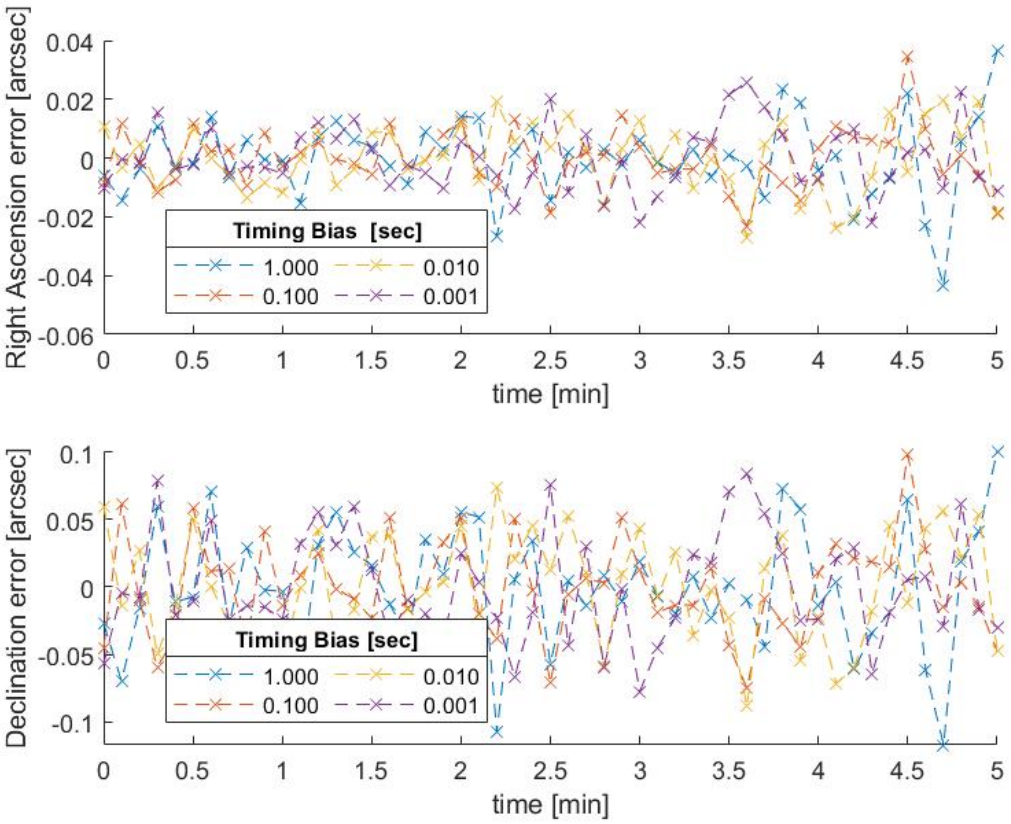

Fig. 5.51. IRIDIUM 96: Observation vs NLUMVE angle error distributions for biased timing error

The angles in Fig. 5.51 show similar random trends as the unbiased case but with smaller magnitudes, which is in agreement with the smaller 3σ timing error of 0.001 s. Since this LEO scenario has a shorter observation window, the least squares method does a relatively good job of maintaining the correct plane of motion, but the radial and along-track component errors remain quite large, seen in Fig. 5.52.In these examples, the effect of timing bias on a higher velocity satellite in LEO is not as predictable as the other scenarios with timing bias. Timing bias of 1.000 second has lower error values than the 0.001 second timing bias scenario.

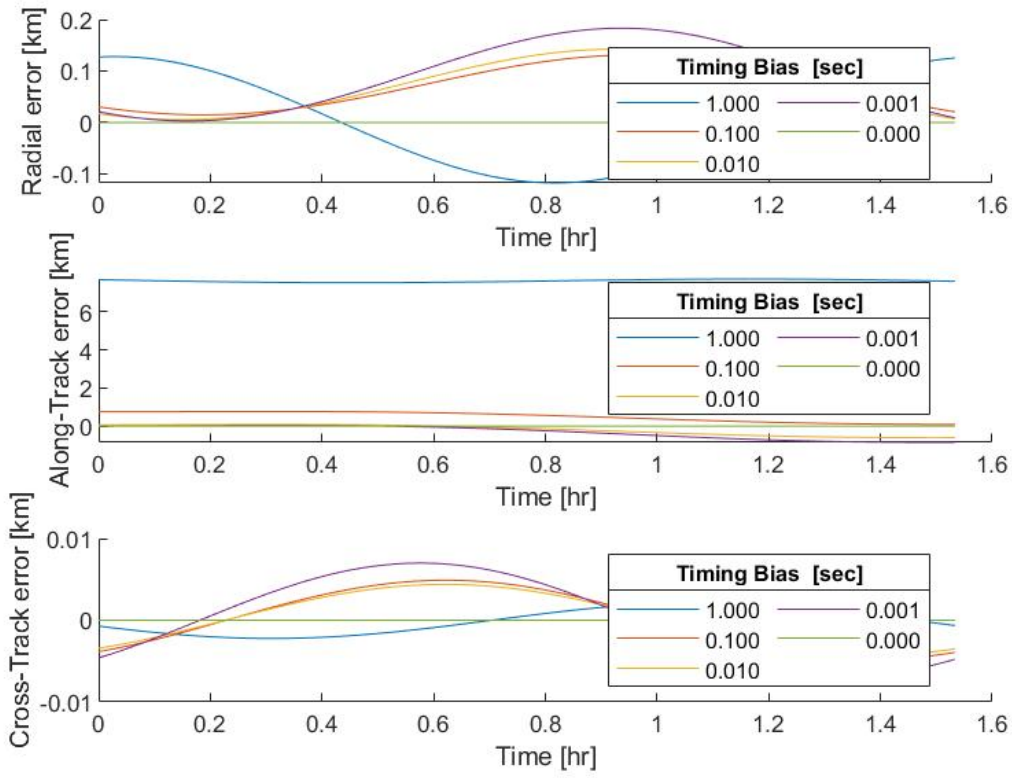

Fig. 5.52. IRIDIUM 96: RSW orbital errors, NLUMVE with biased timing error vs truth

Table 5.20.
IRIDIUM 96: Shapiro-Wilk test results with RSW orbital errors for biased timing error scenarios

IRIDIUM 96	Measurements vs. NLUMVE angles SW test				NLUMVE vs. Truth Orbit (max errors)		
Timing Bias	W α	α P-val	W δ	δ P-val	Radial Error	Along-Track Error	Cross-Track Error
0.000 s	NaN	NaN	NaN	NaN	183.27 m	863.87 m	6.9920 m
0.001 s	0.9799	0.5333	0.9673	0.1710	183.16 m	856.16 m	6.9920 m
0.010 s	0.9793	0.5090	0.9677	0.1767	142.25 m	608.57 m	4.3853 m
0.100 s	0.9604	0.0805	0.9869	0.8417	131.00 m	768.28 m	4.8956 m
1.000 s	0.9598	0.0767	0.9823	0.5507	128.02 m	7,719.1 m	2.2315 m

5.4.3 LEO Sidereal Timing Error

Sidereal timing error is introduced in the LEO scenario, which is run using a range of values for the $3\sigma_t$ sidereal timing error, 0.001 s to 1.000 s:

$$\Delta t_{error} \sim N(0, \sigma_t^2)[seconds] \tag{5.21}$$

In Fig. 5.53, there are some apparent problems in the declination error distributions. Table 5.21 confirms that for these scenarios, that the declination distributions are non-normal with p-values less than 0.15. However, for the worst case scenario, the distribution testing is unable to detect any problem. This is likely due to the high levels of error resulting from using erroneous measurements during the least squares method. Fig. 5.54 shows large error values again, which is expected because the LEO satellite is moving at a much higher velocity. As states before, for closer orbit regions, the Shapiro-Wilk test is less effective, but is still able to detect poor observations sets with medium levels of error in LEO.

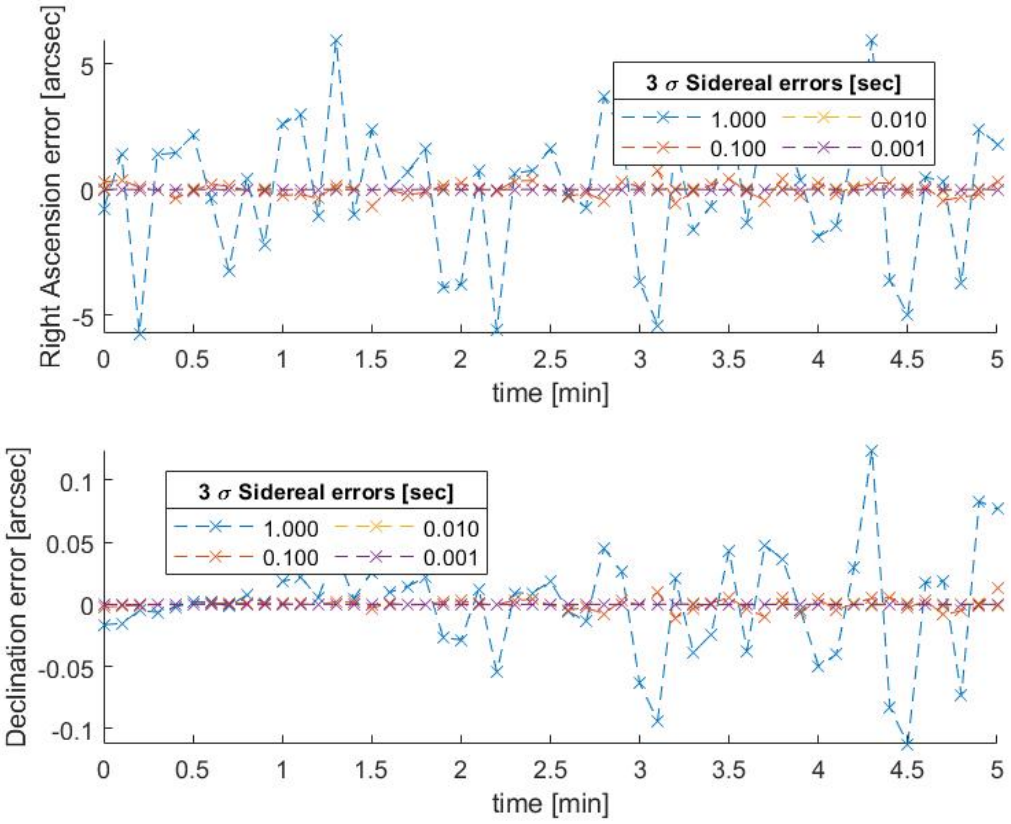

Fig. 5.53. IRIDIUM 96: Observation vs NLUMVE angle error distributions for unbiased sidereal timing error

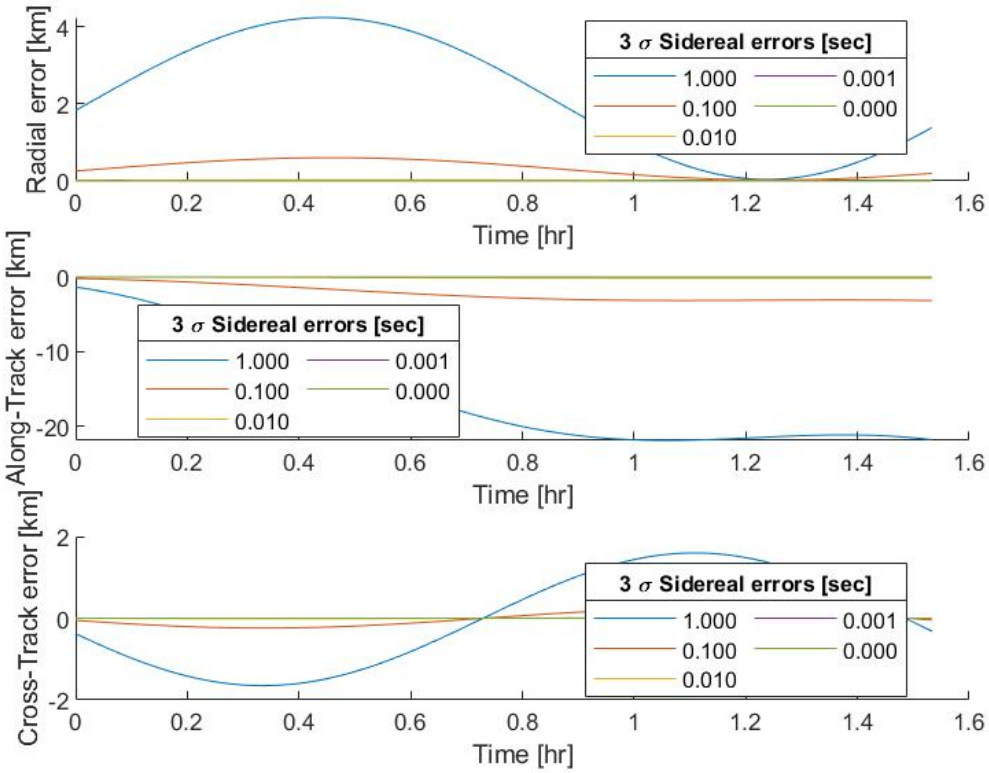

Fig. 5.54. IRIDIUM 96: RSW orbital errors, NLUMVE with modeled unbiased sidereal timing error vs truth

Table 5.21.
IRIDIUM 96: Shapiro-Wilk test results with RSW orbital errors for unbiased sidereal timing error scenarios

IRIDIUM 96	**Measurements vs. NLUMVE angles SW test**				**NLUMVE vs. Truth Orbit** (max errors)		
3σ Sidereal Error	W α	α P-val	W δ	δ P-val	Radial Error	Along-Track Error	Cross-Track Error
0.000 s	NaN	NaN	NaN	NaN	0.0065 m	0.0314 m	0.0003 m
0.001 s	0.9707	0.2374	0.9649	0.1205	4.5090 m	24.300 m	2.0146 m
0.010 s	0.9904	0.9517	0.9462	0.0238	28.850 m	165.90 m	13.874 m
0.100 s	0.9906	0.9573	0.9583	0.0669	600.95 m	3,154.8 m	240.32 m
1.000 s	0.9685	0.1923	0.9584	0.6750	4,233.1 m	21,856 m	1,650.6 m

5.4.4 LEO Sidereal Timing Bias

Sidereal timing bias is introduced in the LEO scenario. It is run using a range of values for the β_t timing bias, 0.001 s to 1.000 s, and a small 3σ timing error of 0.001 s.

$$\Delta t_{error} \sim N(\beta_t, (.001/3)^2)[seconds] \tag{5.22}$$

Fig. 5.55 shows that for the worst-case scenario, the declination error distribution experiences very pronounced nonlinear transformation. However, in Table 5.22 the distribution testing only marks that scenario with a p-value of 0.2065. It is important to note the limitations of distribution testing. It does not factor in the relationship to time. It only looks at the distribution as a whole. For time related testing, a parametric regression or parametric distribution test is required. Both require much more extensive setup and a priori information. Then, it can be concluded again that distribution tests not be recommended for LEO.

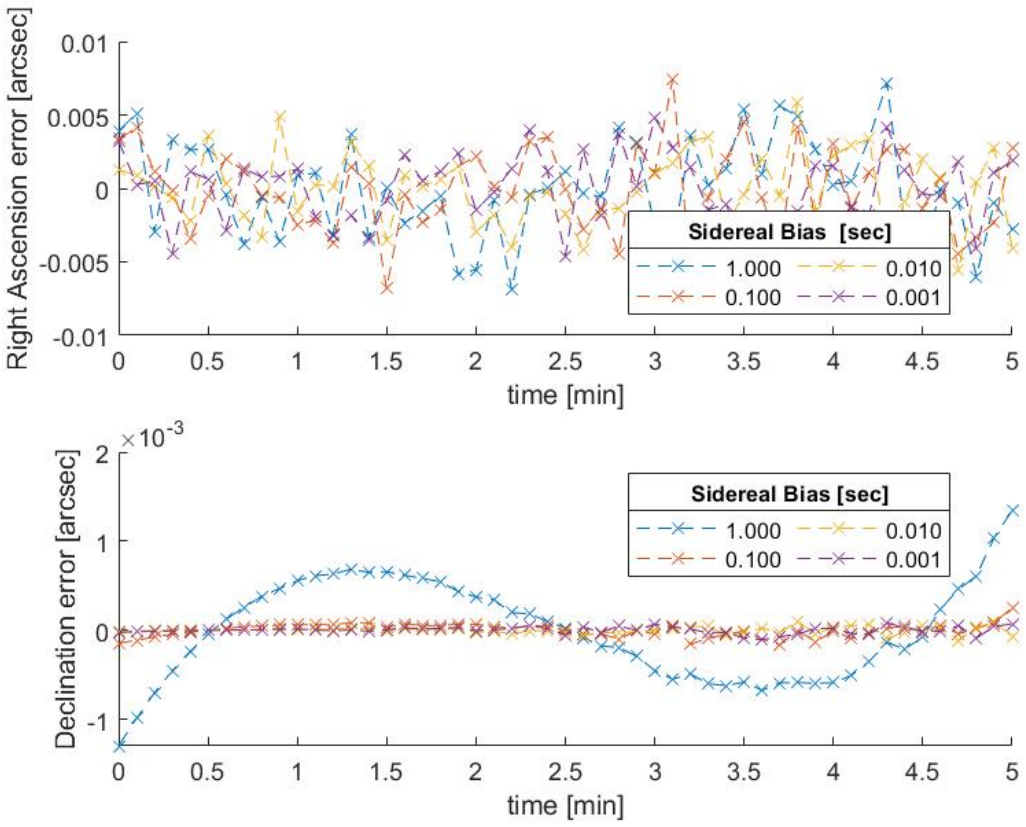

Fig. 5.55. IRIDIUM 96: Observation vs NLUMVE angle error distributions for biased sidereal timing error

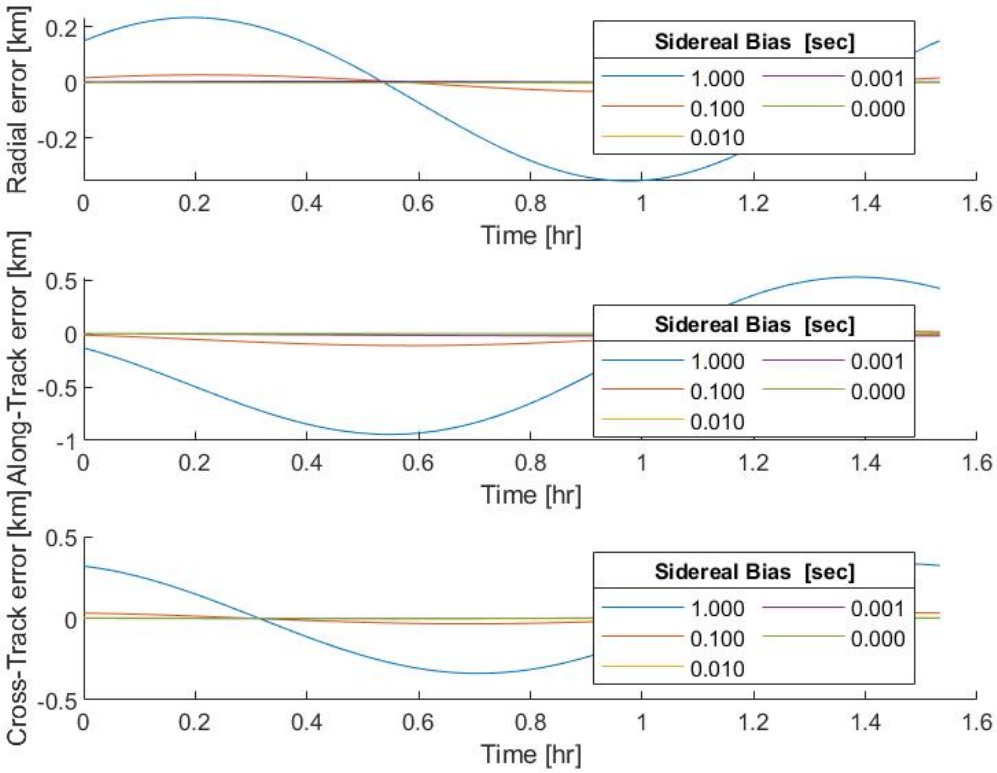

Fig. 5.56. IRIDIUM 96: RSW orbital errors, NLUMVE with modeled biased sidereal timing error vs truth

Table 5.22.
IRIDIUM 96: Shapiro-Wilk test results with RSW orbital errors for biased sidereal timing error scenarios

IRIDIUM 96	Measurements vs. NLUMVE angles SW test				NLUMVE vs. Truth Orbit (max errors)		
Sidereal Bias	W α	α P-val	W δ	δ P-val	Radial Error	Along-Track Error	Cross-Track Error
0.000 s	NaN	NaN	NaN	NaN	4.5090 m	24.300 m	2.0146 m
0.001 s	0.9708	0.2376	0.9653	0.1254	4.5878 m	23.859 m	2.0868 m
0.010 s	0.9903	0.9505	0.9575	0.0626	4.4896 m	19.775 m	3.8724 m
0.100 s	0.9915	0.9734	0.9320	0.0077	33.638 m	113.77 m	34.084 m
1.000 s	0.9836	0.6993	0.9693	0.2065	353.02 m	944.05 m	337.77 m

5.4.5 LEO Angle Measurement Error

Angle Measurement error is introduced in the LEO scenario and is run using a range of values for the $3\sigma_{ang}$ angle measurement error, 0.1 arcseconds to 100.0 arcsecs for both right ascension and declination:

$$\Delta ang_{error} \sim N(0, \sigma_{ang}^2)[arcseconds] \tag{5.23}$$

In Fig. 5.57, the angle error distributions show normally distributed errors, which is similar with the results of the GEO, HEO, LEO scenarios. The results in Table 5.23 confirms that for most of the data sets. No cases tests positive for the right ascension or declination observations. The RSW errors in Fig. 5.58 show the error values as high as 257 km, which is extreme for a LEO object with semi-major axis of 6,775 km. The distribution was unable to detect these egregious errors. Again, it is not recommended that distribution testing be used for detecting unbiased measurement error especially in LEO.

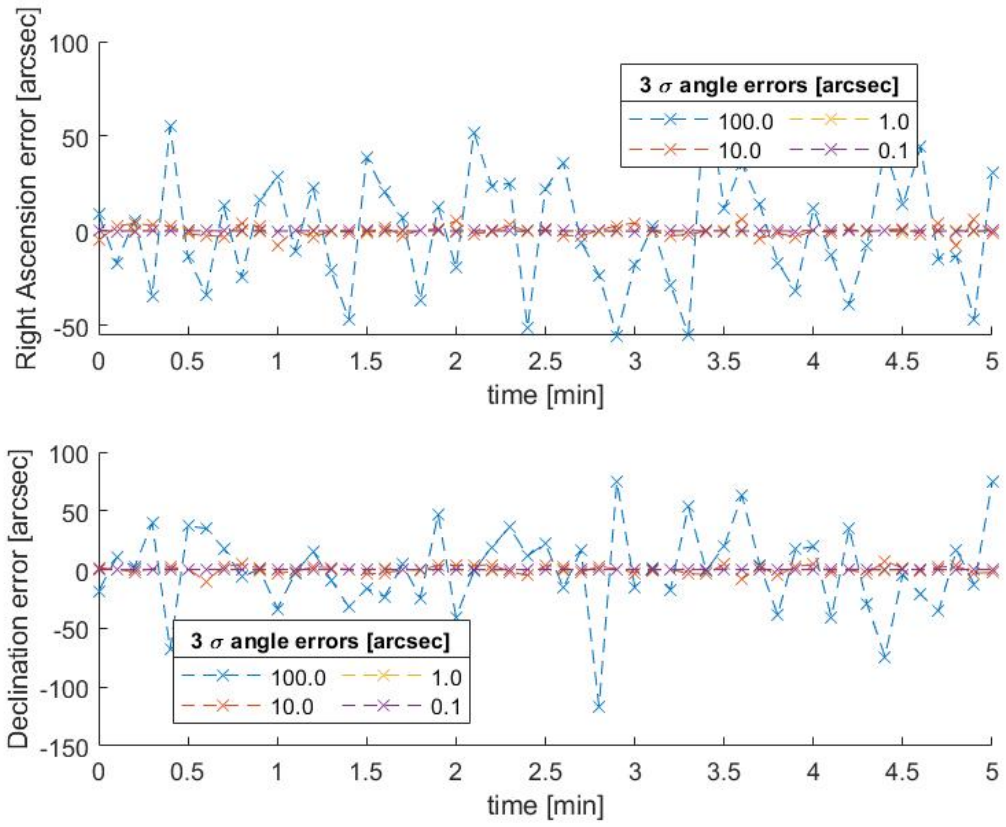

Fig. 5.57. IRIDIUM 96: Observation vs NLUMVE angle error distributions for unbiased angle measurement error

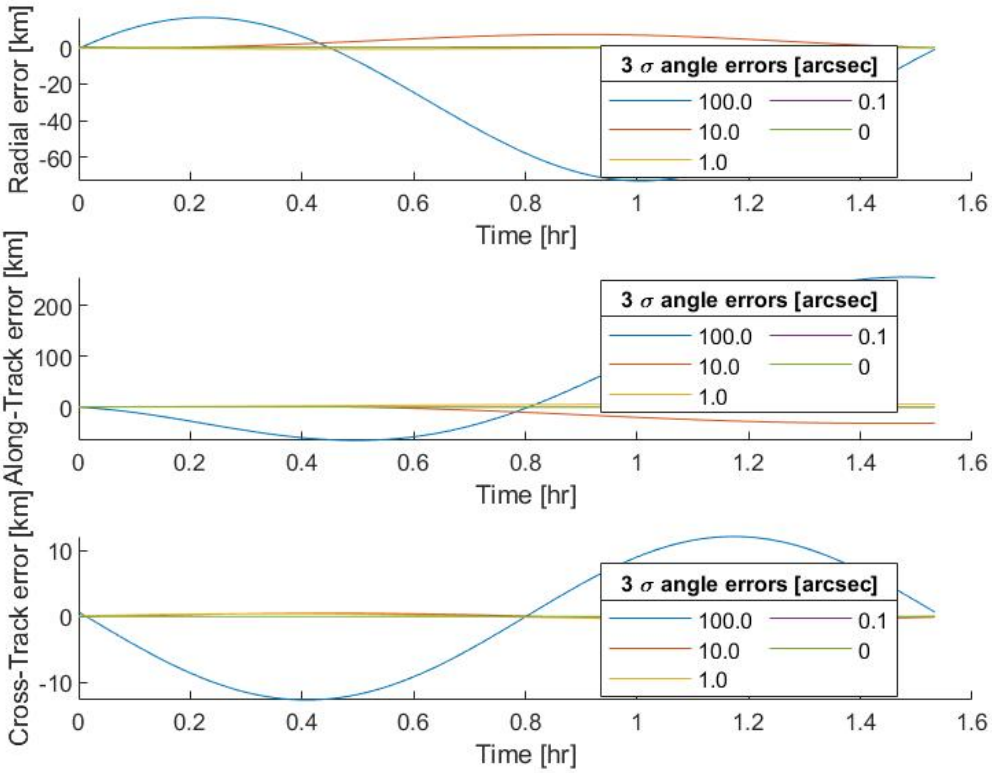

Fig. 5.58. IRIDIUM 96: RSW orbital errors, NLUMVE with modeled unbiased angle measurement error vs truth

Table 5.23.
IRIDIUM 96: Shapiro-Wilk test results with RSW orbital errors for unbiased angle measurement error scenarios

IRIDIUM 96	**Measurements vs. NLUMVE angles SW test**				**NLUMVE vs. Truth Orbit** (max errors)		
3σ Angle Error	W α	α P-val	W δ	δ P-val	Radial Error	Along-Track Error	Cross-Track Error
0 arcsec	NaN	NaN	NaN	NaN	0.0065 m	0.0314 m	0.0003 m
0.1 arcsec	0.9858	0.7964	0.9763	0.3941	132.60 m	668.78 m	4.1940 m
1.0 arcsec	0.9625	0.0970	0.9757	0.3757	1,002.3 m	5,471.2 m	415.39 m
10.0 arcsec	0.9790	0.4215	0.9696	0.1838	7,015.3 m	32,179 m	494.02 m
100.0 arcsec	0.9807	0.5674	0.9675	0.1521	72,825 m	256,890 m	12,662 m

5.4.6 LEO Angle Measurement Bias

Angle measurement bias is introduced in the LEO scenario and is run using a range of values for the β_{ang} angle bias, 0.1 arcsecs to 100.0 arcsecs, and a small 3σ angle error of 0.1 arcsecs.

$$\Delta ang_{error} \sim N(\beta_{ang}, (.001/3)^2)[arcseconds] \tag{5.24}$$

It can be seen in Fig. 5.59 that the angle error distributions appear random for all scenarios even with large errors exceeding 5 km in the RSW plots in Fig. 5.60. Table 5.24 shows that no cases test positive using a significance level of 0.05. These results indicate that distribution testing is not effective at detecting biased angle measurement error in LEO.

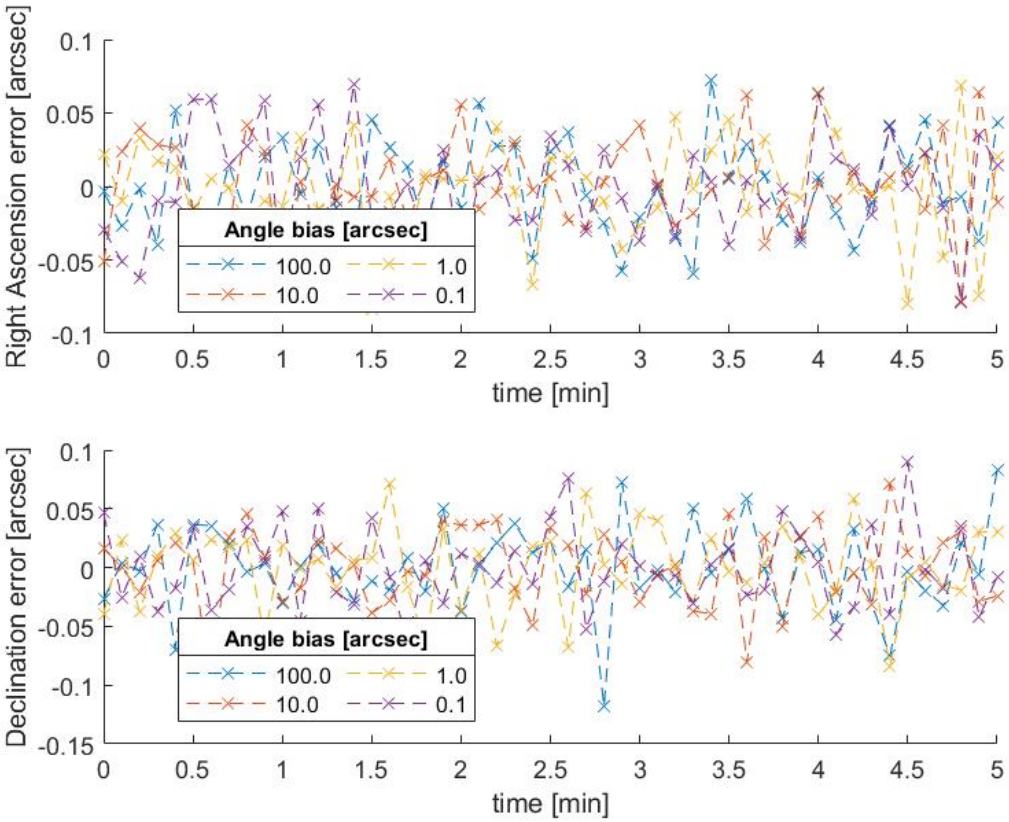

Fig. 5.59. IRIDIUM 96: Observation vs NLUMVE angle error distributions for biased angle measurement error

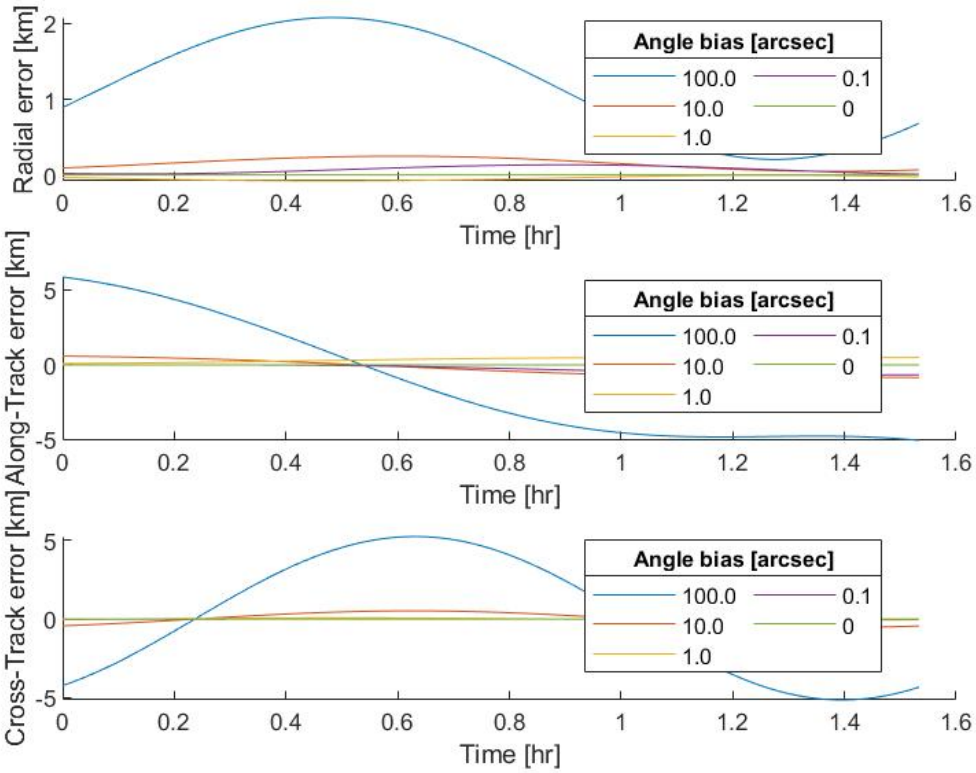

Fig. 5.60. IRIDIUM 96: RSW orbital errors, NLUMVE with modeled biased angle measurement error vs truth

Table 5.24.
IRIDIUM 96: Shapiro-Wilk test results with RSW orbital errors for biased angle measurement error scenarios

IRIDIUM 96	**Measurements vs. NLUMVE angles SW test**				**NLUMVE vs. Truth Orbit** (max errors)		
Angle Bias	W α	α P-val	W δ	δ P-val	Radial Error	Along-Track Error	Cross-Track Error
0 arcsec	NaN	NaN	NaN	NaN	132.60 m	668.78 m	4.1940 m
0.1 arcsec	0.9858	0.7964	0.9763	0.3940	133.76 m	673.05 m	9.9381 m
1.0 arcsec	0.9626	0.0978	0.9758	0.3778	79.332 m	494.23 m	79.365 m
10.0 arcsec	0.9800	0.4579	0.9694	0.1800	248.33 m	850.93 m	529.24 m
100.0 arcsec	0.9808	0.5729	0.9658	0.1313	2,081.5 m	5,863.1 m	5,250.1 m

5.5 Summary and Evaluation

Sections 5.1 through 5.4 simulated several scenarios with modeled errors. To summarize some of the resultant effects of the modeled errors, Table 5.25, Table 5.26, and Table 5.27 compile the results from the smallest error cases from each orbital region for comparison's sake. The upper left portions of the tables, outlined in red, show the GEO cases. The lower left portions of the tables, outlined in blue, show the HEO cases. The upper right portions of the tables, outlined in green, show the MEO cases. The lower right portions of the tables, outlined in purple, show the LEO cases.

5.5.1 Satellite Timing Error Comparison

Table 5.25.
Comparison of small satellite timing errors in each orbital region

INTELSAT 902 (GEO)	**NLUMVE vs. Truth Orbit** (max errors)		
Timing Error [sec]	Radial Error	Along-Track Error	Cross-Track Error
~N(0.000,0.000)	0.0071 m	0.0349 m	0.0003 m
~N(0.000,0.001)	64.992 m	280.10 m	4.2099 m
~N(0.001,0.001)	64.992 m	283.18 m	4.2099 m

NAVSTAR 39 (MEO)	**NLUMVE vs. Truth Orbit** (max errors)		
Timing Error [sec]	Radial Error	Along-Track Error	Cross-Track Error
~N(0.000,0.000)	0.1738 m	0.9134 m	0.0022 m
~N(0.000,0.001)	18.043 m	38.653 m	1.0455 m
~N(0.001,0.001)	18.035 m	42.424 m	1.0455 m

MOLNIYA 3-24 (HEO)	**NLUMVE vs. Truth Orbit** (max errors)		
Timing Error [sec]	Radial Error	Along-Track Error	Cross-Track Error
~N(0.000,0.000)	0.0048 m	0.0126 m	0.0004 m
~N(0.000,0.001)	37.706 m	89.824 m	3.9534 m
~N(0.001,0.001)	41.263 m	98.886 m	3.9534 m

IRIDIUM 96 (LEO)	**NLUMVE vs. Truth Orbit** (max errors)		
Timing Error [sec]	Radial Error	Along-Track Error	Cross-Track Error
~N(0.000,0.000)	0.0065 m	0.0314 m	0.0003 m
~N(0.000,0.001)	183.27 m	863.87 m	6.9920 m
~N(0.001,0.001)	183.16 m	856.16 m	6.9920 m

Table 5.25 shows three cases for each of the orbital regions: error-free (baseline), unbiased error with a 3σ bound of 1 millisecond, and 1 millisecond biased error with a 3σ bound of 1 millisecond. In all orbit regions, the along-track error in the RSW frame is the largest error since that is the primary direction of motion. For LEO, since the uncertainty is modeled using a zero-mean random variable, it is equally likely that the timing is too early or too late. At relative velocities of 7 to 8 km/s, 1 millisecond error can result in 7 to 8 meters of error for each observation. As a result, the least squares method has difficulty using the residuals to come to a solution. Yet when comparing GEO, HEO, and MEO, the larger resultant errors from the inclusion of satellite timing error are in GEO. Because of the farther distances for an object in GEO, small angle errors result in large arcs of the orbit. For this reason, GEO has the largest errors along-track due to satellite timing error, followed by HEO, then MEO. It is important for users and operators to realize this and prioritize minimizing satellite timing error and properly calibrating equipment when tracking objects that are far away.

5.5.2 Sidereal Timing Error Comparison

Table 5.26.
Comparison of small sidereal timing errors in each orbital region

INTELSAT 902 (GEO)	**NLUMVE vs. Truth Orbit** (max errors)			**NAVSTAR 39 (MEO)**	**NLUMVE vs. Truth Orbit** (max errors)		
Sidereal Error [sec]	Radial Error	Along-Track Error	Cross-Track Error	Sidereal Error [sec]	Radial Error	Along-Track Error	Cross-Track Error
~N(0.000,0.000)	0.0071 m	0.0349 m	0.0003 m	~N(0.000,0.000)	0.1738 m	0.9134 m	0.0022 m
~N(0.000,0.001)	20.195 m	108.17 m	0.2822 m	~N(0.000,0.001)	35.949 m	191.06 m	0.4682 m
~N(0.001,0.001)	20.546 m	110.56 m	0.2627 m	~N(0.001,0.001)	39.989 m	212.53 m	0.2644 m
MOLNIYA 3-24 (HEO)	**NLUMVE vs. Truth Orbit** (max errors)			**IRIDIUM 96 (LEO)**	**NLUMVE vs. Truth Orbit** (max errors)		
Sidereal Error [sec]	Radial Error	Along-Track Error	Cross-Track Error	Sidereal Error [sec]	Radial Error	Along-Track Error	Cross-Track Error
~N(0.000,0.000)	0.0048 m	0.0126 m	0.0004 m	~N(0.000,0.000)	0.0065 m	0.0314 m	0.0003 m
~N(0.000,0.001)	19.341 m	48.016 m	1.0966 m	~N(0.000,0.001)	4.5090 m	24.300 m	2.0146 m
~N(0.001,0.001)	19.748 m	49.097 m	1.1331 m	~N(0.001,0.001)	4.5878 m	23.859 m	2.0868 m

Following the outline in section 5.5.1, table 5.26 shows three different cases for each of the orbital regions: error-free (baseline), unbiased error with a 3σ bound of 1 millisecond, and 1 millisecond biased error with a 3σ bound of 1 millisecond. For the cases with sidereal timing error, again, the largest errors occur in the along-track orbital errors. However, the lowest errors seen in the table occur in the LEO regions. This is most likely a result of the 5-minute observation window in LEO covering a larger arc of the whole orbital period compared to the 50-minute window for the other regions. Still, this suggests that when tracking closer objects over longer arcs of their orbits, ground station timing error is not as critical as satellite timing error. For GEO, HEO, and MEO, the largest errors occur in MEO, where for smaller arcs, the closer objects experience larger orbital errors in the context of sidereal timing errors. In HEO, the errors are smaller due to the decelerating of the object as it approaches it slowest point of the orbit, apogee. Users and operators tracking objects in MEO should prioritize minimizing ground station timing errors over satellite timing error.

5.5.3 Angle Measurement Error Comparison

Table 5.27.
Comparison of small angle measurement errors in each orbital region

INTELSAT 902 (GEO)	**NLUMVE vs. Truth Orbit** (max errors)		
Angle Error [arcsec]	Radial Error	Along-Track Error	Cross-Track Error
~N(0.0,0.0)	0.0071 m	0.0349 m	0.0003 m
~N(0.0,0.1)	3,182.3 m	17,031 m	43.684 m
~N(0.1,0.1)	3,532.0 m	18,838 m	27.679 m

NAVSTAR 39 (MEO)	**NLUMVE vs. Truth Orbit** (max errors)		
Angle Error [arcsec]	Radial Error	Along-Track Error	Cross-Track Error
~N(0.0,0.0)	0.1738 m	0.9134 m	0.0022 m
~N(0.0,0.1)	2,614.3 m	14,028 m	28.715 m
~N(0.1,0.1)	2,461.6 m	13,070 m	42.749 m

MOLNIYA 3-24 (HEO)	**NLUMVE vs. Truth Orbit** (max errors)		
Angle Error [arcsec]	Radial Error	Along-Track Error	Cross-Track Error
~N(0.0,0.0)	0.0048 m	0.0126 m	0.0004 m
~N(0.0,0.1)	1,583.8 m	3,992.1 m	72.588 m
~N(0.1,0.1)	1,551.3 m	3,903.6 m	55.637 m

IRIDIUM 96 (LEO)	**NLUMVE vs. Truth Orbit** (max errors)		
Angle Error [arcsec]	Radial Error	Along-Track Error	Cross-Track Error
~N(0.0,0.0)	0.0065 m	0.0314 m	0.0003 m
~N(0.0,0.1)	132.60 m	668.78 m	4.1940 m
~N(0.1,0.1)	133.76 m	673.05 m	9.9381 m

Comparing the errors from Table 5.25 and Table 5.26 to the Angle Measurement errors in Table 5.27, it is apparent that angle measurement errors result in the highest orbital errors after orbit determination. The table shows three cases: error-free (baseline), unbiased error with a 3σ bound of 0.1 arcsecond, and 0.1 arcsecond biased error with a 3σ bound of 0.1 arcsecond. In all orbital regions, it is most important to minimize errors associated with the angle measurements. In these cases, even with small errors of 0.1 arcsecond, which is better than currently available equipment, the errors are very high. For GEO, the highest error is near 19 km, which is unacceptable for collision avoidance. This emphasizes that the most important factor in minimizing object state uncertainty is in the angle measurements. Users and operators should prioritize angle measurements as the most important source of potential error in all orbital regions.

5.6 Combined Error Scenarios

For more real-world applicability, the models used previously are combined to varying degrees to mimic low quality, good quality, and best quality sensors available now. An ideal, error-free sensor is included for reference. The scenarios use the GPS satellite from the MEO simulations from section 5.3, and the observer location remains at Purdue University. The sensors used are outlined with their respective error levels in Table 5.28. For these scenarios, the 50-minute observation window is reused, but measurements are recorded every 2 seconds for a total of 1501 observations of right ascension and declination. More observations are included to study how the distribution testing performs with larger datasets.

Table 5.28.
Description of error levels for sensors used in the combined error scenarios

	3σ Error Ranges, unbiased (μ=0)			
Sensor Quality	Timing	Sidereal	α	δ
Ideal	0	0	0	0
Best Quality	0.0001 s	0.0001 s	0.1 arcsec	0.1 arcsec
Good Quality	0.0001 s	0.0001 s	2.0 arcsec	2.0 arcsec
Low Quality	0.0010 s	0.0010 s	5.0 arcsec	5.0 arcsec

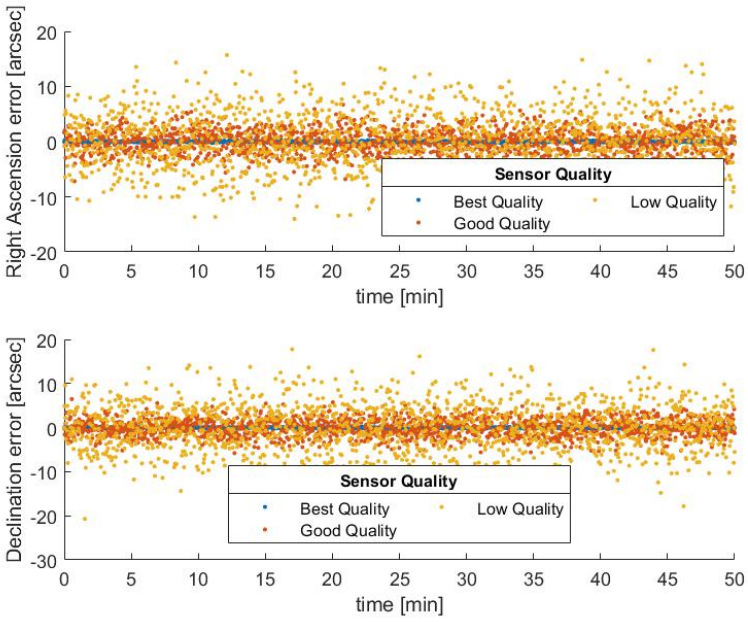

Fig. 5.61. Observation vs NLUMVE angle error distribution for all sensors used in the combined error scenarios

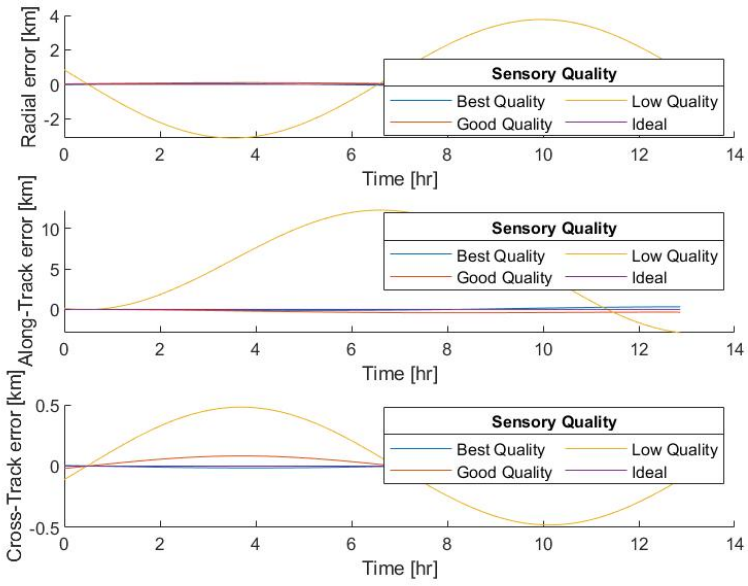

Fig. 5.62. RSW orbital errors, NLUMVE with combined error scenarios vs truth

Fig. 5.61 and Fig. 5.62 show that the low quality sensor has the largest errors in both the angle measurements as well as the RSW orbital errors. This agrees with the result in Table 5.29. The Shapiro-Wilk test is able to detect the one low quality sensor, even though many observations are used. This is very applicable as the test can determine if a sensor is of low quality with only an observation data set and no outside information.

Table 5.29.
Shapiro-Wilk test results and RSW Orbital errors for sensors used in the combined error scenarios

NAVSTAR 39	**Measurements vs. NLUMVE angles SW test**				**NLUMVE vs. Truth Orbit** (max errors)		
Sensor Quality	W α	α P-val	W δ	δ P-val	Radial Error	Along-Track Error	Cross-Track Error
Ideal	NaN	NaN	NaN	NaN	0.0179 m	0.0821 m	0.0013 m
Best Quality	0.9992	0.8029	0.9991	0.7203	102.32 m	327.06 m	14.576 m
Good Quality	0.9990	0.5439	0.9990	0.5518	93.561 m	416 .95 m	83.009 m
Low Quality	0.9993	0.8557	0.9979	0.0493	3,761.9 m	12,285 m	481.24 m

5.7 Two-Sensor Scenario

As an additional scenario, a two-sensor application is simulated in order to study the effects on orbit determination when using measurements from one good sensor and one bad sensor. In the context of sharing observation data, this is a realistic scenario, where amateur measurements may be used to update or improve an existing orbit computation. This setup uses the same geosynchronous INTELSAT 902 from section 5.1 with an observer at Purdue University, West Lafayette, IN, just as before. However, this scenario will include observations taken at the Purdue Optical Ground Station (POGS) in New Mexico. Measurements are first taken every 30 seconds at Purdue during a 50-minute observation window, and then tracking responsibilities are handed off to POGS, where measurements are recorded every 30 seconds for an additional 50-minute window. This results in 101 observations of topocentric right ascension and declination at each location, for a total of 202 observations. All observations are used in the least squares orbit determination method. To study the

effects of using one good sensor and one bad sensor, the observer at Purdue University, will have fixed timing, sidereal timing, and measurement error, and POGS will vary its error levels from low to high for four separate cases, outlined in Table 5.30.

Table 5.30.
Description of error levels in cases used for two-sensor scenario

	Purdue University, West Lafayette, IN				Purdue Optical Ground Station, NM			
	3σ Error Ranges, unbiased (μ=0)				3σ Error Ranges, unbiased (μ=0)			
Case #	Timing	Sidereal	α	δ	Timing	Sidereal	α	δ
Case 0	0.001 s	0.001 s	3.0 arcsec	3.0 arcsec	0.001 s	0.001 s	3.0 arcsec	3.0 arcsec
Case 1	0.001 s	0.001 s	3.0 arcsec	3.0 arcsec	0.010 s	0.010 s	3.0 arcsec	3.0 arcsec
Case 2	0.001 s	0.001 s	3.0 arcsec	3.0 arcsec	0.100 s	0.100 s	3.0 arcsec	3.0 arcsec
Case 3	0.001 s	0.001 s	3.0 arcsec	3.0 arcsec	1.000 s	1.000 s	3.0 arcsec	3.0 arcsec

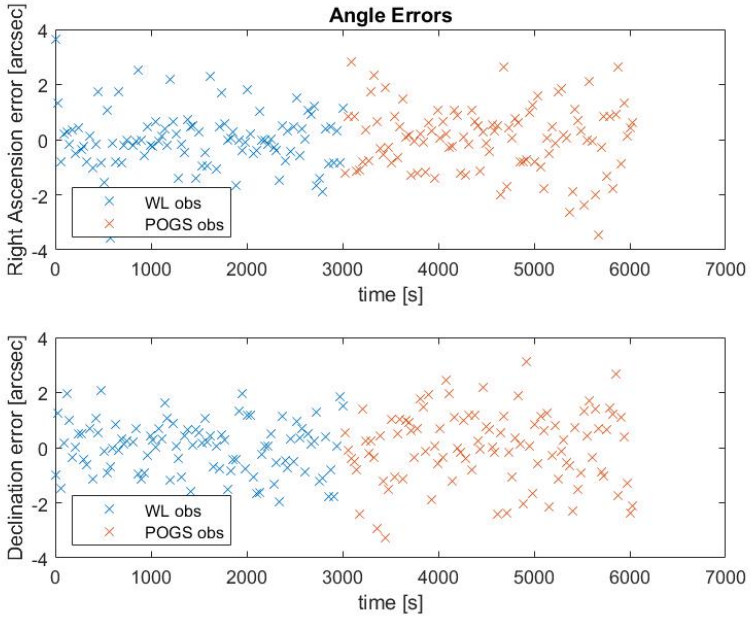

Fig. 5.63. Case 0: Observation vs NLUMVE angle error distributions for the two-sensor scenario

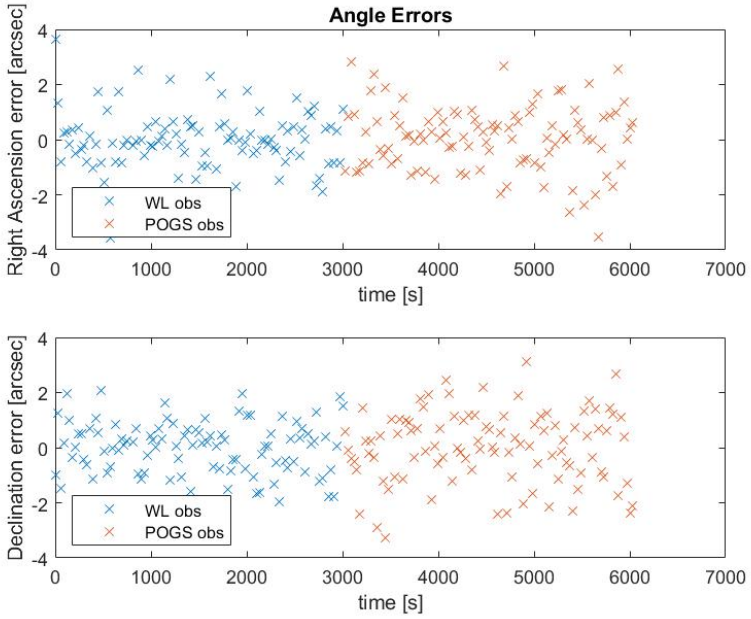

Fig. 5.64. Case 1: Observation vs NLUMVE angle error distributions for the two-sensor scenario

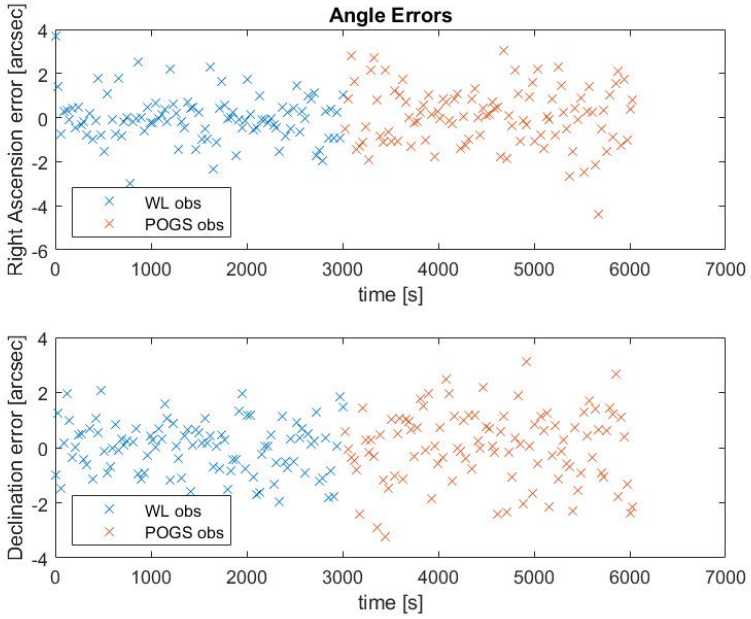

Fig. 5.65. Case 2: Observation vs NLUMVE angle error distributions for the two-sensor scenario

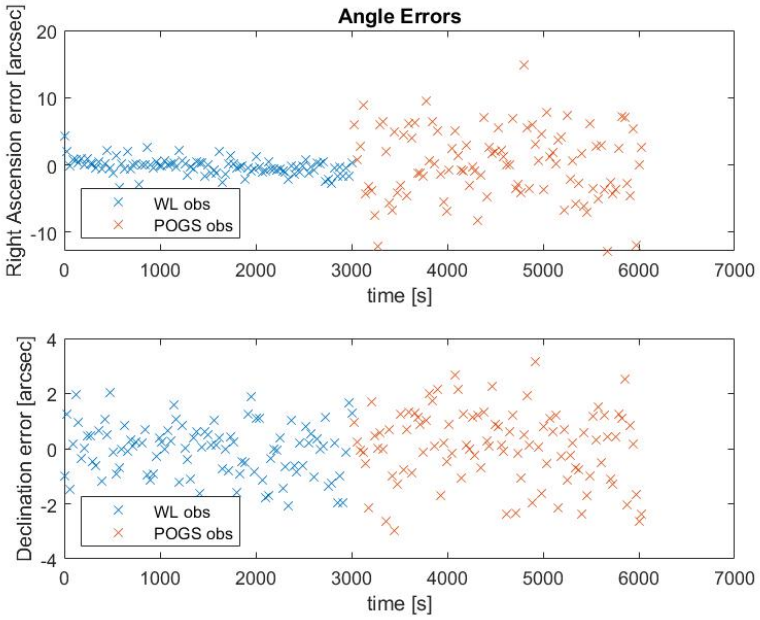

Fig. 5.66. Case 3: Observation vs NLUMVE angle error distributions for the two-sensor scenario

Table 5.31.
Shapiro-Wilk Test results and R and V errors for the two-sensor scenarios

INTELSAT 902	Measurements vs. NLUMVE angles SW test				NLUMVE vs. Truth Orbit at Initial Time	
Case #	W α	α P-val	W δ	δ P-val	Rmag Error	Vmag Error
Case 0	0.9440	0.2416	0.9938	0.5654	907.9 m	0.0806 m/s
Case 1	0.9857	0.0382	0.9938	0.5620	857.2 m	0.0758 m/s
Case 2	0.9861	0.0433	0.9936	0.5273	350.7 m	0.0277 m/s
Case 3	0.9856	0.0394	0.9979	0.0493	4,723.3 m	0.4554 m/s

The unbiased timing and sidereal errors are mostly contained in right ascension errors. This is visibly apparent for cases 2 and 3. For case 1, it is difficult to tell there is much difference between the distributions. However, the Shapiro-Wilk test identifies problems in the error distributions of cases 1, 2, and 3. Case 0 uses the same distribution shape for both the West Lafayette and POGS locations. Table 5.31 shows the test results as well as the error in R and V magnitudes.

When combining the measurements of the same object using two sensors of varying quality, distribution testing is able to detect problems with incoming observation data using only observations already on hand. This is extremely useful for real-world application as it does require any outside information. The testing reveals whether or not an operator should include or exclude new observations.

5.8 Full Satellite Catalog Scenario

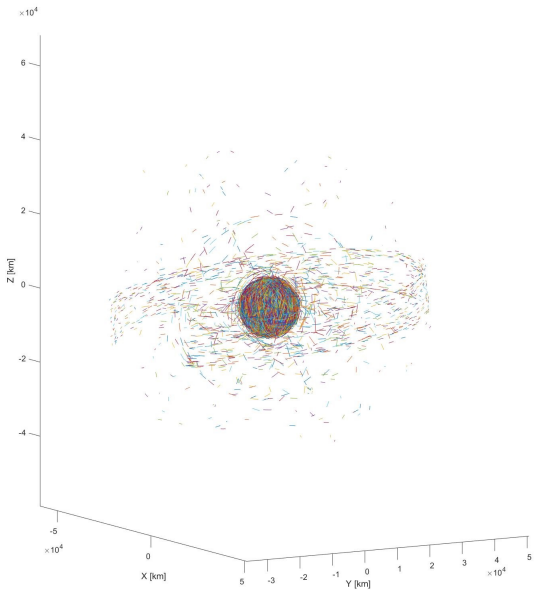

Fig. 5.67. Full Satellite Catalog Propagated for 15 minutes with unbiased timing error and unbiased sidereal timing error

To demonstrate the ease of use and wide applicability of the distribution testing, the entire satellite catalog from 01 September 2019 from space-track.org is propagated for 15 minutes, with observations of both right ascension and declination recorded every 9 seconds, all including small levels of unbiased timing error and unbiased sidereal timing error. No angle measurement error is included as it is evident from the previous sections that the distribution testing is largely ineffective in detecting measurement angle errors. Fig. 5.67 shows the 15-minute orbit arcs for 18,155 objects. The propagated orbit arcs are used to extract the erroneous right ascension and declination measurements, and for each object, orbit determination is completed just as before. The least squares estimate is compared to the erroneous angle measurements to create the angle error distributions, and each of these distributions are tested using

the Shapiro-Wilk test with a significance level of 0.05. The results of the distribution testing is shown in Table 5.32. The distribution testing detected 15,371 individual objects of 18,155 total objects propagated with timing and sidereal timing errors. A successful detection rate of 84.67% shows there is potential in using distribution testing as a filtering method when sharing observation data.

Table 5.32.
Shapiro-Wilk Test results for the full satellite catalog propagation

3σ Error Ranges, unbiased (μ=0)				**Observation Sets Detected with SW Test (α=0.05)**			
Timing	Sidereal	α	δ	α	δ	both α and δ	Total Detected
0.001 s	0.001 s	0.0 arcsec	0.0 arcsec	9,010	14,325	7,964	15,371 (84.67%)
Full Satellite Catalog from 01 Sep 2019 obtained from space-track.org includes 18,155 tracked objects							

6. SUMMARY

With rising interests in improved space situational awareness in commercial, private, and military contexts, the benefits of sharing observations around world are clear. More observations can help track objects and maintain the safe use of near-Earth space. Unfortunately, there is no set protocol for describing error uncertainties for observation datasets, and it can difficult without a priori knowledge to determine the quality or validity of an incoming dataset. Variability in environment, equipment, and operational procedures all contribute to some degree of uncertainty in measurements. Likewise, when these measurements are used for orbit determination, the computed orbit also has uncertainties in the position and velocity state.

One of the goals of this thesis is to model errors associated with optical observations in a simple yet effective manner in order to determine the ultimate effect they may have on orbit computations. The second goal is to use statistical distribution tests to determine if data sets with poorly made observations can be detected using only the incoming dataset. The first goal gives users and operators a reference guide of how different levels of errors affect object position uncertainty and which errors contribute to the largest deviations from an object's true position. The second goal provides users and operators with an additional tool to determine if an incoming data set should be used to update an object's orbit. This second goal is especially important if there is to be a collaborative effort in maintaining the safe use of near-Earth space.

6.1 Conclusions

This research achieves its first goal by modeling potential errors as random variables. By studying and modeling varying degrees of satellite timing error, ground

station timing error, and angle measurement errors from chapter 4 and simulating them in chapter 5, this research collected information on how different errors affect orbit determination compared to the truth orbit. Unbiased satellite timing errors can be modeled with a zero-mean normal distribution, the standard deviation of which can be obtained from user manual equipment. Biased timing errors, such as shutter bias or calibration issues, can be modeled using a non-zero mean. These errors relate to any uncertainties associated with exact time of observation and result in object position uncertainty. Ground station timing error, or sidereal timing error, can be modeled in the same fashion using a normal distribution with zero-mean non-zero-mean for unbiased and biased cases respectively. This simulates any uncertainty associated with ground station location accuracy, which also results in object position accuracy. This can simulate uncertainties in GPS timing at the ground station or potentially poor calibration. Angle measurement errors can also be modeled as a random variable from a normal distribution. Angle errors may be a result of light refraction, lens distortion, or pixel position uncertainty.

In Geosynchronous Earth Orbits (GEO) or Highly Elliptical Orbits (HEO), satellite timing errors had a more apparent effect on position error than ground station timing error of the same degree. However, in Medium-Earth Orbits (MEO), ground station timing error had a larger effect. In the Low-Earth Orbit (LEO) cases, satellite timing had the largest effect and angle measurement followed closely in the same order of magnitude. For the unbiased cases at the (3σ) level of 0.001s for satellite timing error, GEO, HEO, MEO, and LEO have maximum orbit errors of 280.10 m, 89.82 m, 38.65 m, and 863.87 m, respectively. For the same unbiased cases for sidereal timing error at the (3σ) level of 0.001s, GEO, HEO, MEO, and LEO have maximum orbit errors of 108.17 m, 48.02 m, 191.06 m, and 24.30 m, respectively. Typically, angle measurement errors result in the higher levels of orbit error from truth. With a (3σ) level of just 0.1 arcsec, GEO, HEO, MEO, and LEO have maximum errors of 17.03 km, 3.99 km, 14.03 km, and 668.78 m respectively. It is most important for all sensor operators to minimize angle measurement error uncertainties or relay this

uncertainty when sharing data. Satellite timing then take priority in GEO, HEO, and LEO, and ground station timing takes priority in MEO.

The second research goal is achieved through use of the Shapiro-Wilk test, which was used to detect the errors modeled from the first objective. Since standard filtering methods such as the least squares method and Kalman filtering have decreased performance when using noisy data with unknown or highly varying noise levels, the distribution testing can be helpful in first determining whether or not a dataset is usable or can aid in the exlusion of singla data points. The distribution testing was able to detect 24 out of 32 satellite timing error scenarios and 26 out of 32 satellite ground station timing error scenarios. However, only 10 out of 32 angle measurement error scenarios were detected to have errors. Since the linear addition of the angle measurement error causes little change to the shape of the angle error distribution, the Shapiro-Wilk test results are inconclusive. For the cases of timing error and ground station timing error, the Shapiro-Wilk distribution testing at least provides users and operators with additional information extracted from just the dataset. Most importantly, no outside information is necessary to perform the distribution testing. In the context of data sharing, these results suggest that distribution tests be considered as a tool to determine the validity and usability of an incoming data set. It is not recommended that distribution testing be used to detect angle measurement errors.

6.2 Recommendations

The error modeling and application of distribution testing provide useful tools for orbit analysts and operators to improve their understanding of the uncertainty associated an object's position. Error modeling with random variables allows users to compute their own observation and measurement uncertainties, which they can relay to other sites when sharing data. The distribution testing produced consistent results for the timing and sidereal timing errors. It is recommended that this distribution testing be used to assess any suspicions of timing error or sidereal timing in shared

observation data sets for GEO, HEO, MEO, or LEO. It is not recommended however that the distribution testing be used to assess angle measurement errors in any of the orbital regions. Since there are limitations to statistical methods, machine learning is an appropriate next step for further investigation of how to detect errors in a data set.

REFERENCES

REFERENCES

[1] O. Montenbruck and E. Gill, *Satellite Orbits: Models, Methods, and Applications*. Berlin, Germany: Springer-Verlag, 2000.

[2] A. C. Snow, *Multi-Objective CubeSat Constellation Optimization for Space Situational Awareness*. Atlanta, Georgia: Georgia Institute of Technology, 2015.

[3] N. L. Johnson, E. Stansbery, J.-C. Liou, M. Horstman, C. Stokely, and D. Whitlock, *The characteristics and consequences of the break-up of the Fengyun-1C spacecraft*. Houston, Texas: Acta Astronautica 63, 2008.

[4] T. S. Kelso, *Analysis of the Iridium-33 and Cosmos-2251 Collision*. Center for Space Standards and Innovation, 2009.

[5] D. Mehrolz and L. Leushacke, *Detecting, Tracking and Imaging Space Debris*. Wachtberg, Germany: ESA, 2002.

[6] A. Butkus, K. Roe, B. Mitchell, and T. Payne, *Space Surveillance Network and Analysis Model Performance Improvements*. Defense Technical Information Center, 2007.

[7] P. W. Schumacher and F. R. Hoots, *Evolution of the NAVSPACECOM Catalog Processing System Using Special Perturbations*. Corpus Christi, Texas: Texas AM University, 2000.

[8] Y.-R. Kim, E. Park, D. Kucharski, H.-C. Lim, and B. Kim, *The challenge of precise orbit determination for STSAT-2C using extremely sparse SLR data*. Advances in Space Research, 2016.

[9] D. Vallado and V. Agopov, *Orbit Determination Results from Optical Measurements*. Center for Space Standards and Innovation, 2010.

[10] Analytical-Graphics-Incorporated, *https://www.agi.com*, Exton, Pennsylvania, 2020.

[11] E. Stevenson, S. Lemmens, and J. Siminski, *Deriving a Unified Space Object Catalogue for the Purpose of Space Debris Monitoring and Modelling*. Darmstadt, Germany: ESA, 2019.

[12] M. Undseth, C. Jolly, and M. Olivari, *Space Sustainability: The Economics of Space Debris in Perspective*. Paris, France: OECD Science, Technology, and Industry Policy Papers, No. 87, 2020.

[13] O. Montenbruck and T. Pfleger, *Astronomy on the Personal Computer*. Heidelberg, Germany: Springer, 2000.

[14] P. Kelly, *Optical Astrometry and Orbit Determination.* West Lafayette, Indiana: Purdue University, 2020.

[15] D. Lubey, H. Ko, and D. Scheeres, *Orbit Determination and Maneuver Detection Using Event Representation with Thrust-Fourier-Coefficients.* Maui, Hawaii: Advanced Maui Optical and Space Surveillance Technologies Conference, 2015.

[16] E. Delande, C. Frueh, J. Franco, J. Houssineau, and D. Clark, *Novel Multi-Object Filtering Appriach for Space Situational Awareness.* Edinburgh, Scotland: Journal of Guidance, Control, and Dynamics, 2018.

[17] D. Vallado, *Fundamentals of Astrodynamics and Applications.* El Segundo, California: Springer, 2001.

[18] C. Frueh, *Space Traffic Management.* West Lafayette, Indiana: Purdue University, 2019.

[19] V. J. Hodge and J. Austin, *A Survey of Outlier Detection Methodologies.* Artificial Intelligence Review, 2004.

[20] H. Iyer, C.-M. J. Wang, and D. F. Vecchie, *Consistency Tests for Key Comparison Data.* Metrologia, 2004.

[21] S. S. Shapiro and M. B. Wilk, *An Analysis of Variance Test for Normality.* Oxford, England: University of Oxford Press, 1965.

[22] B. Illowsky and S. Dean, *Introductory Statistics.* Houston, Texas: Rice University, 2013.

[23] T. W. Anderson and D. A. Darling, *A Test of Goodness of Fit.* Alexandria, Virginia: Journal of American Statistical Association, 1954.

[24] F. Sanson and C. Frueh, *Noise quantification in optical observations of resident space objects for probability of detection and likelihood.* AIAA/AAS Astrodynamics Specialist Conference: AIAA Press, 2016.

[25] ——, *Noise estimation and probability of detection in non-resolved images: Application to space object observation.* Advances in Space Research 64, 2019.

[26] J. Kovalevsky and P. K. Seidelmann, *Fundmentals of Astrometry.* Cambridge, United Kingdom: Cambridge University Press, 2004.

[27] T. Machines, *TM2000A Installation and Operation Manual.* Time Machines Corp.: Cambridge University Press, 2016.

[28] R. C. Stone, *An Accurate Method for Computing Atmospheric Refraction.* Flagstaff, Arizona: Astronomical Society of the Pacific, 1996.